

Thermal and Mechanical Development of Extremely High Heat Flux Cooling Modules Based on Jet Array Technology

by

Rudy S. Dahbura

B.S. in Mechanical Engineering,
University of California, Los Angeles, June 1995

and

Hesham F. Younis

B.S. in Mechanical Engineering
American University in Cairo, June 1994

Submitted to the Department of Mechanical Engineering in Partial Fulfillment of the
Requirements for the Degree of

Master of Science in Mechanical Engineering

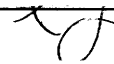
at the

MASSACHUSETTS INSTITUTE OF TECHNOLOGY

June, 1997

©Massachusetts Institute of Technology 1997. All rights reserved.

Signature of Authors



Department of Mechanical Engineering
May 9, 1997

Certified by



Associate Professor John H. Lienhard V
Thesis Supervisor

Accepted by

Professor Ain A. Sonin

Chairman, Department Committee on Graduate Studies

MASSACHUSETTS INSTITUTE
OF TECHNOLOGY

JUL 21 1997



Thermal and Mechanical Development of Extremely High Heat Flux Cooling Modules Based on Jet Array Technology

by

Rudy S. Dahbura and Hesham F. Younis

Submitted to the Department of Mechanical Engineering
on May 9, 1997 in Partial Fulfillment of the
Requirements for the Degree of Master of Science in
Mechanical Engineering

Abstract

Research describing a jet-array cooling module that supports high heat fluxes in steady state over relatively large areas is described. Heat fluxes of up to 7.2 MW/m^2 spanning an area of 10 cm^2 have been successfully dissipated. Convective cooling is provided by an array of 14 small diameter water jets operating at speeds of 40 to 50 m/s and arranged in a hexagonal planform. These jets impinge on the rear surface of an electrically heated metallic faceplate 2 to 4 mm thick. Dispersion strengthened copper (alloy C15715) and molybdenum (TZM) faceplates have been used in the module development and testing. The heat is generated through the use of a thin-film metallic resistance heater of a relatively new design. The heater is deposited directly onto an electrically insulating thin-film ceramic coating on the faceplate using plasma spray technology. The heaters are described in detail, analytically and experimentally.

High velocity liquid jets operating at 50 m/s produce especially thin boundary layers on the impinging surface. They can easily produce heat transfer coefficients of $200,000 \text{ W/m}^2\cdot\text{K}$ or so over a circle having a diameter of roughly 1.5 times the jet diameter. Single jet and jet array configuration behavior is summarized.

Design and performance estimates are described for the cooling modules. Utilizing finite element analysis, the steps required to minimize the thickness of an isothermal faceplate subject to the impinging jet pressure loads are described. The module faceplates have been designed to resist mechanical failure resulting from large temperature gradients, loads owed to the impinging liquid jets, and additional stresses related to the mechanical boundary conditions. Further numerical simulations for our specific case are used to determine module failure at high fluxes owing to stress levels that may exceed yield strength and to conduct studies of the effects of varying faceplate material and thickness. Failure was determined to occur at either the geometrical center of the faceplate or near the corner of the heater, depending on the faceplate material. Numerical results show molybdenum TZM to exhibit the greatest sustainable heat flux prior to failure.

Transient and steady state thermal models are described in detail. Transient faceplate temperature distributions are described. The theoretical development of a thin film heater is described taking into account the effects of temperatures in the faceplate, ceramic insulator and the configuration of the available power supply.

The evolution of the thin-film heaters is described, including steps taken to optimize their performance subject to the available power supply and plasma spray technology. The effects of the film thickness and material for the heater and ceramic insulator are discussed. Thin-film molybdenum heaters, coupled with aluminum oxide electrical insulators were found to be the most effective. Heat flux limitations were due to heater failure at temperatures on the order of 600 °C.

The effects of the heater surface temperature scatter and electrical resistance are discussed. The thermal resistance in the system is quantified, and factors that limit heat flux in the present experiments are described. Heating data results are presented in order to provide estimates detailing the fraction of heat absorbed by the cooling water and the fraction of heat lost due to conduction and radiation to the environment. These losses were determined to be approximately 3 % of the total power generated. The performance results of the cooling module are presented. The temperature difference between the bulk liquid and the heater surface has been shown as a function of the heat flux. The thermal resistance of the faceplate assembly, including the boundary layer, faceplate, and ceramic film, depends strongly upon the faceplate material, the ceramic material and thickness, as well as the quality of the films produced by various plasma spray vendors. It was determined that the heater's thermal resistance is negligible. The temperature distribution across the thin-films, faceplate and the cooling water are quantified.

Thesis Supervisor: John H. Lienhard V

Title: Associate Professor of Mechanical Engineering

Acknowledgments

The authors wish to thank Professor John H. Lienhard V for his guidance and insight which strongly contributed to the completion of this work. We are indebted to his contributions which shaped our graduate education and greatly appreciate the opportunity he has given us.

This project has been funded by the INEL University Research Consortium. The INEL is managed by Lockheed Martin Idaho Technologies Company for the U.S. Department of Energy, Idaho Operations Office, under Contract No. DE-AC07-94ID13223.

Table of Contents

Abstract	2
Acknowledgments	4
Table of Contents	5
List of Tables	7
List of Figures	8
Nomenclature	10
1. Introduction	13
2. Experimental Apparatus	15
2.1 Flow Loop Components	15
2.2 Pump Performance	17
2.3 Cooling Module	18
2.3.1 Lower Manifold	21
2.3.2 Nozzle Plate and Nozzles	21
2.3.3 Low Pressure Manifold and Faceplate	23
2.3.4 Clamp	25
2.3.5 Temperature Measurements	26
2.4 Flow Loop Theoretical Calculations	27
2.4.1 Temperature Rise In The Flow Loop	27
2.4.2 Pressure Drop Calculations	28
2.4.3 Calculation Of The Manifold's Contour	29
2.4.4 Stresses In The Nozzle Plate	30
2.5 Cooling Module Experimental Performance	30
3. Cooling by Impinging Jets	32
3.1 Introduction	32
3.2 Free Surface Jets	32
3.3 Submerged Jets	34
3.4 Jet Arrays	36
3.5 Flow and Temperature Simulations	37
4. Thermal and Mechanical Faceplate Stresses	44
4.1 2D Stress Analysis	48
4.2 3D Thermal and Stress Analysis	51
4.2.1 Summary of Finite Element Simulations	59
5. Transient and Steady State Thermal Models	62
5.1 Faceplate Transient Thermal Analysis	62
5.2 Analytical Heater Design	62
5.2.1 Pyrolytic Graphite Heaters	62
5.2.2 Thin Metal Film Heaters	63
6. Experimental Development of Thin Film Heaters	70
6.1 Heater Development	70
6.2 Surface Temperature Scatter	73
6.3 Electrical Resistance	75
6.4 Thermal Resistance	76

6.5 Heater Failure	78
6.6 Future Recommendations	80
7. Heating Data	83
7.1 Power Generation and Absorption	83
7.2 Module Cooling Performance	84
7.3 Discussion	92
Appendix A – Flow Loop Components	94
Appendix B – Pressure Drop Calculation Across the Nozzles	96
Appendix C – Temperature Dependent Material Properties	97
Appendix D – COSMOS/M Finite Element Algorithm	98
Appendix E – Temperature Data	103

List of Tables

Table 1 Locations for thermocouples 1 - 7 when (x,y) is measured from the lower left corner of the heater.	27
Table 2 Minor pressure losses at 70 gpm.	28
Table 3 Thermal and elastic properties of various materials.	45
Table 4 Temperature and heat flux at which a simply supported circular plate reaches yield stress during localized heating. T_{max} in K and $q \cdot H$ in MW·mm/m ² .	47
Table 5 Temperature and heat flux at which a fixed-edge circular plate reaches yield stress during localized heating. T_{max} in K and $q \cdot H$ in MW·mm/m ² .	47
Table 6 Stresses and temperatures as a function of heat flux. DS Copper (C15715), 2.5 mm thick faceplate FEM results. Italicized stresses exceed the local yield stress.	60
Table 7 Stresses and temperatures as a function of heat flux. DS Copper (C15715), 3.0 mm thick faceplate FEM results. Italicized stresses exceed the local yield stress.	60
Table 8 Stresses and temperatures as a function of heat flux. DS Copper (C15715), 4.0 mm thick faceplate FEM results. Italicized stresses exceed the local yield stress.	60
Table 9 Stresses and temperatures as a function of heat flux. TZM, 2.5 mm thick faceplate FEM results. Italicized stresses exceed the local yield stress.	61
Table 10 Stresses and temperatures as a function of heat flux. TZM, 3.0 mm thick faceplate FEM results. Italicized stresses exceed the local yield stress.	61
Table 11 Stresses and temperatures as a function of heat flux. TZM, 4.0 mm thick faceplate FEM results. Italicized stresses exceed the local yield stress.	61
Table 12 Early problems encountered with thin film heaters.	72
Table 13 Surface temperature scatter (evaluated at $q \approx 3 \text{ MW/m}^2$) and electrical resistance data for various heater configurations.	75
Table 14 Thermal resistance values for various heater/plate configurations.	77
Table 15 Heat flux and peak surface temperature at failure for various heater/faceplate configurations.	79
Table 16 Parts listing.	94
Table 17 Temperature dependent material properties for dispersion strengthened copper (C15715).	97
Table 18 Temperature dependent material properties for molybdenum (TZM).	97

List of Figures

Figure 1 Flow loop schematic diagram.	15
Figure 2 Pump performance curves.	18
Figure 3 Cooling module configuration showing manifolds, jet array and faceplate.	19
Figure 4 Cooling module cross-section illustrating the flow path.	20
Figure 5 High pressure lower manifold.	20
Figure 6 Top view of the nozzle plate.	22
Figure 7 Low pressure upper manifold.	23
Figure 8 Faceplate clamping configuration.	26
Figure 9 Area normal to the liquid flow in the high pressure manifold.	29
Figure 10 The cooling module pressure drop, ΔP , as a function of the system flow rate, \dot{Q} .	31
Figure 11 Axisymmetric simulation configuration and numerical grid.	38
Figure 12 Calculated variation of pressure as a function of radial distance from stagnation point for $u_j = 20, 30, \text{ and } 40 \text{ m/s}$ at 20 MW/m^2 .	38
Figure 13 Radial liquid velocity just outside the boundary layer as a function of the radial distance from the stagnation point for $u_j = 20, 30, \text{ and } 40 \text{ m/s}$ at 20 MW/m^2 .	39
Figure 14 Liquid-side temperature of copper as a function of radial distance from the stagnation point for $u_j = 40 \text{ m/s}$ at 20 MW/m^2 .	41
Figure 15 Hot side temperature of copper as a function of the radial distance from the stagnation point for $u_j = 40 \text{ m/s}$ at 20 MW/m^2 .	41
Figure 16 Calculated variation of h as a function of the radial distance from the stagnation point for $u_j = 20, 30, \text{ and } 40 \text{ m/s}$ at 20 MW/m^2 .	42
Figure 17 Faceplate configuration. Shaded area is heated.	48
Figure 18 Uniform pressure required to yield an isothermal faceplate.	49
Figure 19 Uniform pressure required to yield an isothermal faceplate.	50
Figure 20 Finite element thermal analysis results for a one quarter, 3 mm TZM faceplate model with a heat flux of 10 MW/m^2 .	52
Figure 21 Finite element stress analysis results for a one quarter, 3 mm TZM faceplate model with a heat flux of 10 MW/m^2 .	53
Figure 22 TZM faceplate top surface temperature variation across the heater width.	55
Figure 23 TZM faceplate bottom surface heat flux variation across the heater width.	55
Figure 24 Maximum faceplate temperature as a function of the heat flux.	56
Figure 25 Stress vs. heat flux for a 2.5 mm C15715 faceplate.	56
Figure 26 Stress vs. heat flux for a 3.0 mm C15715 faceplate.	57
Figure 27 Stress vs. heat flux for a 4.0 mm C15715 faceplate.	57
Figure 28 Stress vs. heat flux for a 2.5 mm TZM faceplate.	58
Figure 29 Stress vs. heat flux for a 3.0 mm TZM faceplate.	58
Figure 30 Stress vs. heat flux for a 4.0 mm TZM faceplate.	59
Figure 31 Composite series wall.	64
Figure 32 Temperature distribution throughout the faceplate assembly for a 3 mm C15715 faceplate, an 8 mil Al_2O_3 insulator, and a 1.2 mil molybdenum heater.	69

Figure 33	The required heater voltage as a function of the desired heat flux for a 3 mm C15715 faceplate, an 8 mil Al ₂ O ₃ insulator, and a 1.2 mil molybdenum heater.	69
Figure 34	Heater top surface temperatures for various thermocouples as a function of the heat flux for Data Set D.	74
Figure 35	Experimental and theoretical heater film resistance as a function of the surface average film temperature for Data Set D.	76
Figure 36	Electrical power dissipated and heat absorbed as a function of the electric current for Data Set D (see Table 14).	84
Figure 37	Average temperature difference between the bulk liquid and the heater film's upper surface for Data Set A (see Table 14).	85
Figure 38	Average temperature difference between the bulk liquid and the heater film's upper surface for Data Set B (see Table 14).	86
Figure 39	Average temperature difference between the bulk liquid and the heater film's upper surface for Data Set C (see Table 14).	86
Figure 40	Average temperature difference between the bulk liquid and the heater film's upper surface for Data Set D (see Table 14).	87
Figure 41	Average temperature difference between the bulk liquid and the heater film's upper surface for Data Set E (see Table 14).	87
Figure 42	Average temperature difference between the bulk liquid and the heater film's upper surface for Data Set F (see Table 14).	88
Figure 43	Average temperature difference between the bulk liquid and the heater film's upper surface for Data Set G (see Table 14).	88
Figure 44	Average temperature difference between the bulk liquid and the heater film's upper surface for Data Sets A-G (see Table 14).	89
Figure 45	Temperature distribution throughout the faceplate assembly and the bulk liquid for Data Set D.	90
Figure 46	Temperature distribution throughout the faceplate assembly and the bulk liquid for Data Set E.	90
Figure 47	Temperature distribution throughout the faceplate assembly and the bulk liquid for Data Set F.	91
Figure 48	Temperature distribution throughout the faceplate assembly and the bulk liquid for Data Set G.	91

Nomenclature

- a = faceplate width (m)
 A = lower manifold cross-sectional area normal to the water flow (m^2)
 A_h = heater area (m^2)
 b = faceplate length (m)
 c_p = specific heat of water (J/kg·K)
 d = jet diameter (m)
 D_L = lower manifold hydraulic diameter (m)
 E = Young's Modulus (Pa)
 E_{max} = dielectric strength (V/m)
 f = friction factor
 h = heat transfer coefficient ($W/m^2 \cdot K$)
 H = circular disc thickness (mm)
 h_{avg} = average heat transfer coefficient ($W/m^2 \cdot K$)
 h_{loss} = minor head loss (m)
 i = electric current (amps)
 k = thermal conductivity ($W/m \cdot K$)
 k_f = thermal conductivity of the faceplate ($W/m \cdot K$)
 k_h = thermal conductivity of the heater ($W/m \cdot K$)
 k_i = thermal conductivity of the ceramic insulator ($W/m \cdot K$)
 l = heater length (m)
 L = manifold length (m)
 \dot{m} = water mass flow rate (kg/s)
 P = water pressure (Pa)
 $P_{ambient}$ = ambient pressure (Pa)
 P_{stag} = jet stagnation pressure (Pa)
 q = heat flux (W/m^2)
 \dot{q} = internal heat generation (W/m^3)
 \dot{Q} = water volume flow rate (m^3/s)
 $Q_{absorbed}$ = power absorbed by water flow (W)
 Q_{efm} = figure of merit for elastic performance ($MW \cdot mm/m^2$)
 q_1 = distributed pressure load on the faceplate (Pa)
 q_{TZM} = TZM faceplate bottom surface heat flux (W/m^2)
 r = radial distance from the jet stagnation point (m)
 R = electrical resistance of heater (Ω)
 $R_{th,bl}$ = thermal resistance of the boundary layer ($m^2 \cdot K/MW$)
 $R_{th,films}$ = thermal resistance of the heater and ceramic insulating films ($m^2 \cdot K/MW$)

$R_{th,plate}$ = thermal resistance of the faceplate ($m^2 \cdot K/MW$)
 $R_{th,total}$ = total thermal resistance between the heater and the water boundary layer ($m^2 \cdot K/MW$)
 s = nozzle to nozzle spacing (m)
 t_f = thickness of the faceplate (m)
 t_h = thickness of the heater (m)
 t_i = thickness of the ceramic insulator (m)
 T_0 = temperature at the heater surface (K)
 T_1 = temperature at the heater/ceramic insulator surface (K)
 T_2 = temperature at the ceramic/faceplate surface (K)
 T_3 = temperature at the faceplate/water surface (K)
 T_c = circular disc cold temperature (K)
 T_f = film temperature (K)
 T_h = circular disc hot temperature (K)
 T_∞ = free stream water temperature (K)
 T_{jet} = water jet temperature (K)
 T_m = material melting temperature (K)
 T_{max} = circular disk maximum temperature (K)
 T_{melt} = solidus temperature for metallic alloys (K)
 T_{TZM} = TZM faceplate top surface temperature ($^{\circ}C$)
 T_{wall} = heated surface wall temperature (K)
 u_j = jet water velocity (m/s)
 V = voltage across the heater (V)
 V_{max} = maximum voltage before dielectric breakdown (V)
 w = heater width (m)
 X_i = jet center coordinate (m)
 Y_i = jet center coordinate (m)
 z = nozzle to target separation (m)

Greek Letters

ΔP = pressure difference (Pa)
 $\Delta P_{nozzles}$ = pressure difference across a nozzle (Pa)
 ΔT = temperature difference (K)
 ΔT_{bulk} = bulk temperature increase of water through the cooling module (K)
 α = thermal diffusivity (m^2/s)
 α_n = eigenvalue to series solution
 ν = kinematic viscosity (m^2/s)
 ρ = mass density (kg/m^3)

ρ_e = electrical resistivity ($\Omega \cdot m$)

σ_y = yield strength (Pa)

1. Introduction

High heat flux systems may generally be separated into one of two categories: those requiring a moderately high heat flux over a large area and those involving a hot-spot with extremely large flux over a small area. Few designs are capable of removing an extremely large flux over a large area. Quantitatively, small areas may be regarded as those of a few square millimeters and moderately high fluxes may be regarded as those of up to 10 MW/m^2 . While the precise demarcations are debatable, there is clearly a need for systems that support fluxes in excess of 10 MW/m^2 over areas of several square centimeters or more.

Here, we report on the development of a cooling module design intended to remove heat fluxes of 20 MW/m^2 or more over areas of 10 cm^2 or more. The module uses an array of high speed impinging liquid jets to convectively cool the rear of a heated faceplate. The forward surface is heated by a thin-film resistance heater applied using plasma spray technology.

Impinging liquid jets are of value in this application for both their high heat transfer coefficients and their ability to carry high heat fluxes. Extrapolation of existing correlations¹ into our range of Reynolds number (up to 200,000) predicts heat transfer coefficients on the order of $200,000 \text{ W/m}^2 \cdot \text{K}$.

Although the stagnation pressure of a high speed liquid jet significantly raises the stagnation temperature and can enable high wall temperatures and extremely high heat fluxes to exist in the stagnation zone,² both the pressure and the heat transfer coefficient drop rapidly as the distance from the stagnation point increases. Consequently individual jets are unsuitable for high-flux cooling of areas significantly larger than the cross-sectional area of the jet. Our approach is to place an array of jets (3 to 4 jet diameters center-to-center) on a tightly spaced hexagonal planform, so as to limit the area cooled by each jet to diameters of only 3 to 4 times the jet diameter. Such arrays can largely compensate for the radial decrease in the heat transfer

¹ J.H. Lienhard V, "Liquid Jet Impingement," *Annual Review of Heat Transfer*, (C.L. Tien, ed.), Vol. 6, Ch. 4. New York: Begell House, 1995, pp. 199-270.

² X. Liu and J.H. Lienhard V, "Extremely High Heat Fluxes Beneath Impinging Liquid Jets," *J. Heat Transfer*, Vol. 115, pp. 472-476, 1993.

coefficient,³ and can slightly compensate for the declining pressure. This arrangement will not sustain fluxes as high as may be reached within the stagnation zone of a single jet, but should support fluxes within our range of interest. Detailed design estimates⁴ suggest that an array of water jets having our geometry and velocity should support heat fluxes above 20 MW/m² over areas of many square centimeters without boiling.

Test heating is accomplished using a resistance heater driven by a high current and low voltage DC power supply. Often, when high heat flux resistance heating is needed, graphite heating elements are mechanically mounted to the surface. Unfortunately, thermal contact resistance between surfaces, rapid graphite oxidation at high temperatures, and geometrical constraints limit the utility of graphite for our purpose. Consequently, we have developed thin-film metal resistance heaters. A ceramic insulator film is located between the faceplate and the metallic heater film.

The other significant barrier to high heat flux cooling is the mechanical failure of the heated surface, which in the present case is the module's faceplate. High heat flux surfaces must be only a few millimeters thick in order to limit heat conduction resistance and its associated temperature rise. Thermal stresses owed to nonlinear temperature gradients, heater geometry, and the faceplate's mechanical boundary conditions can cause yielding and mechanical failure as the heated material softens. In addition, the faceplate must withstand the pressure loads from the impinging liquid jets. Detailed stress analyses have been reported previously,^{4,5} and appropriate materials have been identified for these conditions, including a dispersion strengthened copper (alloy C15715)⁶ and a molybdenum alloy (TZM).

³ Y. Pan and B.W. Webb, "Heat Transfer Characteristics of Arrays of Free-Surface Liquid Jets," *J. Heat Transfer*, Vol. 117, No. 4, pp. 878-883, 1995.

⁴ J.H. Lienhard V, R.S. Dahbura, H.F. Younis, and C.H. Oh, 1996, "Large Area Jet-Array Cooling Modules for High Heat Fluxes," *High Heat Flux Engineering III*. SPIE Vol. 2855, pp. 66-81, 1996.

⁵ J.H. Lienhard V and D.S. Napolitano, "Thermal Stress Limits of Plates Subjected to Extremely High Heat Fluxes," *ASME Intl. Mech. Engr. Congress and Exhibition*, Atlanta, November 1996.

⁶ SCM Metal Products, "GLIDCOP: Copper Dispersion Strengthened with Aluminum Oxide," Research Triangle Park, NC, 1994.

2. Experimental Apparatus

2.1 Flow Loop Components

A schematic diagram of the flow loop is shown in Figure 1. The flow loop can be divided into two main sections: a low and a high pressure section. Water flows from a 1892 L (500 gallon) capacity reservoir at low pressure through 2 in. PVC piping where the flow rate is recorded by a turbine flowmeter. The pipe diameter is then stepped up to 2½ in. in order to match the pump entrance. After experiencing a pressure rise, the flow passes through 2½ in. schedule 40, 304 stainless steel piping and is gradually reduced back to 2 in. The 2 in. schedule 40 stainless piping is rated to a theoretical bursting pressure of 67.06 MPa (9,726 psi) and is all welded according to Mil Standard 8611.

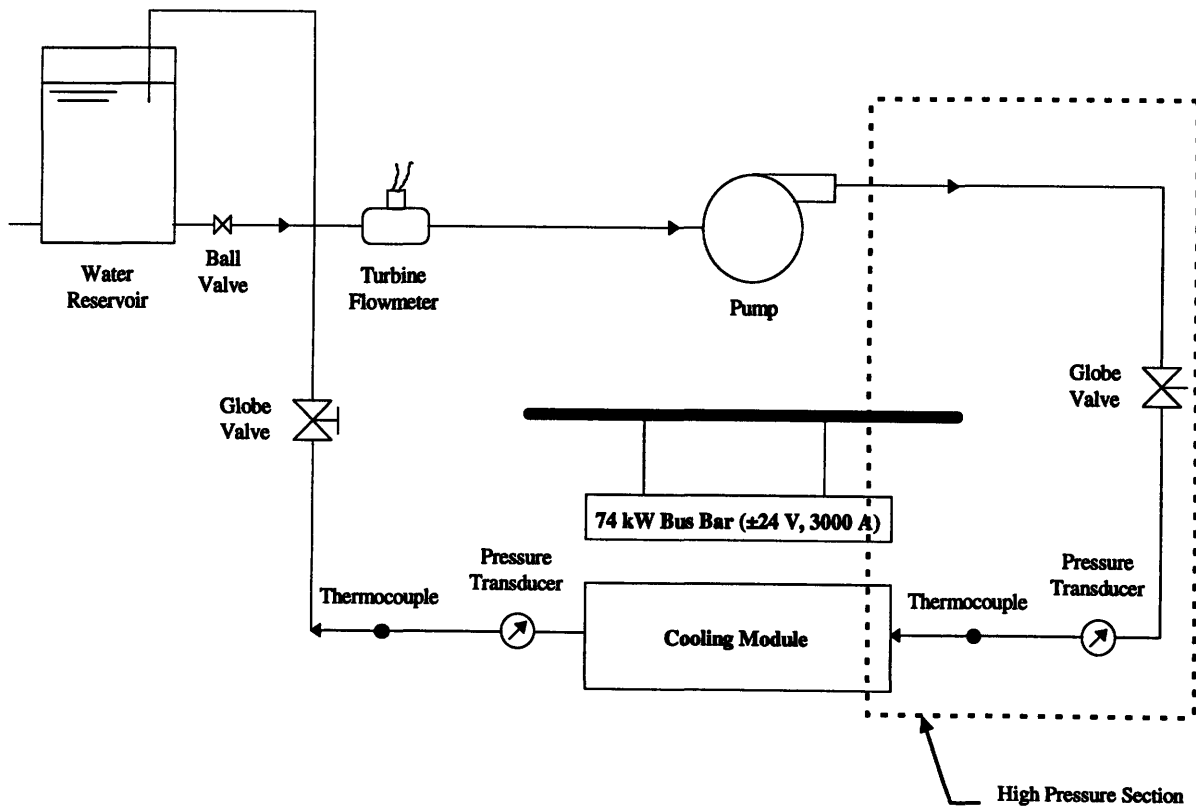


Figure 1 Flow loop schematic diagram.

The flow is throttled through a 2 in. globe valve for flow regulation and the pipe is then raised a vertical distance of 3 ft. above the floor to position the test section at a comfortable working height. After the pressure drop in the test section, the flow returns to a low pressure state and is guided back to the top of the reservoir through PVC piping.

Since flow passing through the flowmeter must be free of secondary flows, a minimum straight pipe run of at least 10 pipe diameters is recommended at the meter's entrance and 5 pipe diameters at its exit.⁷ This evaluates to a minimum straight pipe run at the entrance of 10 x 2 in. = 20 in. (actual value is 54 in.) and 5 x 2 in. = 10 in. (actual value is 22 in.) at the exit.

The end-to-end dimension of the loop is 139 in., measured from the exit of the reservoir to the outermost point on the loop. The low pressure (PVC pipe and flowmeter) section before the pump measures a total distance of 90.5 in. The pump is then followed by a straight stainless steel section of length 27.5 in. (which includes a concentric reducer) after which a 90° long radius bend leads another section of straight pipe horizontally into the valve and to yet one more 90° long radius elbow which directs the flow vertically upwards. The length of this horizontal section (from elbow to elbow) is 36 in.

After that, the pipe is raised to a height of 36 in. above floor level and another 90° long radius elbow is used to bring the flow back horizontally. The final portion of the high pressure stainless steel section is a straight pipe of length 59 in. that leads into the test section.

The flow loop instrumentation includes a turbine flowmeter (accurate to ± 1 %) with a digital rate meter and two diaphragm pressure transducers (accurate to ± 0.1 %) with digital process meters. Before operating the instrumentation, the rate and process meters were appropriately scaled and connected to the flow loop. The rate meter was scaled to read through a range of 0 - 17.35 L/s (0 - 275 gpm) and the process meters 0 - 3.45 MPa (0 - 500 psi). In order to test the pressure transducers, they were mounted on the inlet and outlet flanges of the pump and the valve was used to vary the flow rate. Data was taken several times to obtain a pump performance curve. The power delivered by the bus bars will be used to heat the face plate of our prototype cooling module.

⁷ Omega Technologies Company, "FTB-100 Series & FTB-200 Series Turbine Meters Operator's Manual," Omega Engineering, Inc., 1995.

A globe valve after the test section controls the back pressure. The pressure transducers are presently located before and after the test section in order to measure the actual pressure drop across our cooling module. Type K thermocouples (accurate to ± 0.05 °C) are fitted into positions farther downstream than the pressure transducers so as not to interfere with the pressure readings. These thermocouples measure the temperature rise of water through our test section. The high pressure section is all constructed of 304 stainless steel, except for the 316 stainless steel globe valves. Appendix A lists all the flow loop components.

Although most of our piping has been 2 in. nominal diameter, a pipe size of 1 in. was chosen at the exit of the cooling module. This was necessary to assure that flow exiting the upper manifold would not interfere with the flow leaving the nozzles, since the nozzles are only 2 in. long. To minimize pressure losses,⁸ however a 1½ in. globe valve has been chosen. Pressure drop calculations across a widely open globe valve revealed that a 1 in. valve causes a pressure drop of about 245 kPa (35.6 psi) for a flow rate of 4.416 L/s (70 gpm). This loss is dramatically reduced when using a 1½ in. globe valve, which causes a pressure drop of only 40.7 kPa (5.9 psi). Thus, a concentric expander has been added after the cooling module to expand from 1 in. to 1½ in. accommodating the valve and a further expansion from 1½ in. to 2 in. joined the manifold to the remainder of the flow loop.

2.2 Pump Performance

The pump is driven by a 30 hp motor and is rated at 2 MPa (300 psi) and 6.31 L/s (100 gpm). The discharge pressure was varied with the 2 in. globe valve. The pressure rise across the pump and the corresponding water flow rate were recorded in order to verify the manufacturer's pump curve. The results are shown in Figure 2 for convenience.

⁸ Crane Co., "Flow of Fluids Through Valves, Fittings, and Pipe," *Technical Paper No. 410M*, Crane Co., 1982.

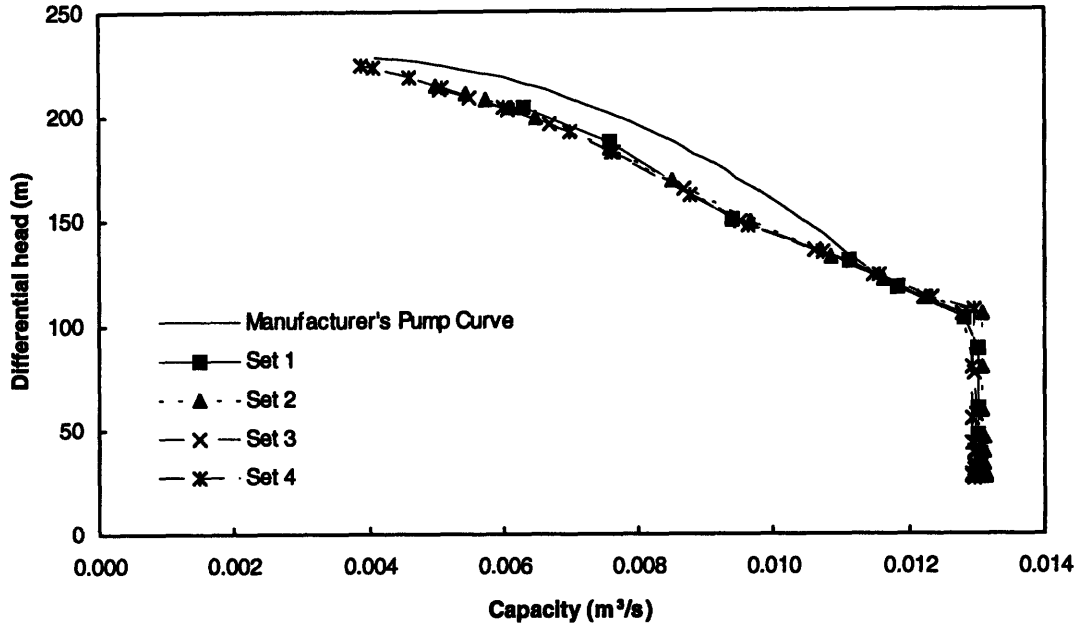


Figure 2 Pump performance curves.

2.3 Cooling Module

For heat fluxes of up to 40 MW/m^2 , we have decided to utilize a hexagonal array of 14 water jets operating at a velocity of 40 - 50 m/s to cool the face plate. Figure 3 shows an exploded view of the cooling module with the various components labeled.

The lower manifold is at a higher pressure than the upper manifold and is tapered to limit stream wise variations in dynamic pressure. The liquid is driven into the tube nozzles from the higher pressure manifold to the lower pressure, upper manifold. In doing this, it experiences a pressure drop across the nozzles and a rise in velocity, u_j , related by

$$\Delta P_{\text{nozzles}} \approx 1.8 \left(\frac{1}{2} \rho u_j^2 \right) \quad (2.1)$$

which is obtained from an analytical pressure drop calculation (see Appendix B). Thus, by controlling $\Delta P_{\text{nozzles}}$, the flow rate through the tube nozzles is varied. As illustrated in Figure 4, the fluid passes through the nozzles and impinges onto the faceplate, which is attached to the upper manifold with a carefully designed clamp that will help reduce thermal stresses.

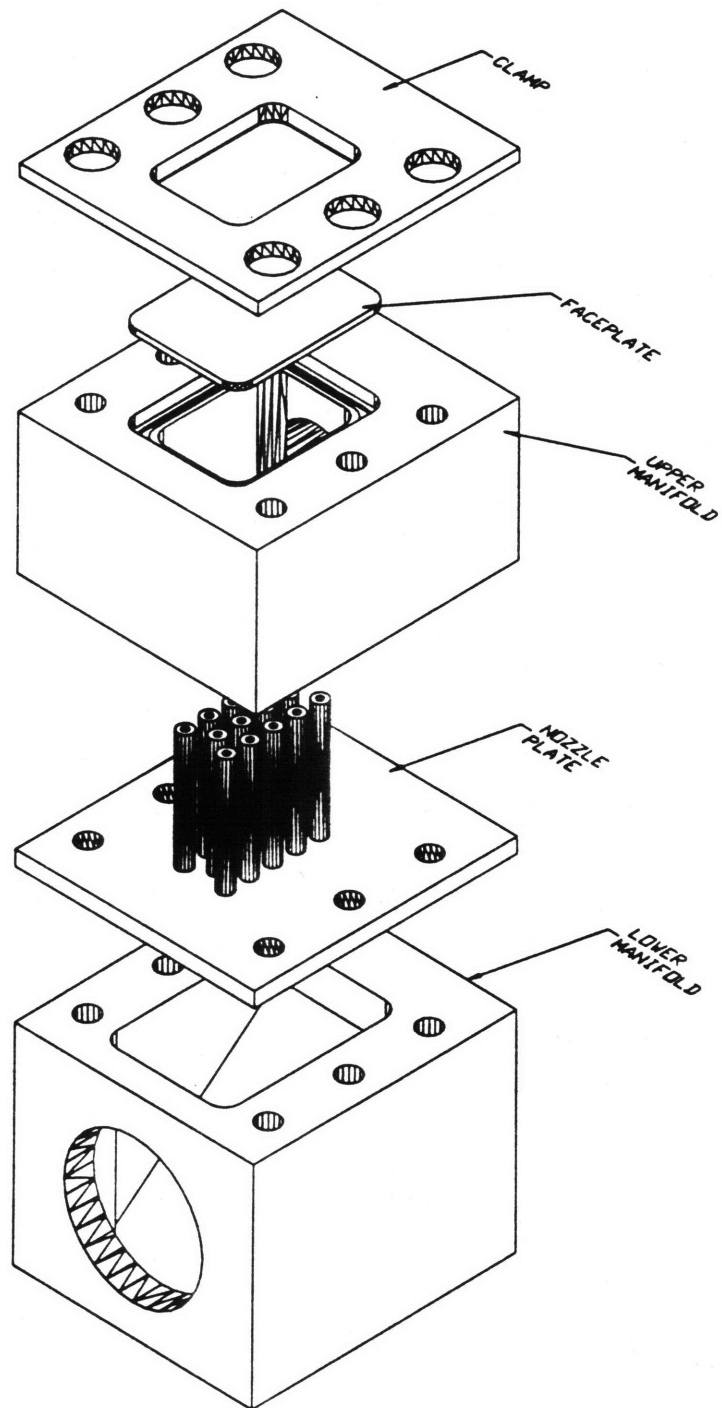


Figure 3 Cooling module configuration showing manifolds, jet array and faceplate.

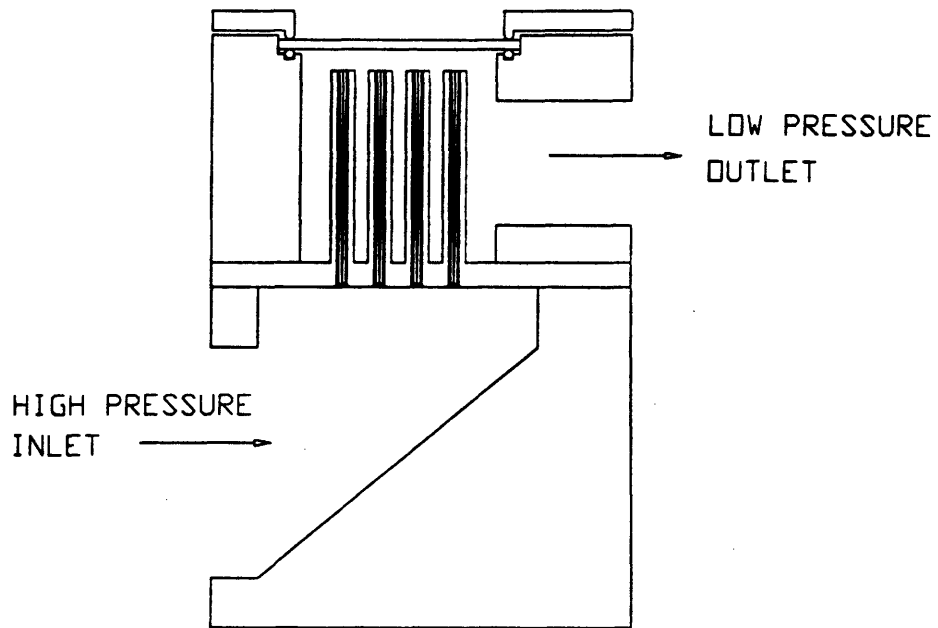


Figure 4 Cooling module cross-section illustrating the flow path.

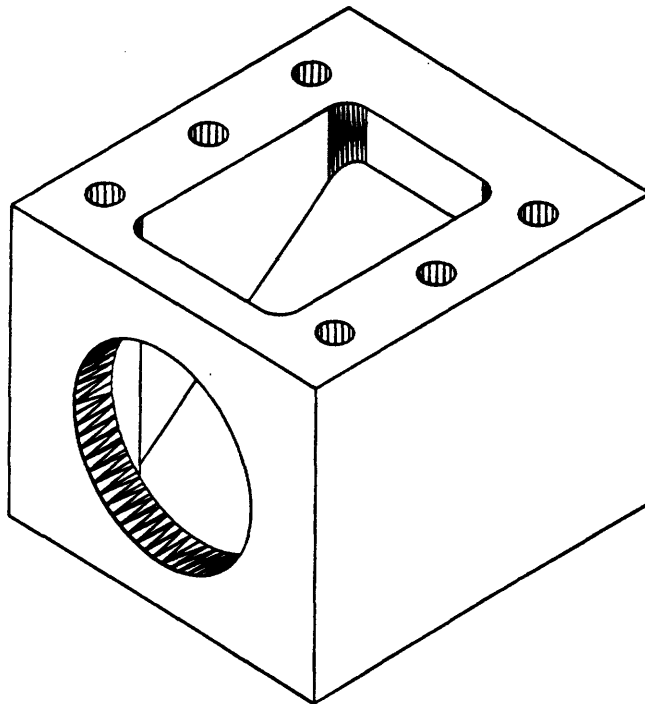


Figure 5 High pressure lower manifold.

2.3.1 Lower Manifold

The lower manifold is machined out of a block of 304 stainless steel and is of external dimensions 10.4 cm by 11.4 cm by 8.9 cm deep (4.1 in. by 4.5 in. by 3.5 in. deep). This manifold is tapered along its length, so as to minimize pressure variations through the manifold which might cause different jets to flow at different speeds. To incorporate the tapered feature, a solid triangular wedge was inserted and plug welded into the bottom of the manifold as shown in Figure 5. Water enters the manifold at 2 MPa (300 psi) through a 2 in. nominal diameter pipe welded into the front of the manifold.

Calculations used to determine the desired angle of taper within the supply manifold yielded an angle α of 45° measured from the horizontal. To avoid constricting the flow entering the last two nozzles, α was reduced to 38.4° . The full details of the calculation are outlined in Section 2.4.3. Since the manifold is short in length, friction losses along it are negligible.

2.3.2 Nozzle Plate and Nozzles

The nozzle plate in Figure 6 has been designed to a thickness of 0.953 cm (3/8 in.) and an area of 10.4 by 11.4 cm (4.1 by 4.5 in.) to fit on top of the lower portion of the manifold. The spacing between the nozzles has been chosen to be 1 cm (0.4 in.), rather than the initially proposed value of 1.6 cm (0.625 in.). Our initial design idea for the top manifold was to bore out annular passages (in a hexagonal array) for each jet into a high conductivity metallic block thus confining each jet to its own annular region. A higher nozzle to nozzle spacing, s , was needed for such a configuration in order to incorporate the annuli. This idea was aborted to make use of the enhanced cooling produced by the secondary stagnation zone resulting from the radial interaction of the jets (Section 3.4) and consequently, the nozzle to nozzle spacing could be reduced. In fact, previous work on jet arrays has shown the strongest secondary maxima in Nusselt numbers to be at an s/d value of 4, where d is the jet diameter. Our s/d value currently stands at 3.6.

The inner nozzle diameter was chosen to be 2.78 mm (7/64 in.). Smaller diameters lead to higher average heat transfer coefficients, h_{avg} , but jet diameters of less than 1 to 2 mm become

impractical owing to manufacturing considerations and the potential to clog nozzles. Increasing jet speed raises h_{avg} as well. However, whereas h_{avg} rises as $u_j^{0.6}$, the liquid flow rate rises as u_j , the supply pressure rises as u_j^2 and the pumping power rises as u_j^3 . The cost of pumps is more nearly proportional to the pumping power, so that a value of $u_j \approx 50$ m/s was the highest speed deemed cost effective for this project. Having set the speed, nozzles of 2 to 3 mm diameter and a spacing of about 10 mm provide the desired range of h_{avg} while posing no special fabrication problems.

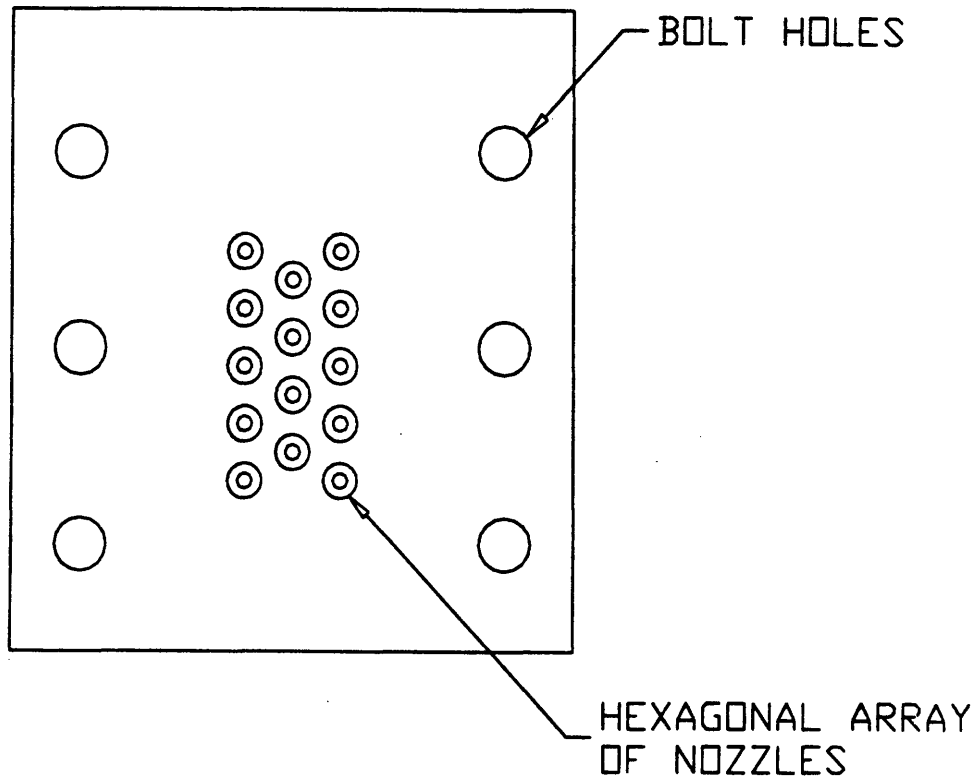


Figure 6 Top view of the nozzle plate.

The outer nozzle diameter was chosen to be 6.35 mm (1/4 in.). A thick wall was chosen in order to enable us to thread the nozzles. Threading also allows us to change nozzles as desired and thus vary nozzle length as well as providing a tight seal. A total of 14 holes have been drilled and tapped into the plate. The plate has been made 0.953 mm (3/8 in.) thick to accommodate the

nozzles. The nozzles are 5.72 cm (2¼ in.) and thread 0.64 cm (¼ in.) into the plate. The inlets to the nozzles has been filleted to reduce entrance pressure drops. The stresses in the nozzle plate subjected to a uniform pressure of 300 psi have been analyzed using finite element modeling⁹ (see Section 2.4.4). The results of the simulation found the maximum von Mises stress in the nozzle plate to be 26 MPa (3.76 ksi), in comparison to a yield stress of 227.5 MPa (33 ksi) for 304 stainless steel. The hoop stress in the nozzle walls due to 300 psi internal pressure was also calculated to be 2.63 MPa.

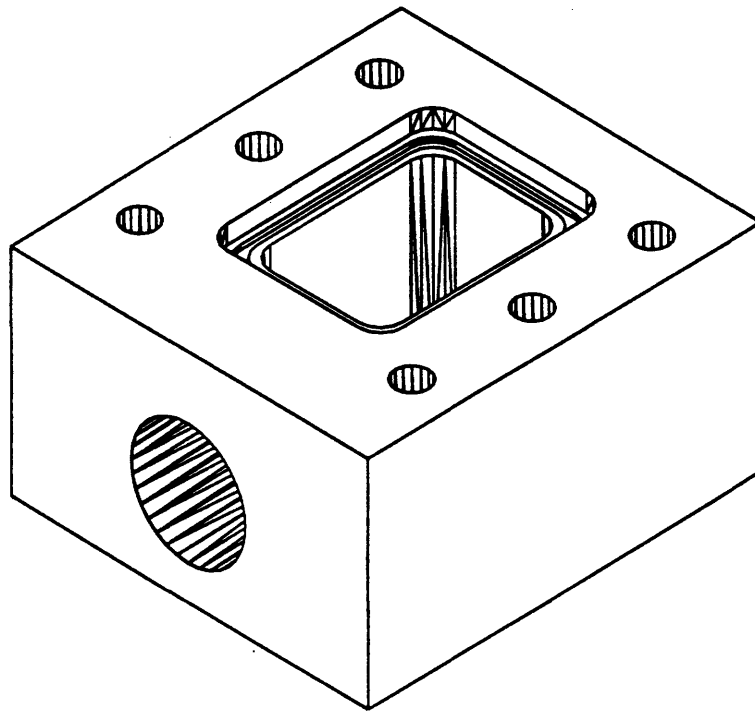


Figure 7 Low pressure upper manifold.

2.3.3 Low Pressure Manifold and Faceplate

The upper, low pressure manifold, shown in Figure 7, is of similar external dimensions to the lower manifold, but only 6.03 cm (2.375 in.) deep. After impinging on the faceplate, the low pressure water leaves this manifold through a 1 in. nominal diameter pipe. A groove is machined

⁹ COSMOS/M Version 1.75. Los Angeles, CA: Structural Research and Analysis Corp., 1995.

on the top of the upper manifold to accommodate a high temperature silicone O-ring on top of which the faceplate sits. The faceplate is of dimensions 5.08 cm by 6.60 cm (2 in. by 2.6 in.). This area was chosen since it is the smallest area that can accommodate the heater, clamp and the bus bars that supply the heater. In addition, the pressure stresses have been shown to be lower for this size plate in comparison to a larger one (see Section 4.1). The heated area is smaller and is of dimensions 5.08 cm by 2.80 cm (2 in. by 1.1 in.). The heater design is discussed in detail in Section 5.2.

The materials for the faceplate have been chosen to be C15715, a dispersion strengthened copper and molybdenum TZM alloy. Copper is a very desirable material to use for high heat flux applications because its high thermal conductivity limits thermal stresses. However, pure copper loses much of its strength at relatively low temperatures. After a one hour exposure to 300 °C, for example, the yield strength of pure oxygen free copper drops from 400 MPa to approximately 250 MPa, a 37.5 % reduction and if exposed to 400 °C, pure copper loses virtually all its strength.¹⁰ Such temperatures are easily exceeded in high heat flux systems.

This has led to the search for materials that have thermal conductivity similar to copper, but which retain higher strengths. Cold working can be used to increase the strength of copper, but its effects are lost once the recrystallization temperature is exceeded. For most pure metals, the recrystallization temperature is between one third to one half the absolute melting temperature T_m . Cold worked pure copper loses its strength between 180 to 400 °C. Solid solution alloying has also been used to overcome the weaknesses of pure copper. Although such alloys can withstand higher temperatures than copper, they still lose most of their strength at relatively low temperatures,¹¹ approximately half the solidus temperature (K). Further, alloying often causes a significant decrease in conductivity.

To overcome these shortcomings, copper has also been strengthened by placing finer particulate compounds into its matrix. This can be done either by age hardening or dispersion strengthening. In age hardening, particles are precipitated from a metastable solution into the matrix of the base material. These particles inhibit the slip of grain boundaries and thus increase

¹⁰ SCM Metal Products, "GLIDCOP: Copper Dispersion Strengthened with Aluminum Oxide," Research Triangle Park, NC, 1994.

¹¹ American Society for Metals, *Metals Handbook*, 9th Edition. Metals Park, OH: ASM, Vol. 7, pp. 710-717.

the strength of the material. These materials perform very well at room temperature, but the precipitation hardening effects are lost when exposed to temperatures above those of the initial heat treatment, since these particles grow back into solution. Dispersion strengthening overcomes this problem by using stable compounds as the dispersoids.¹² Since these compounds are stable, they do not go into solution when the temperature is raised. Alloy C15715 contains 0.3 % aluminum oxide powder by weight. The aluminum oxide lends strength to the copper matrix, but at the same time has a minimal effect on important physical properties of the matrix material, such as thermal conductivity and thermal expansion coefficient, owing to the small amounts of oxide used. Thus, C15715 has both a high thermal conductivity (365 W/m·K) and a high yield strength (approximately 400 MPa) at room temperature and exhibits little softening at high temperature. Our samples were cold worked to a hardness of HO4.

Molybdenum is a refractory metal and frequently used in high temperature applications. TZM alloy is a powder metal product and contains 0.5 % Ti and 0.08 % Zr; our samples were cold worked and have a yield strength of approximately 860 MPa with a thermal conductivity of approximately 120 W/m·K. These properties are evaluated at 20 °C.

The objective in selecting the dimensions and liquid speed of the array was to divide the thermal resistance evenly between the faceplate and the liquid. Estimates of the mechanical and thermal stress limits of the faceplate showed that it must be 2 to 3 mm thick in order to avoid yielding during operation if it is made of dispersion strengthened copper. To balance the solid and liquid thermal resistances, h_{avg} must be in the range of 200,000 W/m²·K.

2.3.4 Clamp

The clamp has been carefully designed in an effort to limit thermal stresses. It is a 0.51 cm (0.2 in.) thick sheet of stainless steel with a 0.13 cm (0.05 in.) protruding lip. The faceplate is pressed between this lip and the O-ring as shown in Figure 8. This configuration closely resembles a simple support and will help limit the thermal stresses in the faceplate by facilitating the lateral expansion of the plate during heating.

¹² American Society for Metals, *Metals Handbook*, 9th Edition. Metals Park, OH: ASM, Vol. 7, pp. 710-717.

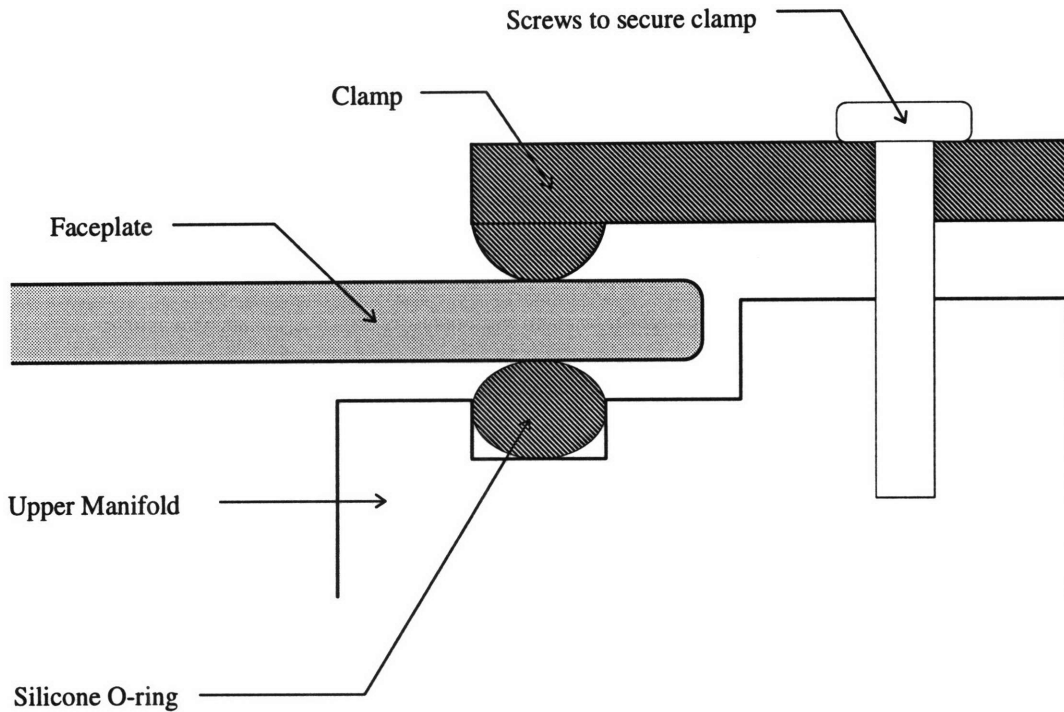


Figure 8 Faceplate clamping configuration.

2.3.5 Temperature Measurements

Temperature measurements were made over the forward surface of the heater film using type K thermocouples. Using high temperature cement or Kapton tape, these thermocouples were attached as described in Table 1. The (x, y) coordinates are measured from the lower left corner of the heater. The heater dimensions are 5.1 by 2.0 cm (2.0 by 0.8 in.). The heater surface temperature measurements were averaged and used to compute the average total temperature difference, ΔT , between the heater surface and the bulk inlet temperature of the water. The heaters are described in detail in Section 6.

Table 1 Locations for thermocouples 1 - 7 when (x,y) is measured from the lower left corner of the heater.

Data Set	1	2	3	4	5	6	7
A	(1.5,0.3)	*	(1.5,0.6)	(0.8,0.2)	(0.8,0.6)	(0.2,0.6)	(0.2,0.2)
B	(1.5,0.7)	*	(1.5,0.2)	(0.7,0.3)	-	(0.4,0.6)	(0.3,0.1)
C	(1.7,0.6)	*	(1.1,0.4)	(1.5,0.2)	-	(0.3,0.1)	(0.5,0.5)
D	(1.6,0.7)	*	(1,1,0.5)	(1.6,0.2)	-	(0.2,0.2)	(0.2,0.6)
E	*	(1.9,0.6)	(1.3,0.5)	(1.4,0.2)	(0.7,0.6)	(0.7,0.2)	-
F	-	(1.5,0.1)	-	(1.1,0.4)	(0.6,0.5)	(0.7,0.2)	-
G	-	(1.6,0.2)	(1.0,0.6)	(1.3,0.3)	(0.7,0.6)	(0.7,0.4)	-

*Thermocouple was attached to the side of the plate on top of insulating ceramic layer.

2.4 Flow Loop Theoretical Calculations

2.4.1 Temperature Rise In The Flow Loop

The temperature rise across the cooling module, neglecting viscous dissipation, can be calculated from the following,

$$q = \dot{m}c_p \Delta T_{bulk} \quad (2.2)$$

where $\Delta T_{bulk} = T_{out} - T_{in}$ is the bulk temperature increase of the liquid passing through the module (K). At a heat flux of 50 MW/m², the heater power is approximately 71 kW and the calculated temperature rise is 3.9 °C. For a heat flux of 20 MW/m², $\Delta T_{bulk} = 1.6$ °C for an operating volume flow rate of 4.41 L/s (70 gpm). The thermocouples placed before and after the cooling section verify this. Higher liquid temperatures obviously occur within the boundary layer on the faceplate.

The 1.89 m³ (500 gallon) reservoir supplying the flow loop also acts as the heat sink and thus liquid temperatures will rise during operation. Running the system at a heat flux of 50 MW/m² causes liquid temperatures to rise at a rate of 32.5 °C/hour. Note, there is also a significant heat load from the pump.

2.4.2 Pressure Drop Calculations

The pressure drops have been revised for a flow rate of 70 gpm. Pressure drops for the new components have been calculated as shown in Table 2. Therefore, for a flow rate of 4.41 L/s (70 gpm), the total calculated pressure drop from various components along the flow loop excluding the nozzles is 73.1 kPa (10.6 psi), without any back pressure from the second flow regulating valve. The 70 gpm flow rate corresponds to a pressure rise of 2.14 MPa (310 psi) across the pump. Thus, a pressure drop of approximately 2.07 MPa (300 psi) is expected across the nozzles if the system operates at a flow rate as high as 70 gpm after all the components have been installed. We can conclude that during operation, roughly 97 % of the system pressure drop occurs across the nozzles.

Table 2 Minor pressure losses at 70 gpm.

No.	Description	Qty.	h_{loss} (m)	ΔP (Pa)
High Pressure				
1	Pump to 2½" pipe entrance	1	0.052	503.31
2	Pipe 2½" to 2" (gradual)	1	0.002	20.68
3	Long radius elbow (radius of 3", NPT 2")	3	0.176	1709.87
4	Globe valve (2" fully open)	1	1.370	13292.88
Low Pressure				
5	Reservoir to 2" pipe entrance	1	0.106	1027.30
6	Ball valve (fully open)	1	0.012	117.21
7	Pipe 2" to 2½" (sudden)	1	0.019	186.16
8	Pipe to pump entrance	1	0.104	1013.51
9	Manifold exit to 1" contraction	1	1.194	11707.12
10	Pipe 1" to 1½" (gradual)	1	0.307	3012.96
11	Globe valve (1½" fully open)	1	4.115	40361.28
12	Pipe 1½" to 2" (gradual)	1	0.018	172.37
Total			7.475	73124.65

2.4.3 Calculation Of The Manifold's Contour

To obtain uniformly divided flow from the nozzles, the manifold was contoured to maintain a constant static pressure along it. The following equation was used to determine the variation of cross sectional area, A , with length along the manifold, x , where x is measured from the dead end,

$$\frac{A}{A_L} = \left[\left(1 + \frac{fL}{D_L} \right) \left(\frac{x}{L} \right)^{\frac{1}{2}} - \frac{fL}{2D_L} \frac{x}{L} \right]^2 \quad (2.3)$$

where L is the length of the manifold, $A \cdot L$ the flow area at the beginning of the manifold, f the friction factor for fully developed flow and D_L is the hydraulic diameter. For our high pressure manifold, $A \cdot L = 40.645 \text{ cm}^2$ (6.3 in²), $L = 7.62 \text{ cm}$ (3 in.), $D_L = 6.28 \text{ cm}$ (2.47 in.) and $f \approx 0.023$. Figure 9 shows the graph of A vs. x for the manifold.

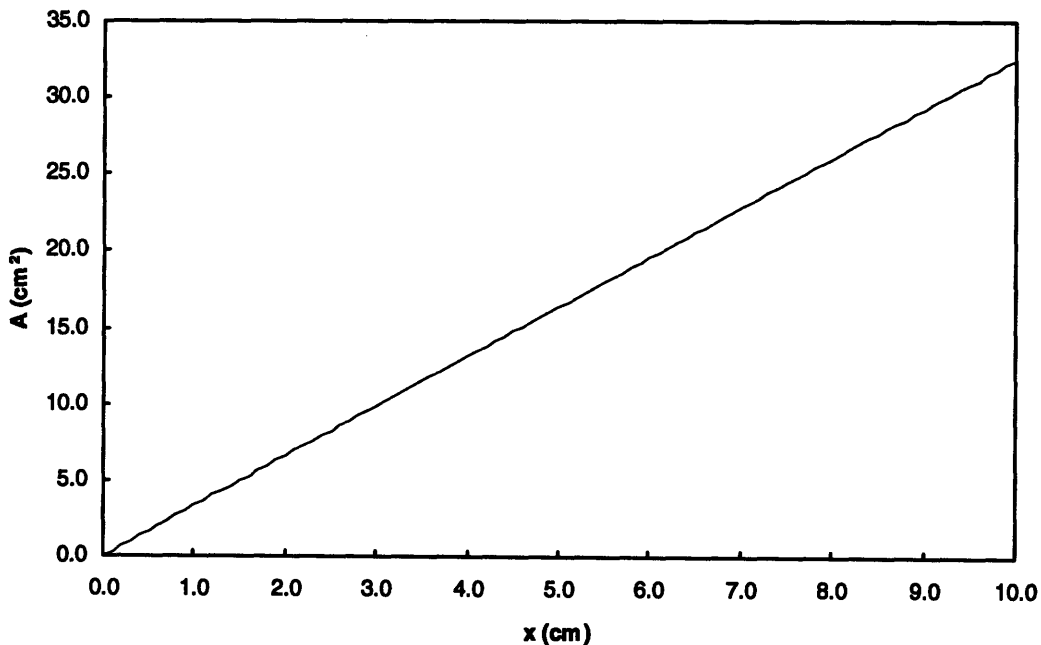


Figure 9 Area normal to the liquid flow in the high pressure manifold.

2.4.4 Stresses In The Nozzle Plate

Due to the geometrical symmetry of the plate and the loading, a one quarter plate model was utilized as a means to increase the number of nodes per unit area of the plate.¹³ The model consisted of triangular (3 node), 6 degree of freedom, shell type elements with bending and membrane capabilities and a total of 1240 elements. The zone of highest stress occurs at the central, outer edge of the plate. These stresses are well below yield stress.

2.5 Cooling Module Experimental Performance

During operation, with both globe valves fully open, 97 % of the pressure drop in the flow loop occurs across the cooling module and is related to the average nozzle outlet velocity u_j approximately by,

$$\Delta P = 1.5 \left(\frac{1}{2} \rho u_j^2 \right) \quad (2.4)$$

which is in close agreement with the analytical result of Equation (2.1).

Liquid flow through the cooling module was measured by varying the system back pressure. The pressure drop across the cooling module, as a function of the system flow rate, is illustrated in Figure 10. Operation with both pressure regulating valves fully open yielded a steady state flow rate of 4.48 L/s (71.0 gpm). The corresponding jet velocities were determined to be 52 m/s (170 ft/s). As the back pressure was increased from 36.5 kPa (5.3 psi) to 739.8 kPa (107.3 psi), the flow rate dropped from 4.48 L/s (71.0 gpm) to 3.73 L/s (59.1 gpm).

An elevated pressure in the upper manifold (back pressure) is desirable in that it raises the saturation temperature of the water and boiling that may occur on the rear surface of the faceplate (and corresponding concerns about CHF). For this reason, all experiments were performed with a back pressure of 579.2 kPa (84.0 psi), limiting the flow rate to 3.94 L/s (62.5 gpm) and the jet velocities to 46.5 m/s (152.6 ft/s) for the 14 nozzle configuration. The corresponding saturation temperature is 157 °C.

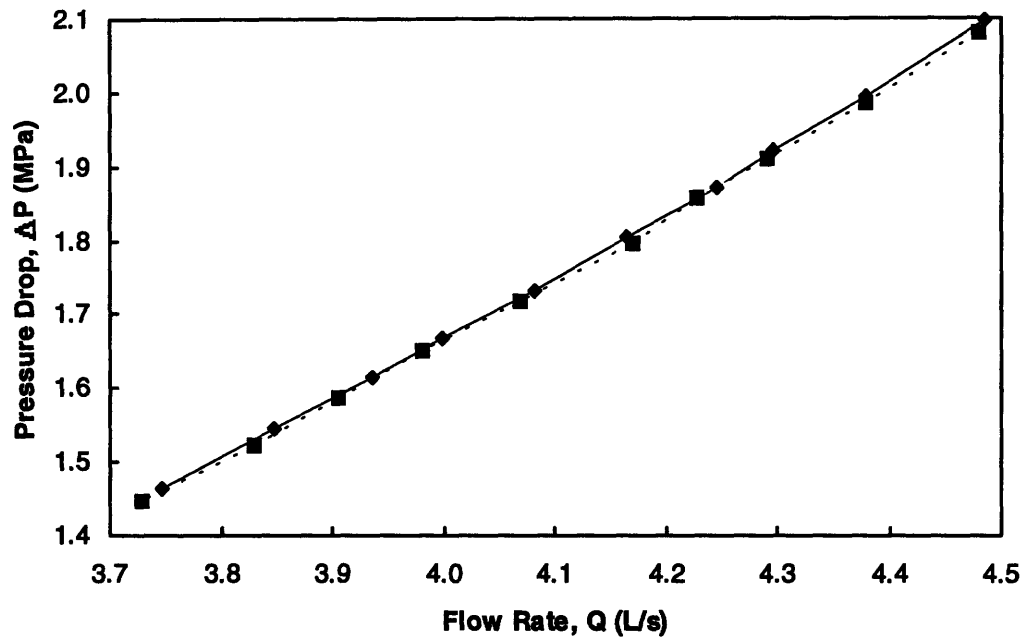


Figure 10 The cooling module pressure drop, ΔP , as a function of the system flow rate, \dot{Q} .

Flow through the cooling module, with no heating, results in a slight temperature increase due to viscous dissipation. A first law balance for the cooling module yields the following relationship for the temperature rise as a function of the cooling module pressure loss,

$$\Delta T_{bulk} = \frac{\Delta P \cdot \dot{Q}}{\dot{m}c_p} = \frac{\Delta P}{\rho c_p} \quad (2.5)$$

This result is in good agreement with the average, measured temperature rise of $\Delta T_{bulk} = 0.4 \text{ }^\circ\text{C}$ ($0.7 \text{ }^\circ\text{F}$), without heating.

¹³ J.H. Lienhard V, R.S. Dahbura, H.F. Younis, and C.H. Oh, 1996, "Large Area Jet-Array Cooling Modules for High Heat Fluxes," *High Heat Flux Engineering III*. SPIE Vol. 2855, pp. 66-81, 1996.

3. Cooling by Impinging Jets

3.1 Introduction

Past work¹⁴ with free surface circular liquid jets has shown that jets operating in the range of 100 m/s can carry fluxes as high as 400 MW/m². These results have made the use of impinging liquid jets attractive in our application, provided we can reach the desired liquid velocities while suppressing boiling burnout and provided that the faceplate survives the mechanical and thermal stresses. If sufficient liquid pressure can be maintained, boiling can be avoided and critical heat flux limitations to h will not create an obstacle. These issues are discussed in more detail later; here, we focus our attention on the heat transfer characteristics and hydrodynamics of impinging liquid jets.

High velocity liquid jets produce especially thin boundary layers on the impingement surface and as a result very high heat transfer coefficients can be attained. Water jets at velocities close to 50 m/s can easily produce heat transfer coefficients of 200,000 W/m²·K or so over a circle having a diameter of roughly 1.5 times the diameter of the jet.

3.2 Free Surface Jets

Previous work on single free surface jets has shown the stagnation zone of an impinging jet to be in the range $0 < r/d < 0.787$, where r is the radial distance from the stagnation point and d is the jet diameter.¹⁵ It has been experimentally verified that this region is of nearly constant Nusselt number. Beyond the stagnation zone, h drops rapidly with radius,^{16,17} as a result of growth of the boundary layer and the flow's deceleration in the wall jet zone. Consequently, h drops by about 50 % from the stagnation zone value at a radius of $4d$ to $6d$.

¹⁴ X. Liu and J.H. Lienhard V, "Extremely High Heat Fluxes Beneath Impinging Liquid Jets," *J. Heat Transfer*, Vol. 115, pp. 472-476, 1993.

¹⁵ X. Liu, J.H. Lienhard and J.S. Lombara, "Convective Heat Transfer by Impingement of Circular Liquid Jets," *J. Heat Transfer*, Vol. 113, pp. 571-582, 1991.

¹⁶ J.H. Lienhard V, "Liquid Jet Impingement," *Annual Review of Heat Transfer*, (C.L. Tien, ed.), Vol. 6, Ch. 4. New York: Begell House, 1995, pp. 199-270.

¹⁷ H. Martin, "Heat and Mass Transfer Between Impinging Gas Jets and Solid Surfaces," *Advances in Heat Transfer*, Vol. 13. New York: Academic Press, 1977, pp. 1-60.

Pressure also drops with distance from the stagnation point in a Gaussian manner. Liu et al.¹⁸ analytically obtained pressure distributions for laminar liquid jets including surface tension effects. For infinite Weber number (as in our case), the pressure drops to 70 % of its stagnation point value at $r/d = 0.75$. The stagnation point pressure is defined as

$$P_{stag} = P_{ambien} + \frac{1}{2} \rho u_j^2 \quad (3.1)$$

for u_j the jet speed and ρ the liquid density. Thus, a 50 m/s water jet has a stagnation point pressure of 1.34 MPa (193 psia) which drops to 400 kPa (58 psia) at $r/d = 0.7$ and to the ambient pressure beyond $r/d = 1$.

Several investigators have examined stagnation zone Nusselt numbers beneath impinging jets. For free surface turbulent liquid jets issued from long tubes, Gabour and Lienhard found,¹⁹

$$Nu_d \equiv \frac{hd}{k} = 0.278 Re_d^{0.633} Pr^{1/3} \quad (3.2)$$

where the jet Reynolds number, $Re_d = u_j d / \nu$, should be between 25,000 and 85,000 and the liquid Prandtl number, $Pr = \nu / \alpha$, should be > 1 . Here, d is the nozzle's inside diameter, ν is the liquid kinematic viscosity, α is the liquid thermal diffusivity, and k is the liquid thermal conductivity. The heat transfer coefficient increases with jet speed and decreases with jet diameter as $u_j^{0.633} d^{-0.367}$.

A simple calculation reveals how high the heat fluxes supported by impinging jets can be. Note that these calculations are extrapolations and skepticism should be exercised while using them. For a 2.78 mm water jet at 50 m/s having a temperature $T_{jet} = 30$ °C and cooling a wall at $T_{wall} = 100$ °C, the Reynolds number is of the order 300×10^3 (physical properties are evaluated at the film temperature, 65 °C) and the equation may be extrapolated to predict h values above 200,000 W/m²·K. With $T_{wall} - T_{jet} = 70$ °C, the stagnation point heat flux $q = h \cdot \Delta T$ would be greater than 14 MW/m². If the wall were at the local saturation temperature of 193 °C, the heat flux at the saturation point would be 33 MW/m² or higher.

¹⁸ X. Liu, L.A. Gabour and J.H. Lienhard V, "Stagnation-Point Heat Transfer During Impingement of Laminar Liquid Jets: Analysis Including Surface Tension," *J. Heat Transfer*, Vol. 115, pp. 99-105, 1993.

Other investigators have examined stagnation point Nusselt numbers for free surface jets in configurations that involve pipe type nozzles. Stevens and Webb²⁰ have examined jets in the range $4,000 < Re < 52,000$ with varying z/d where z is the nozzle to target separation and d is the nozzle diameter. Pan et al.²¹ investigated Re numbers between 16,500 and 43,500 and for a fixed nozzle to plate spacing $z/d = 1$. Their correlations, however, give Nusselt number values lower than those obtained from Equation 3.2 since they document a lower exponential dependence on Reynolds number. Faggiani and Grassi²² as well as Gabour and Lienhard¹⁹ have found a stronger dependence of stagnation point Nusselt number on Reynolds number at high Reynolds numbers, and the exponent 0.633 in Equation (3.2) more accurately correlates stagnation point Nusselt number data at such high Re values.

3.3 Submerged Jets

In order to assure that no air pockets exist between the face plate and our impinging jets (this could dramatically increase the cooling side thermal resistance), all the air is driven out of the system through bleeder valves in the manifolds. Thus, the jets are submerged. Submerged jets have a somewhat different behavior from free surface jets beyond the stagnation zone. However, if the target is kept within the potential core of the jet (nozzles within 5 to 6 jet diameters of the faceplate), the stagnation zone of both types of jet are identical.²³ This is due to the fact that at such a spacing the core of the jet has not begun to mix with the surrounding fluid. We thus chose a nozzle to plate spacing of 1 to 2 times the jet diameter for our initial studies. For free surface jets, the effect of varying z/d on the stagnation Nusselt number was found to be negligible¹⁹ over a z/d range of 1 to 20. In submerged water jets, however, it has been observed

¹⁹ L.A. Gabour and J.H. Lienhard V, "Wall Roughness Effects on Stagnation-Point Heat Transfer Beneath Impinging Liquid Jets," *J. Heat Transfer*, Vol. 116, No. 1, pp. 81-87, 1994.

²⁰ J. Stevens and B.W. Webb, "Local Heat Transfer Coefficients Under an Axisymmetric, Single-Phase Liquid Jet," *J. Heat Transfer*, Vol. 113, pp. 71-78, 1991.

²¹ Y. Pan, J. Stevens and B.W. Webb, "Effect of Nozzle Configuration on Transport in the Stagnation Zone of Axisymmetric Impinging Free-Surface Liquid Jets: Part 2 — Local Heat Transfer," *J. Heat Transfer*, Vol. 114, pp. 880-886, 1992.

²² S. Faggiani and W. Grassi, "Round Liquid Jet Impingement Heat Transfer: Local Nusselt Numbers in the Region with Non Zero Pressure Gradient," *Proc. of the Ninth Int. Heat Trans. Conf.*, Vol. 4, pp. 197-202, 1990.

²³ J.H. Lienhard V, "Liquid Jet Impingement," *Annual Review of Heat Transfer*, (C.L. Tien, ed.), Vol. 6, Ch. 4. New York: Begell House, 1995, pp. 199-270.

that stagnation Nusselt numbers increase to a maximum²⁴ at $z/d = 5$. This has been attributed to greater turbulence levels with greater nozzle to plate separations associated with the increased mixing of the jet with its surroundings until it reaches a maximum level. Beyond $z/d = 5$, the Nusselt numbers drop monotonically from this peak. The increased mixing comes at the expense of a decreased mean speed of the jet. Larger stand-off distances allow more drag by surrounding liquid on the jet, while smaller distances allow for higher fluid momentum on the impinging wall and keep the downstream wall boundary layers thinner. Nozzle-to-target spacing tighter than $z/d = 1$ raises the flow resistance and the required supply pressure without producing a significant improvement in h .

Because of the similarity in stagnation zones, it is reasonable to assume that the pressure distributions and Nusselt numbers will be similar to those of free surface jets in the stagnation region. Sun et al.²⁴ have performed experiments to analyze the stagnation Nusselt numbers and Nusselt number distributions for submerged water jets in the Reynolds number range $5,000 < Re < 36,000$. Their stagnation zone Nusselt numbers generally agree very well with Steven and Webb's data for free surface jets,²⁵ but are significantly lower than those given by Equation (3.2). This can again be attributed to the lower values of Reynolds number studied (as was discussed for free surface case).

The behavior of single free surface and submerged jets beyond the stagnation zone will not be discussed further here because it does not apply to our case. We have radial interaction between the adjacent jets just outside the stagnation zone. Experimental evidence shows that the stagnation point heat transfer of jets in arrays is not significantly affected by the adjacent jets,²⁶ but the surrounding flow field is favorably changed by the radial interaction as discussed below.

²⁴ H. Sun, C.F. Ma and W. Nakayama, "Local Characteristics of Convective Heat Transfer From Simulated Microelectronic Chips to Impinging Submerged Round Water Jets," *J. Electronic Packaging*, Vol. 115, pp. 71-77, 1993.

²⁵ J. Stevens and B.W. Webb, "Local Heat Transfer Coefficients Under an Axisymmetric, Single-Phase Liquid Jet," *J. Heat Transfer*, Vol. 113, pp. 71-78, 1991.

²⁶ Y. Pan and B.W. Webb, "Heat Transfer Characteristics of Arrays of Free-Surface Liquid Jets," *J. Heat Transfer*, Vol. 117, No. 4, pp. 878-883, 1995.

3.4 Jet Arrays

One can conclude from Section 3.2 that reduced cooling performance beyond the stagnation zone of single jets can pose a problem in high heat flux systems, especially that pressures start to drop rapidly as well. Thus, to eliminate some of the shortcomings of jets in cooling at large distances from the stagnation point, our cooling modules use an array of closely spaced jets. The faceplate is effectively divided into sub-regions associated with each individual jet, within which heat transfer coefficient remains closer to the stagnation zone value. Fewer data are available for arrays of liquid jets, particularly at high Re_d . The hydrodynamics between the various jets differ considerably from conditions for single jet cooling. In particular, liquid from adjacent jets collides along the lines of symmetry between nozzles, creating secondary stagnation zones on the wall; for example, the secondary stagnation zone will form a hexagon surrounding the central jet in our array. Within these stagnation zones, momentum conservation requires the pressure to rise significantly above the ambient pressure as the liquid turns 90° and moves normally away from the wall; in addition, h has also been observed to rise in experimental studies.

The specific variation of h with radial distance from the stagnation point depends on Reynolds number, nozzle-to-nozzle spacing, and array planform; however, existing data²⁷ for similar configurations at lower Reynolds numbers than ours show a minimum h of about 75 % of the stagnation value at a radius of about d and a secondary peak of about 90 % of the stagnation value in the secondary stagnation zone (radius of $1.8d$). A correlation for the average heat transfer coefficient, h_{avg} , of an array of nozzles having a center-to-center spacing s is²⁷

$$Nu_{avg} \equiv \frac{h_{avg} d}{k} = 0.225 Re_d^{2/3} Pr^{0.4} e^{-0.095s/d} \quad (3.3)$$

This equation is based on data for water with $5000 < Re_d < 20000$ and $2 < s/d < 8$. Our Reynolds numbers are ten times higher than the upper limit of the correlation; nonetheless, the result provides some guidance as to what fraction of the stagnation point heat transfer coefficient will be achieved as an average beneath the jet array. For our array, $s/d = 3.6$. On the

²⁷ Y. Pan and B.W. Webb, "Heat Transfer Characteristics of Arrays of Free-Surface Liquid Jets," *J. Heat Transfer*, Vol. 117, No. 4, pp. 878-883, 1995.

basis of this equation and various published data, we estimate that the average heat transfer coefficient, h_{avg} under our jet array will be in the range of 80 - 85 % of the stagnation value as given by Equation (3.2).

3.5 Flow and Temperature Simulations²⁸

Numerical simulations of the flow in the region surrounding a single nozzle were made using the FLUENT package.²⁹ Turbulent transport was modeled using the renormalization group $k - \epsilon$ model.³⁰ The geometry and adaptive numerical grid are shown in Figure 11. The simulation is axisymmetric, and the secondary stagnation zone at the outside of the simulation domain is modeled as a circle of 5 mm (0.197 in.) radius having a symmetry boundary condition (zero gradients). The nozzle outlet is situated 2 jet diameters behind the faceplate. The flow speed at the nozzle outlet was varied, as was the heat flux applied to the outer surface of the dispersion strengthened (DS) copper plate. A 2 mm (0.079 in.) thick plate was used for all the runs.

Using the FLUENT package, simulation runs have been used to give approximate pressure distributions at jet velocities of 20, 30 and 40 m/s. The pressure results were very consistent with our expectations (see Section 3.2). The highest pressure region in all three cases was at the stagnation point, with the pressure dropping to a minimum between the primary and secondary stagnation zones at $r/d = 1.2$. When the nozzle-to-target separation is reduced, the minimum pressure is reduced. At the secondary stagnation zone, the pressure rises slightly again due to conservation of momentum. Figure 12 shows the radial pressure distribution on the liquid-side of the copper plate.

²⁸ C.H. Oh, Idaho National Engineering Laboratory, Idaho Falls, ID.

²⁹ FLUENT, Version 4.3. Lebanon, NH: Fluent, Inc., 1995.

³⁰ V. Yakhot and S.A. Orszag, "Renormalization Group Analysis of Turbulence: Basic Theory," *J. Scientific Computing*, Vol. 1, No. 1, pg. 3, 1986.

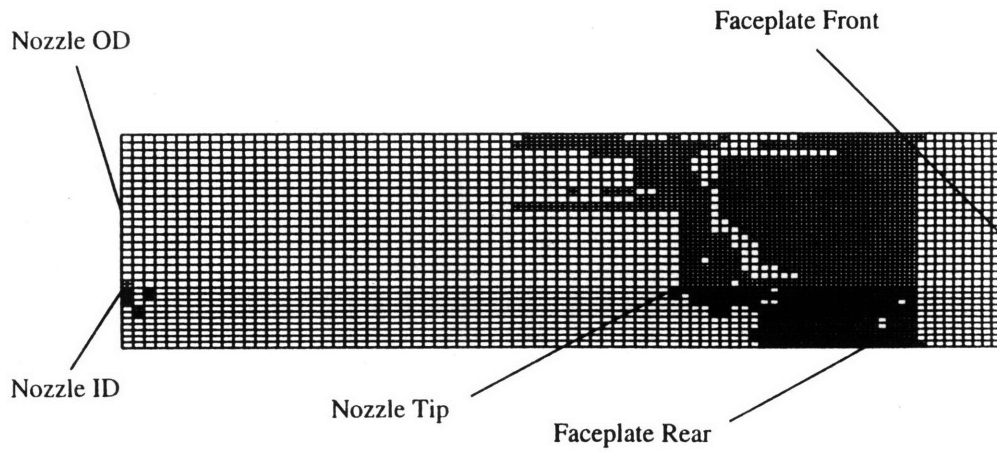


Figure 11 Axisymmetric simulation configuration and numerical grid.

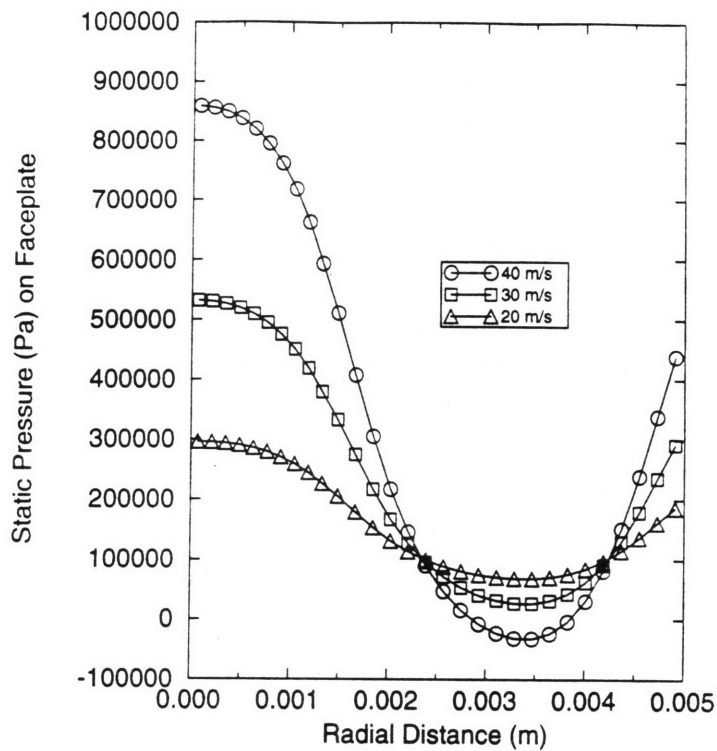


Figure 12 Calculated variation of pressure as a function of radial distance from stagnation point for $u_j = 20, 30,$ and 40 m/s at 20 MW/m^2 .

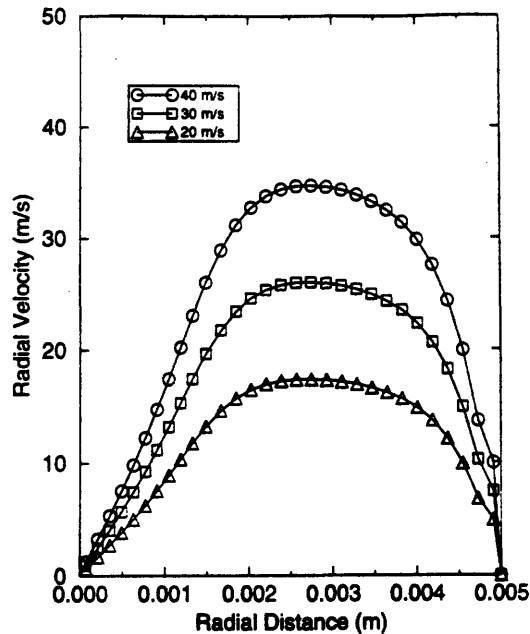


Figure 13 Radial liquid velocity just outside the boundary layer as a function of the radial distance from the stagnation point for $u_j = 20, 30,$ and 40 m/s at 20 MW/m^2 .

A primary concern for jet array impingement cooling at these high fluxes is the possibility of boiling in the low pressure regions between jets. Even though boiling tends to increase the convective heat transfer locally, it interferes with the flow downstream of the jet and can eventually lead to burnout.³¹ Thus, in order to tackle this problem, we may apply a back pressure to the low pressure manifold to raise the pressure above the saturation value and suppress boiling. At 20 MW/m^2 and with a jet velocity of 40 m/s , the simulations show that the wall temperature on the cooled side is nearly isothermal with $T_{\text{wall}} \approx 145^\circ\text{C}$. The corresponding saturation pressure P_{sat} is 415 kPa (60 psi). If no back pressure is imposed, boiling is possible beyond $r = 1.8 \text{ mm}$ ($r/d > 0.65$) from the jet stagnation point where the pressure drops below the saturation pressure corresponding to the local temperature. Addition of a 552 kPa (80 psia) back pressure raises the pressure above P_{sat} over the entire faceplate. This back pressure can be added with the aid of the regulating globe valve at the exit of the upper manifold.

³¹ Y. Katto and M. Shimizu, "Upper Limit of CHF in the Saturated Forced Convection Boiling on a Heated Disk with a Small Impinging Jet," *J. Heat Transfer*, Vol. 101, pp. 265-269, May 1979.

The stagnation point pressure for a 40 m/s jet is 891 kPa (129 psia) for 1 atm ambient pressure. Therefore, with a back pressure of 552 kPa (80 psia), P_{stag} is raised to 1.44 MPa (209 psia). This would be the maximum pressure on the faceplate and is close to the value of 1.24 MPa (180 psia) that we used for our stress simulations.

The FLUENT simulations also numerically modeled the radial component of liquid velocity just outside the boundary layer, the liquid and hot side temperature distributions as well as heat transfer coefficient distribution on the impingement front. Figure 13 shows the radial component of the liquid velocity as a function of radius for three different nozzle velocities and Figure 14 shows the temperature on the liquid side of the copper plate. Figure 15 shows the temperature on the hot side of copper plate for the same conditions. The radial variation is small relative to the temperature difference through the thickness of the plate. Figure 16 shows the radial distribution of the heat transfer coefficient.

The results of these simulations differ somewhat from our previous predictions in Section 3. The heat transfer coefficient reaches a peak at the stagnation point and is of the order 200,000 W/m²·K. The recalculated value from extrapolation of Equation (3.2) for a 40 m/s jet, with these conditions is $h = 264,000$ W/m²·K. This is based on a jet temperature $T_j = 30$ °C and a wall temperature $T_{wall} = 145$ °C from the FLUENT run (giving a film temperature $T_f \approx 360$ K). If further increase in h_{avg} is needed, the liquid side of the faceplate may be roughened to 10 to 20 μm rms. Past studies³² have shown that such roughness raises stagnation zone heat transfer by up to 50 %.

Although the stagnation heat transfer coefficients agree well with the simulations, the behavior of h beyond the stagnation zone $r > 0.7d$ (i.e. $r > 2$ mm), is different from what was expected. The simulations show that the heat transfer coefficient does not reach a minimum value of about 75 % the stagnation value between the primary and secondary stagnation zones, but rather smooths out with r and drops at the secondary stagnation zone. The behavior between stagnation zones can be attributed to the effect of confining the jets, but the sharp drop off in h at the secondary stagnation region may be due to limitations in the simulation.

³² L.A. Gabour and J.H. Lienhard V, "Wall Roughness Effects on Stagnation-Point Heat Transfer Beneath Impinging Liquid Jets," *J. Heat Transfer*, Vol. 116, No. 1, pp. 81-87, 1994.

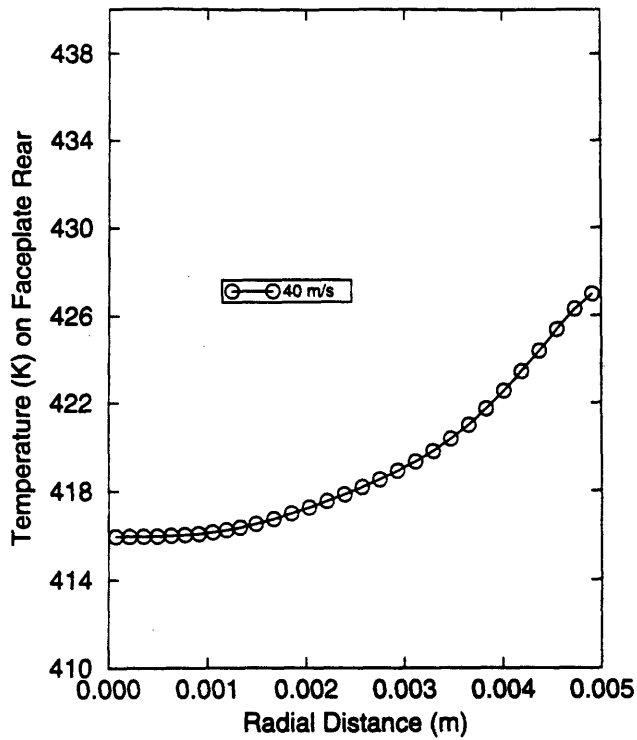


Figure 14 Liquid-side temperature of copper as a function of radial distance from the stagnation point for $u_j = 40$ m/s at 20 MW/m^2 .

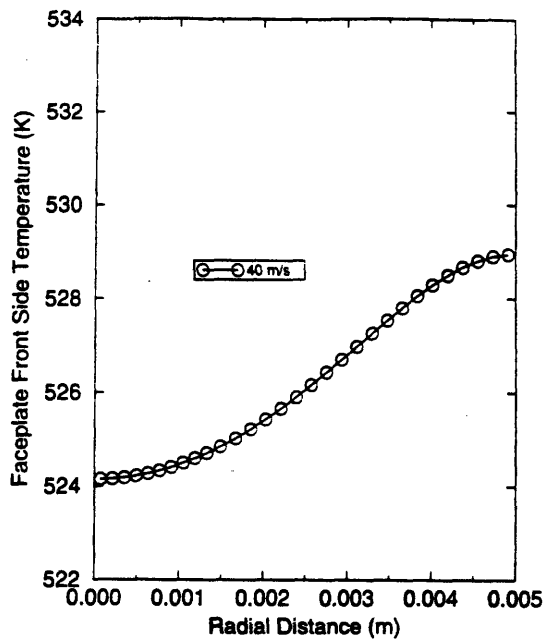


Figure 15 Hot side temperature of copper as a function of the radial distance from the stagnation point for $u_j = 40$ m/s at 20 MW/m^2 .

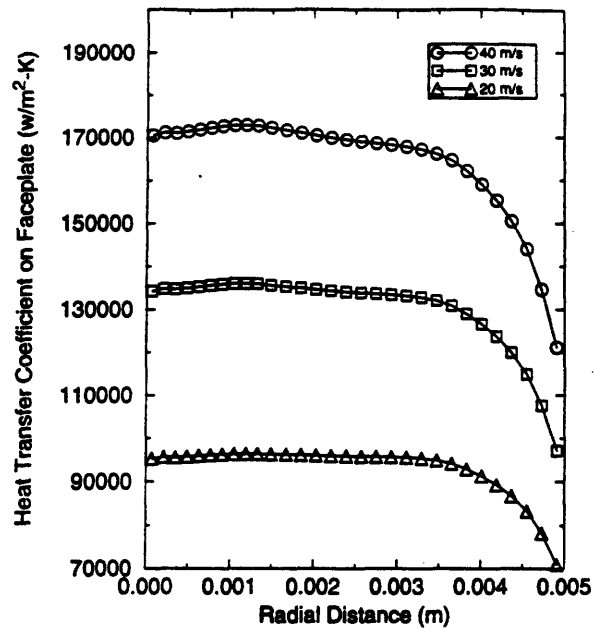


Figure 16 Calculated variation of h as a function of the radial distance from the stagnation point for $u_j = 20, 30,$ and 40 m/s at 20 MW/m².

Owing to the thick wall of our nozzle and the tight nozzle-to-target separation we use ($1d$ to $2d$), the specific nozzle arrangement influences the radial variation of h enough that published data do not predict our h with any great precision. However, this nozzle configuration confines the flow, and a somewhat similar behavior was observed for confined, submerged jets. Previous work on single submerged and confined jets³³ also showed the presence of a recirculation pattern that moved further away from the stagnation point with increasing z/d . This was apparent in our flow simulations for $z/d = 1$ and contributed to heat transfer coefficients of higher magnitudes than at the stagnation zone in the range of $1 < r/d < 2$. As z/d is increased, the location of this recirculating region moves further downstream and in our runs for $z/d = 2$, it is speculated that the circulating region is driven out of the confined area and its convective enhancement effects are lost. It is not entirely clear, however, why the heat transfer coefficient distribution smooths out in the manner shown in Figure 16.

³³ S.V. Garimella and R.A. Rice, "Confined and Submerged Liquid Jet Impingement Heat Transfer," *J. Heat Transfer*, Vol. 117, pp. 871-977, 1995.

Since the heat transfer coefficient is nearly constant, it is not surprising to see that the temperatures vary only minimally in the radial direction on the hot and cold sides. For 20 MW/m² imposed heat flux and jets operating at 40 m/s, the heat flux surface is nearly isothermal with the temperature ranging between 524 K to 529 K; a maximum temperature difference of 11 °C in the radial direction. The liquid side temperatures of the faceplate behave similarly, with a maximum variation of 9 °C and a range from 416 K to 427 K.

4. Thermal and Mechanical Faceplate Stresses

The stresses occurring in the faceplate are a function of temperature differences, heater geometry, liquid jet pressure loads, mechanical boundary loads at the faceplate edges, and material properties. Temperature distributions through the thickness of the faceplate may be nonlinear as a result of temperature dependent material properties and three dimensional effects imposed by the heat flux and convective cooling boundary conditions. A complete listing of the temperature dependent material properties used in the numerical analyses is included in Appendix C.

Low faceplate temperatures during operation inhibit softening of the plate and maintain a high yield stress and low degree of thermal expansion. These characteristics tend to increase the maximum attainable heat flux prior to failure. Previous studies^{34,35,36} have proposed the following figure of merit for the elastic performance of high heat flux materials

$$Q_{efm} \equiv \frac{(1-\nu)k\sigma_Y}{E\alpha} \quad (4.1)$$

The figure of merit represents the flux that causes yielding in a clamped edge plate of unit thickness subjected to the thermal stresses of a uniform heat load. The heat flux at yield, Q_{efm} , is a function of the Poisson's ratio ν , the thermal conductivity k , the yield stress σ_Y , Young's modulus E , and the coefficient of thermal expansion α . Table 3 contains values for various materials; also shown is $\Delta T = Q_{efm}/k$, the temperature difference through a plate of unit thickness at yielding.

³⁴ J.H. Lienhard V and D.S. Napolitano, "Thermal Stress Limits of Plates Subjected to Extremely High Heat Fluxes," *ASME Intl. Mech. Engr. Congress and Exhibition*, Atlanta, November 1996.

³⁵ J.H. Lienhard V and A.M. Khounsary, "Liquid Jet Impingement Cooling in Conjunction with Diamond Substrates for Extremely High Heat Flux Applications," *High Heat Flux Engineering II*, SPIE Vol. 1997, pp. 29-43, 1993.

³⁶ M.A. Abdou et al., "Technical Assessment of the Critical Issues and Problem Areas in High Heat Flux Materials & Component Development," Vol. 2 of "Magnetic Fusion Energy Plasma Interactive and High Heat Flux Components," DOE Office of Fusion Energy Task Group on High Heat Flux Material and Component Development. Los Angeles: Center for Plasma Physics and Fusion Engineering, UCLA, 1984.

Table 3 Thermal and elastic properties of various materials⁴. All values are at room temperature unless otherwise indicated. Properties that have been estimated are italicized. For ductile materials, σ_Y is for 0.2 % offset. For brittle materials, σ_Y is the compressive strength. T_{melt} is the solidus temperature for metallic alloys; for diamond it is the temperature above which pyrolysis occurs. α is based on the total expansion from 20 °C to the indicated temperature.

Material	α (10^{-6} K^{-1})	E GPA	k (W/m-K)	σ_Y MPa	ν	Q_{efm} (MW·mm/m ²)	ΔT (K)	T_{melt} (K)
Diamond (single crystal)	0.8	1050	2100	3000	0.15	6400	3	973
DS Copper (C15715-H04)								1356
20 °C	<i>16</i>	130	365	430	<i>0.3</i>	52.8	145	
200 °C	17.2	<i>120</i>	345	375	<i>0.3</i>	43.6	127	
400 °C	18.8	<i>110</i>	320	307	<i>0.3</i>	33.3	104	
Copper-Cr (C18200-TH04)								1343
20 °C	16.3	130	324	520	<i>0.3</i>	55.6	172	
200 °C	17.2	<i>120</i>	351	441	<i>0.3</i>	55.5	150	
400 °C	18.9	109	364	343	<i>0.3</i>	42.4	117	
Copper-Zr (C15000-TH04)	16.9	129	367	411	0.34	45.7	124	1253
Molybdenum (TZM)								2883
Stress relieved, 21 °C	4.9	315	120	860	<i>0.3</i>	46.8	390	
Stress relieved, 1090 °C	5.6	205	100	435	<i>0.3</i>	26.5	265	
Tantalum (T-222)								3293
Stress relieved, 20 °C	5.9	200	54	950	<i>0.3</i>	30.4	563	
Stress relieved, 1000 °C	6.8	<i>140</i>	59	700	<i>0.3</i>	30.3	514	
Tungsten								3683
Wrought, 500 °C	4.4	388	130	517	0.29	28.0	215	
Recrystallized, 500 °C	4.4	388	130	131	0.29	7.1	54	
Aluminum (7075-T651)								750
20 °C	23.4	72	130	503	0.33	26.0	200	
149 °C	24.3	<i>66</i>	170	188	<i>0.33</i>	13.2	77	
371 °C	25.2	<i>40</i>	172	38	<i>0.33</i>	4.4	25	
Aluminum (6061-T651)								855
20 °C	23.6	70	167	276	0.33	18.8	112	
149 °C	24.2	64	175	2115	<i>0.33</i>	16.8	96	
371 °C	25.3	39	181	12	<i>0.33</i>	1.5	9	
Inconel 713C	10.6	205	11	740	0.3	2.6	238	1533
Stainless 304L (10 % cw)	17.3	193	15	290	0.27	1.0	63	1673

Recently, Lienhard and Napolitano³⁷ have examined the yield limits of circular faceplates subjected to high heat fluxes for various candidate materials. They calculated the thermal stresses in a disk of radius b and thickness H whose rear surface was held at $T_c = 25$ °C and whose front surface was subjected to a Gaussian temperature profile,

$$T_h = T_c + (T_{\max} - T_c)e^{-\left(\frac{2r^2}{a^2}\right)} \quad (4.2)$$

The outer edge of the disk was either simply supported or fixed, and T_{\max} and a were varied.

The values of T_{\max} and heat flux, q , at which the plate stresses reach yield stress are given in Table 4 and Table 5. Note that the stresses depend on the temperature difference, rather than the heat flux, so that plates of different thickness will reach yielding for the same value of T_{\max} but with different values of the flux. The numerical values of $q \cdot H$ in the table correspond to the lowest heat flux though a 1 mm plate which will cause yielding; for other thicknesses, the flux can be found by dividing the tabulated value of H in millimeters.

The results are listed as a function of a/b . Small values of a/b correspond to a localized hot-spot, whereas $a/b \rightarrow \infty$ corresponds to a uniform temperature on the hot surface. In the uniform temperature limit, thermal stresses go to zero in a simply supported plate; here, the upper surface is assumed to reach the melting point temperature of the plate material. In the hot-spot limit, the simply supported and fixed edge disks have the same stresses. Otherwise, stresses are considerably higher for a fixed edge disk, which underscores the value of allowing lateral expansion of the plate so as to relieve membrane stresses.

The tabulated data show that hardened copper alloys are among the best candidates for the faceplate, owing to a combination of high thermal conductivity and high strength. While their strength is lower than some refractory metals, their high conductivity helps limit the upper surface temperature. The dispersion strengthened coppers (e.g., C15715) are particularly attractive, owing to their very good creep characteristics at high temperatures. The DS coppers

³⁷ J.H. Lienhard V and D.S. Napolitano, "Thermal Stress Limits of Plates Subjected to Extremely High Heat Fluxes," *ASME Intl. Mech. Engr. Congress and Exhibition*, Atlanta, November 1996.

retain more strength above 300 - 400 °C than do precipitation hardened Cu alloys such as C18200.

Table 4 Temperature and heat flux at which a simply supported circular plate reaches yield stress during localized heating.³⁸ T_{\max} in K and $q \cdot H$ in MW·mm/m².

Material		<i>a/b</i>				
		0.1	0.4	0.75	1.0	∞
DS Copper (C15715-H04)	T_{\max}	616	633	696	766	1343
	$q \cdot H$	112	118	138	160	323
Chromium Copper (C18200-TH04)	T_{\max}	641	659	711	765	1343
	$q \cdot H$	120	127	146	167	376
Molybdenum (recrystallized)	T_{\max}	556	575	630	705	2883
	$q \cdot H$	35	37	44	53	200
Aluminum (6061-T651)	T_{\max}	461	466	477	491	885
	$q \cdot H$	28	29	31	33	106

Table 5 Temperature and heat flux at which a fixed-edge circular plate reaches yield stress during localized heating.³⁸ T_{\max} in K and $q \cdot H$ in MW·mm/m².

Material		<i>a/b</i>				
		0.1	0.4	0.75	1.0	∞
DS Copper (C15715-H04)	T_{\max}	610	581	525	494	429
	$q \cdot H$	110	100	82	71	49
Chromium Copper (C18200-TH04)	T_{\max}	639	610	555	523	450
	$q \cdot H$	119	109	89	77	52
TZM Alloy (wrought)	T_{\max}	1052	980	841	764	606
	$q \cdot H$	94	86	70	60	41
Tungsten (wrought)	T_{\max}	864	811	714	643	557
	$q \cdot H$	77	71	59	49	38
Molybdenum (recrystallized)	T_{\max}	556	525	478	450	395
	$q \cdot H$	35	31	24	21	13
Aluminum (6061-T651)	T_{\max}	461	455	442	430	400
	$q \cdot H$	28	27	25	23	17

³⁸ J.H. Lienhard V and D.S. Napolitano, "Thermal Stress Limits of Plates Subjected to Extremely High Heat Fluxes," ASME Intl. Mech. Engr. Congress and Exhibition, Atlanta, November 1996.

4.1 2D Stress Analysis

An important parameter governing the maximum faceplate temperature is its thickness. In order to minimize the temperatures, the optimal faceplate design would consist of the minimum thickness required to withstand the force of the impinging liquid jets. Finite element modeling (FEM) has been utilized as a design tool for the stress analysis. Our analysis examines a rectangular DS copper faceplate (Figure 17) of dimensions a by b , simply supported along its edges. The shaded region of dimensions w by l is subject to a uniform pressure.

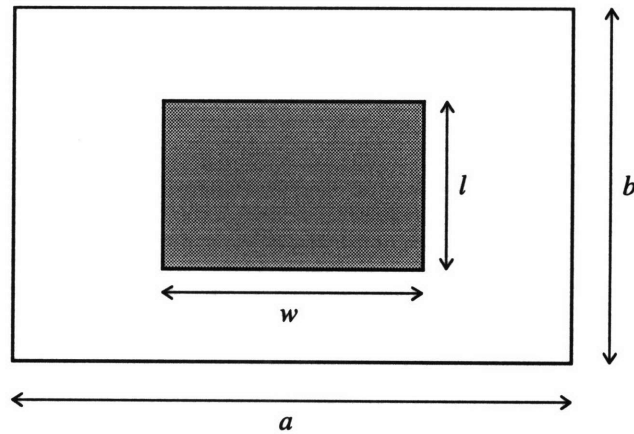


Figure 17 Faceplate configuration. Shaded area is heated.

Finite element simulations were used to determine the pressure at which yielding would occur in the DS copper faceplate as a function of plate thickness for various plate sizes subject to isothermal conditions. The plate was modeled using quadrilateral (4 node), 6 degree of freedom, shell type elements with bending and membrane capabilities. The effects of varying grid resolutions were determined prior to establishing the final model, which consisted of approximately 1100 elements. Stress results are within 5 - 10 % of models utilizing a higher number of elements and nodes. Results show the zone of highest stress to be in the center of the faceplate.

Yielding for the DS copper plate occurs when the von Mises stress reaches the material yield stress (434 MPa for C15715, 820 MPa for TZM). Figure 18 illustrates the result of the finite element simulations. The pressure required to cause yielding increased non-linearly with increasing plate thickness and was highest for the smallest plate. Based on the limits of our flow loop, the maximum operating pressure is 2 MPa and the design thickness of 2.5 mm (yield pressure of 3.41 MPa) provides an adequate safety factor to prevent yielding. The faceplate dimensions in our design are those of the smallest plate shown in the figure. Note, the plate dimensions shown in Figure 18 correspond to the dimensions a and b in Figure 17.

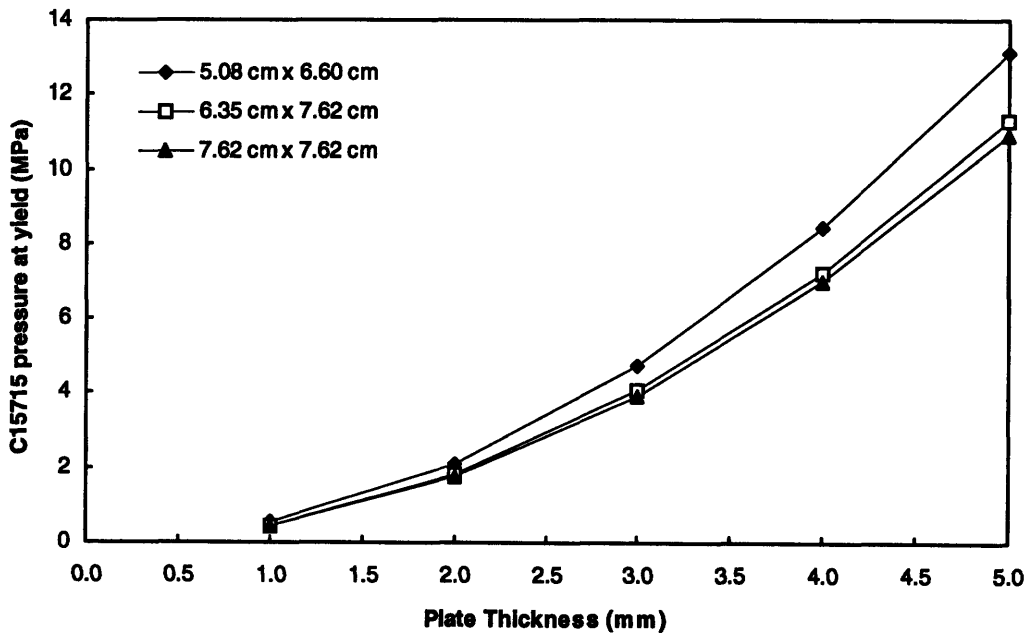


Figure 18 Uniform pressure required to yield an isothermal faceplate.

Results from the finite element simulations were in good agreement when compared with handbook results³⁹ for a similar configuration whose maximum bending stress was described by the following equation,

³⁹ W.C. Young, *Roark's Formulas for Stress and Strain*, 6th Edition. New York: McGraw-Hill, 1989, pg. 459.

$$\sigma_{b,\max} = \beta \frac{q_l w l}{t_f^2} \quad (4.3)$$

where q_l is the magnitude of the distributed pressure load, t_f is the faceplate thickness and β is a factor based on the plate dimensions and the size of the loaded region. The maximum stress described by Equation (4.3) is tensile and occurs at the center of the plate on the heated surface, and lies in a direction parallel to the dimension b . The maximum operating pressure for the molybdenum faceplate was determined using Equation (4.3), where the bending stress was replaced by the yield stress of TZM. Results are shown in Figure 19. The design thickness of 1.81 mm (yield pressure of 3.39 MPa) provides an adequate safety factor to prevent yielding.

The yield stress of DS copper is approximately 50 % lower than the yield stress of (TZM). A design based on DS copper provides a lower bound on the faceplate dimensions a and b . A TZM faceplate of dimensions a by b could be made thinner than its DS copper counterpart, as evident in the results. This is due to TZM's higher yield strength, relative to DS copper.

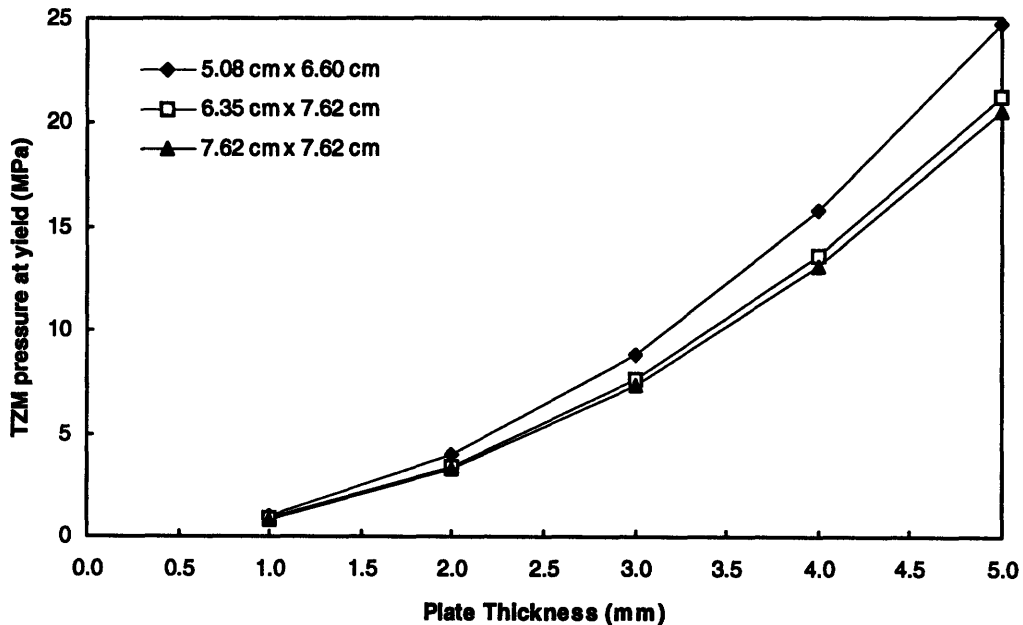


Figure 19 Uniform pressure required to yield an isothermal faceplate.

4.2 3D Thermal and Stress Analysis

Finite element simulations were utilized to determine the combined effects of thermal and mechanical loading of the faceplate. The faceplate was modeled in three dimensions using solid (8 node), 3 degree of freedom elements. The effects of varying grid resolutions were once again determined prior to establishing the final model, which consisted of 1000 elements. As before, stress results are within 5 - 10 % of models utilizing a higher number of elements and nodes. Results for DS copper (C15715) and molybdenum (TZM) are discussed.

Mechanical boundary conditions were used to simulate pressure from the impinging liquid jets and the restrained edges of the plate. The pressure distribution resulting from the liquid jets has been modeled using a series of Gaussian surfaces given by,

$$P(x, y) = P_{stag} \sum_{i=1}^9 e^{-\frac{(x-x_i)^2}{2\sigma^2}} e^{-\frac{(y-y_i)^2}{2\sigma^2}} \quad (4.4)$$

The center of each surface, (X_i, Y_i) , models the stagnation zone of a jet. A stagnation pressure, P_{stag} , of 1.24 MPa (180 psi), corresponding to a jet velocity of 50 m/s, was utilized. As the distance from the jet center increases, the pressure decreases. Due to the geometrical symmetry of the plate and the loading, a one quarter plate model was utilized as a means to increase the number of nodes per unit area of the plate. A total of nine jets were used in the one quarter model. Only five jet centers lie directly on the quarter plate model. The remaining four lie outside the quarter plate boundary.

The edges of the faceplate were modeled as simply supported; displacements normal to the faceplate were restricted at the edges while displacements in the plane of the plate were unrestricted. Rotational boundary conditions could not be applied as the solid elements only supported 3 degrees of translational freedom.

Thermal boundary conditions were used to simulate the heat source and convective cooling. On the rear surface of the faceplate, within the region bounded by the centers of the outer jets, the heat transfer coefficient, h , was modeled as a constant 200,000 W/m²·K. The liquid temperature used was a constant 310 K. Outside this region, the decrease in h was modeled using a Gaussian

distribution, similar to the pressure load approach. On the forward surface of the faceplate, the heat flux was modeled as a constant over the active heater surface (see shaded region in Figure 17). All other surfaces on the faceplate were adiabatic. Thermal expansion was based on a reference temperature of 20 °C. Temperature dependent properties of thermal conductivity, coefficient of thermal expansion and Young's modulus were utilized. A full listing of the finite element algorithm is included in Appendix D.

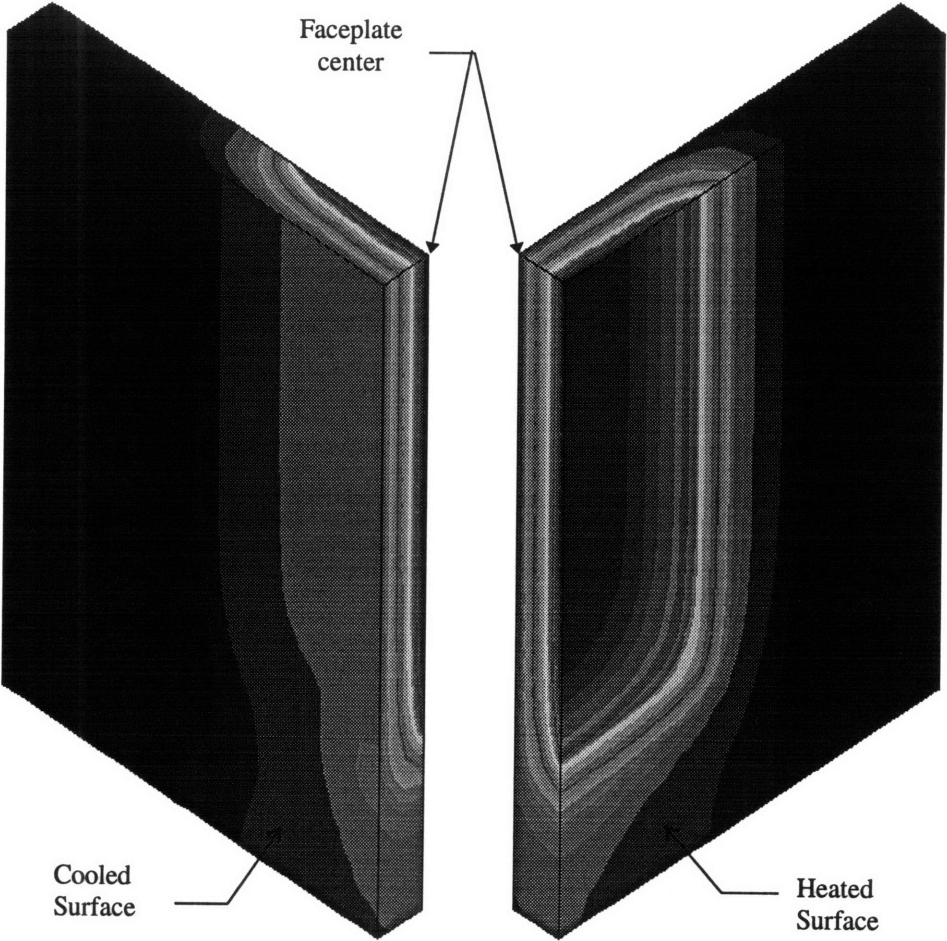


Figure 20 Finite element thermal analysis results for a one quarter, 3 mm TZM faceplate model with a heat flux of 10 MW/m².

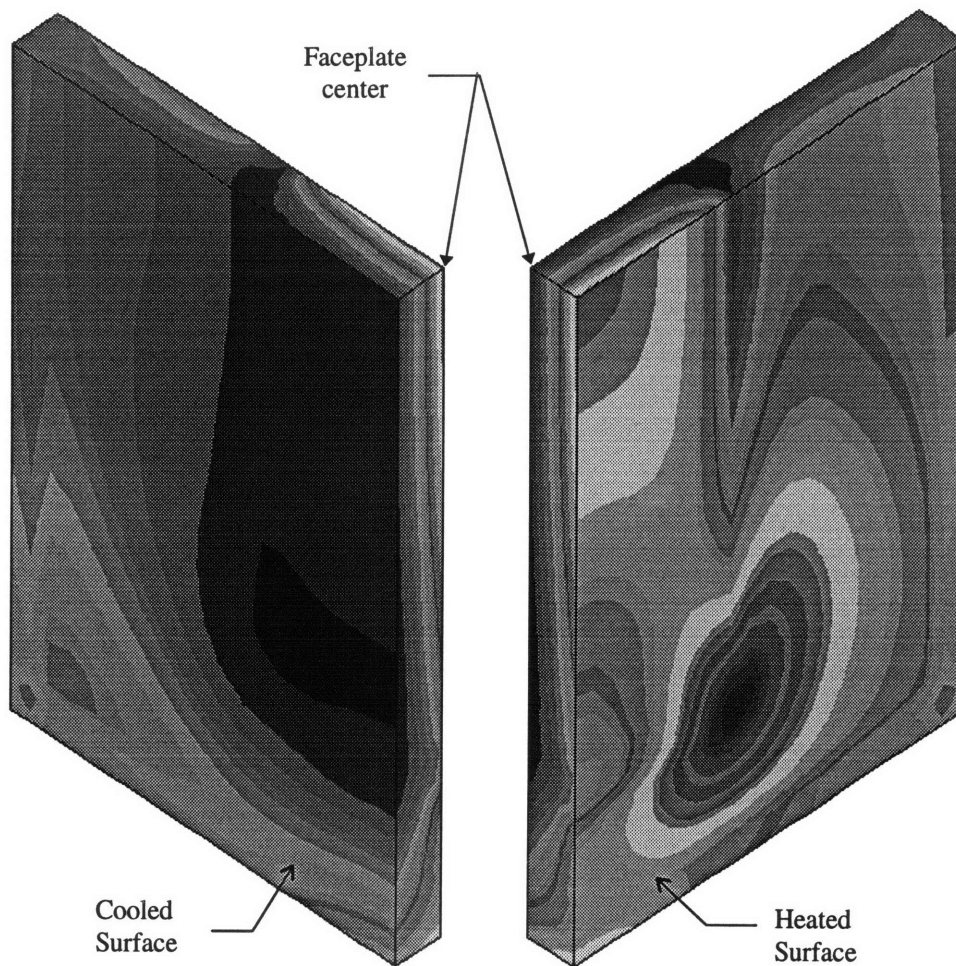


Figure 21 Finite element stress analysis results for a one quarter, 3 mm TZM faceplate model with a heat flux of 10 MW/m^2 .

Multidimensional heat conduction effects are observed across the entire heater as shown in Figure 20. The dominant temperature gradients occur through the plate thickness, a result of the large heat transfer coefficient provided by the liquid jet array. There exist, nonetheless, substantial temperature gradients in the plane of the heated surface. The von Mises stress distribution is shown in Figure 21. Clearly, the highest stresses occur on the heated surface and exist in two distinct zones. The first zone occurs at the center of the faceplate and the second zone occurs beyond the corner of the heater. The rectangular geometry of the heater is believed to induce the secondary zone of stress.

The temperature and heat flux distributions for a 3 mm thick TZM faceplate with a heat flux of 10 MW/m^2 are shown in Figure 22 and Figure 23, respectively. The heat flow is essentially one dimensional near the center of the heating element, but shows some significant 3-D effects near the outside edges. From this we can conclude that the central jets in the array are removing essentially the full imposed heat flux, while the outermost jets experience a flux that is approximately 50 % lower.

The temperature of the faceplate depends on the applied heat load, the convective cooling, the faceplate material and thickness. The faceplate temperatures increased with increasing thickness and heat flux. Due to their superior thermal conductivity, DS copper ($k \sim 350 \text{ W/m}\cdot\text{K}$) faceplates remained cooler than TZM ($k \sim 115 \text{ W/m}\cdot\text{K}$) faceplates. At a heat flux of 2.5 MW/m^2 , a 2.5 mm DS copper faceplate exhibited temperatures up to 33 % cooler than the equivalent TZM faceplate. At a heat flux of 40 MW/m^2 , a 4.0 mm DS copper faceplate exhibited temperatures up to 61 % cooler than the equivalent TZM faceplate. Figure 24 illustrates the maximum faceplate temperature, occurring on the rear surface at the plate center, as a function of the heat flux.

Two distinct zones of high stress occurred on the faceplate. One was at the corner of the heater while the other was at the center of the faceplate, both on the forward faceplate surface. These stresses are shown as a function of the heat flux and faceplate thickness in Figure 25 - Figure 30; both for DS copper (C15715) and molybdenum (TZM). For each material, the heat flux was varied from 2.5 MW/m^2 to 40 MW/m^2 for a plate thickness of 2.5, 3.0 and 4.0 mm.

For DS copper, yielding occurred at the corner of the heater at a heat flux of 19 and 18 MW/m^2 for 2.5 and 3.0 mm thick faceplates, respectively. At 4.0 mm, both the center and the corner yielded at a heat flux of 17 MW/m^2 . For molybdenum, yielding occurred at the center and the corner of the faceplate at a heat flux of 24 and 21 MW/m^2 for 2.5 and 3.0 mm thick faceplates. At 4.0 mm, the center yielded at a heat flux of 17 MW/m^2 . Results have been listed in Table 6 - Table 11. Stresses at the center and the corner which have exceeded their corresponding yield stress are italicized.

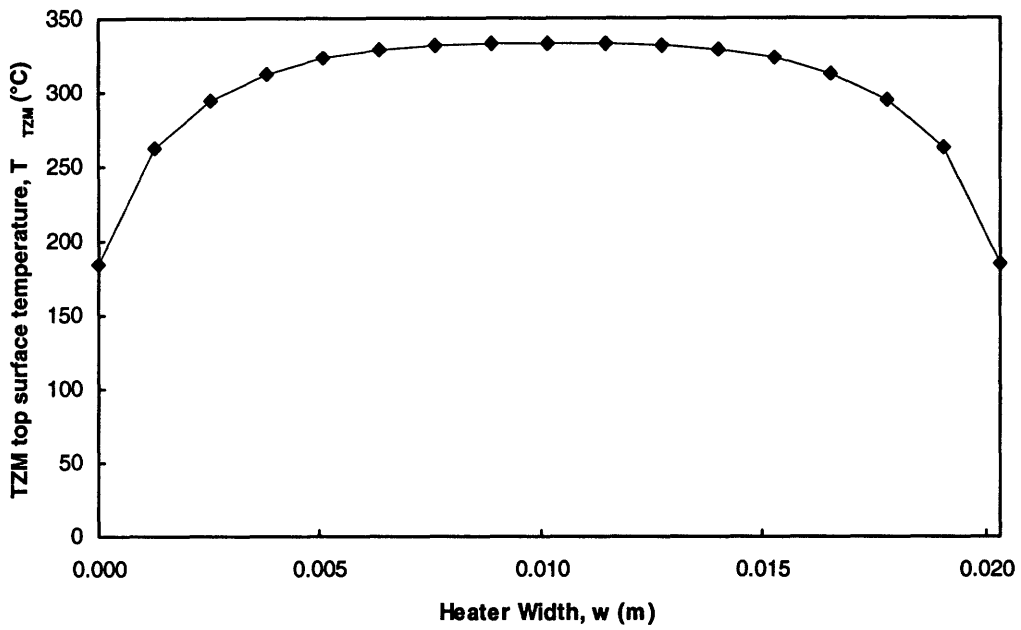


Figure 22 TZM faceplate top surface temperature variation across the heater width.

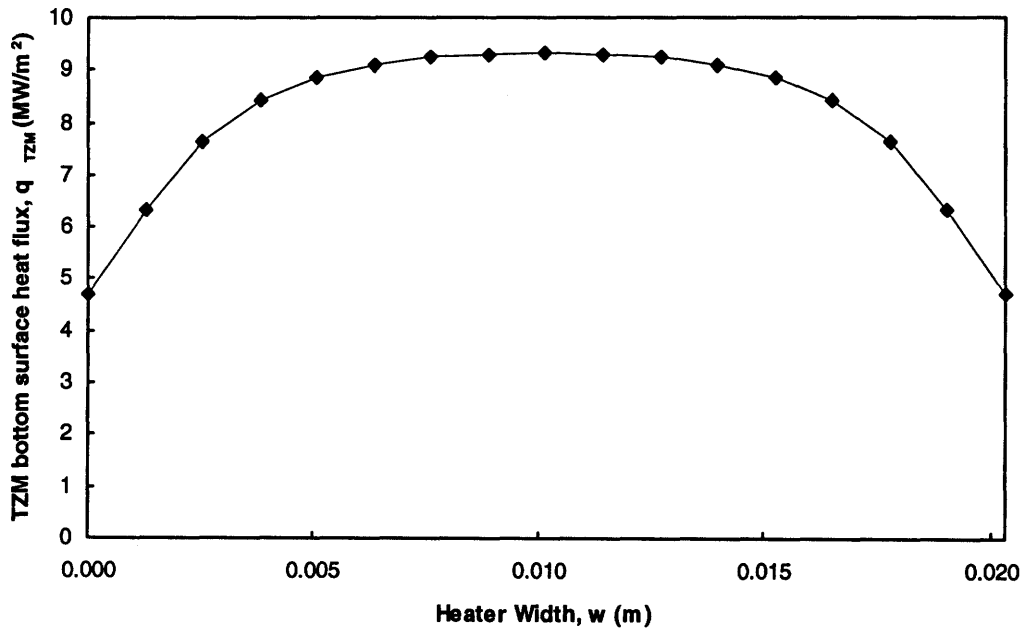


Figure 23 TZM faceplate bottom surface heat flux variation across the heater width.

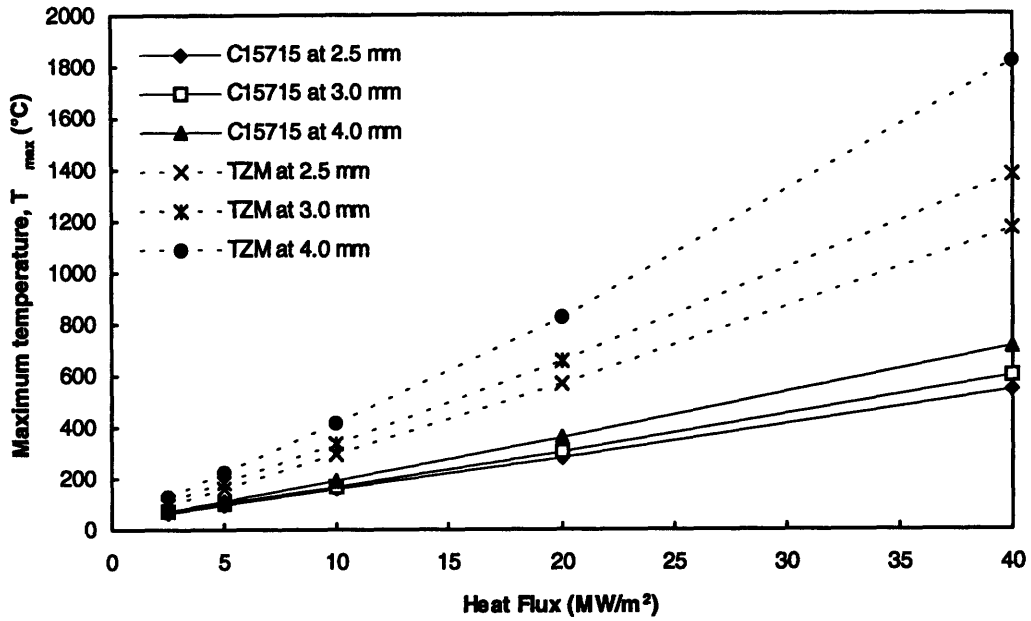


Figure 24 Maximum faceplate temperature as a function of the heat flux.

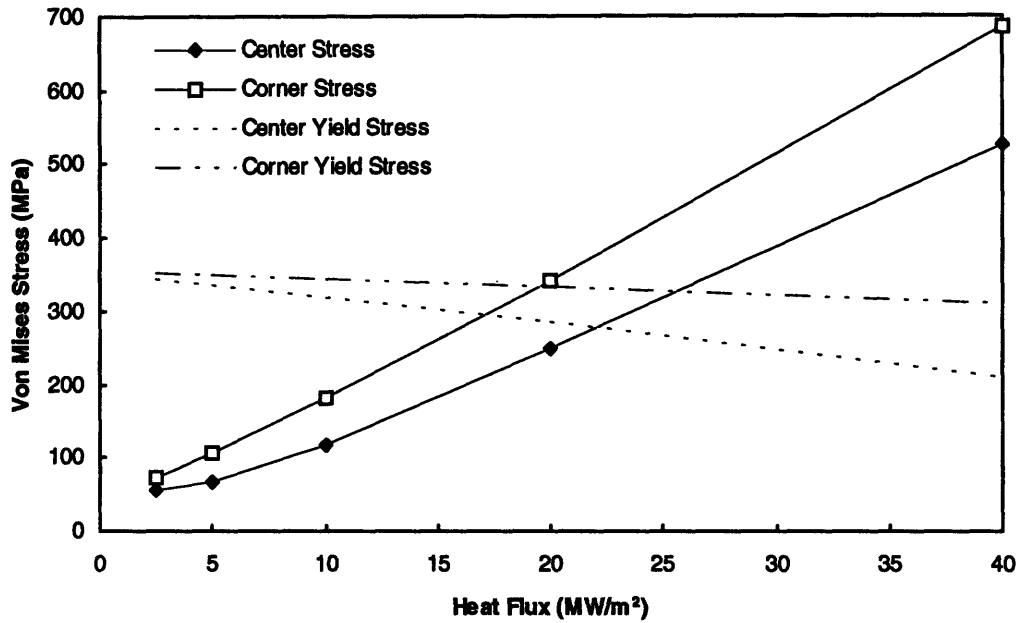


Figure 25 Stress vs. heat flux for a 2.5 mm C15715 faceplate.

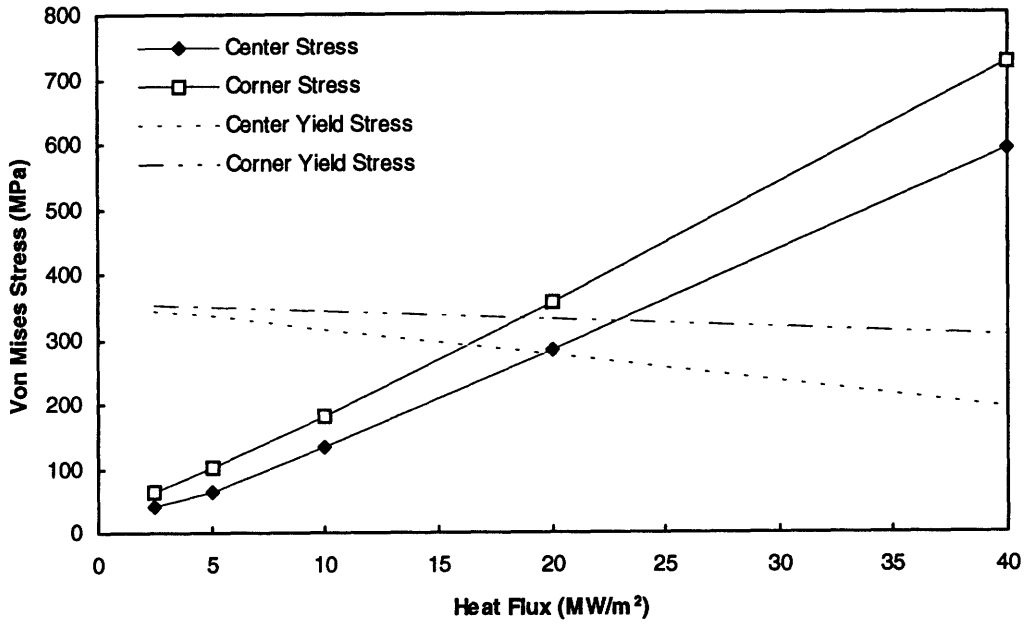


Figure 26 Stress vs. heat flux for a 3.0 mm C15715 faceplate.

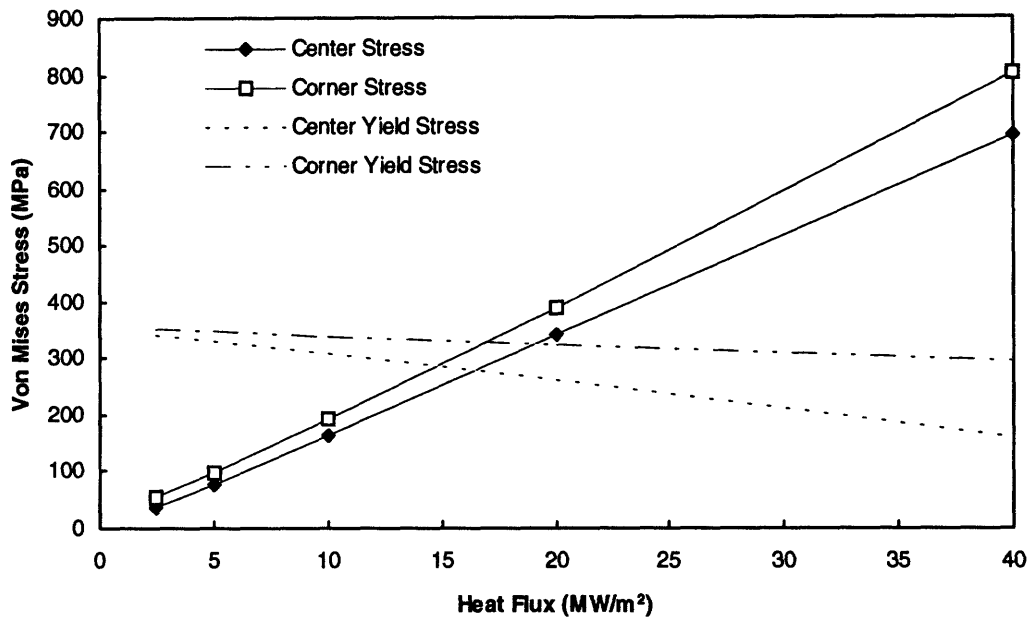


Figure 27 Stress vs. heat flux for a 4.0 mm C15715 faceplate.

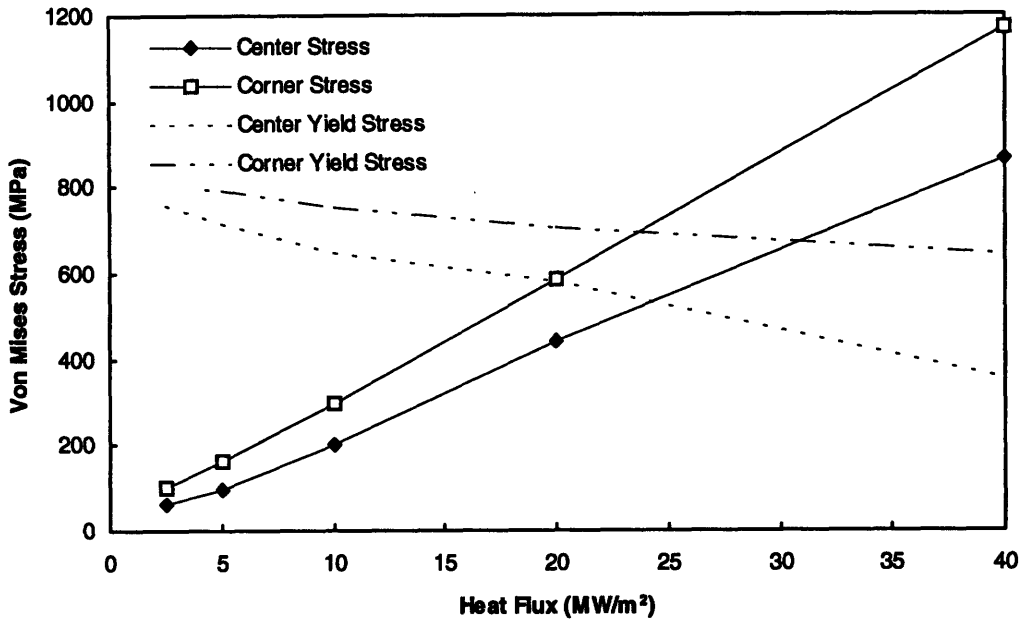


Figure 28 Stress vs. heat flux for a 2.5 mm TZM faceplate.

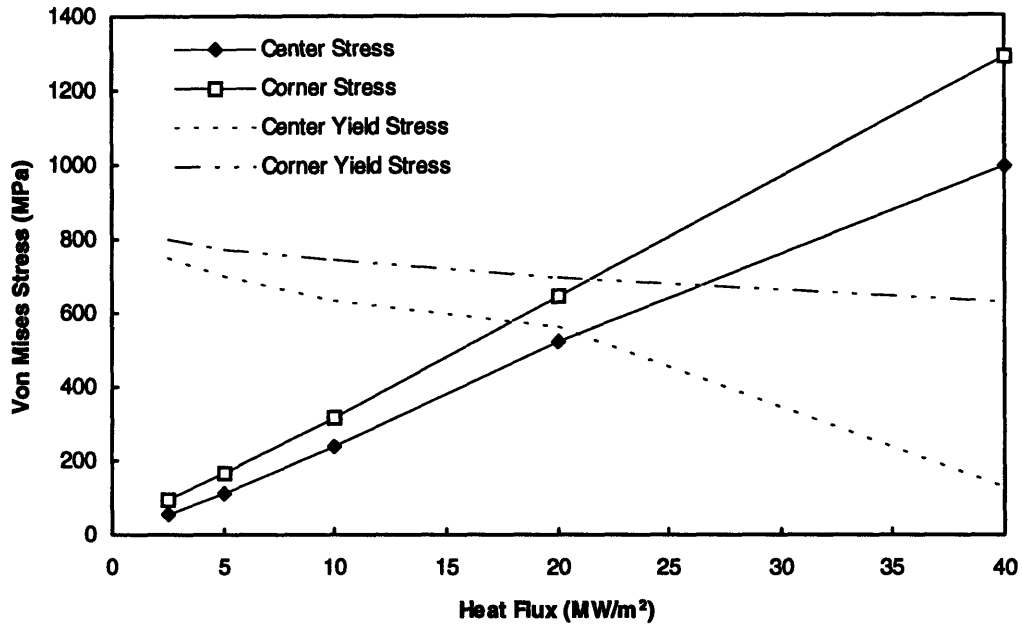


Figure 29 Stress vs. heat flux for a 3.0 mm TZM faceplate.

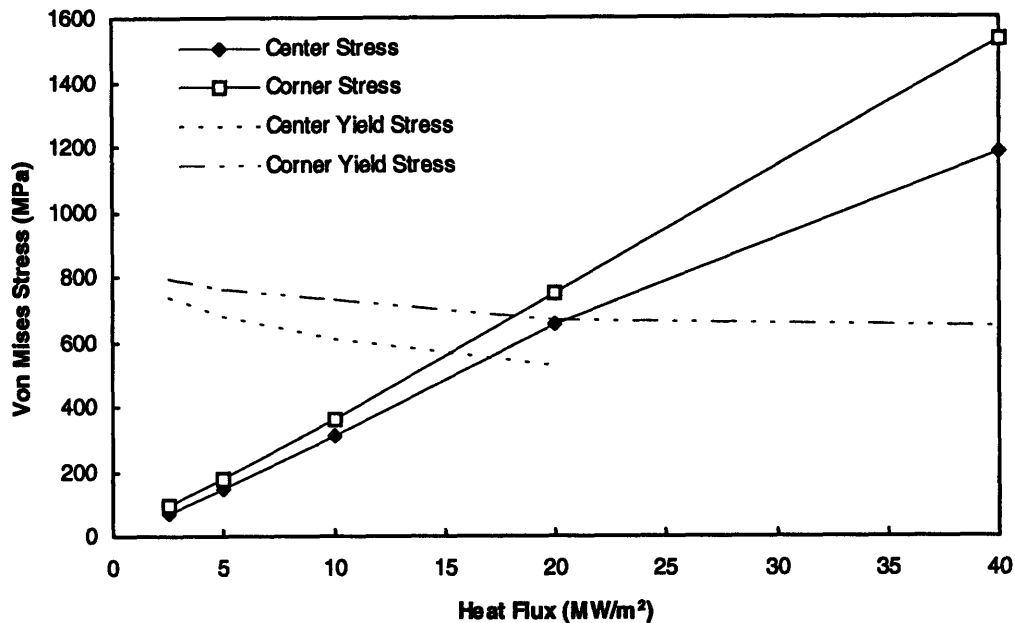


Figure 30 Stress vs. heat flux for a 4.0 mm TZM faceplate.

4.2.1 Summary of Finite Element Simulations

The maximum stress for all cases occurred at the corner region. For a thickness less than 4.0 mm, the DS copper faceplate was more likely to fail at the corner. For a thickness greater than 2.5 mm, the TZM faceplate was more likely to fail at the center. In general, the failure occurred when the local stress exceeded the local yield strength. As shown, the center of the faceplate, where the maximum temperature and minimum yield strength occur, was at times the point of failure. In both cases, the 2.5 mm faceplate showed the greatest sustainable heat flux prior to failure. Overall, the 2.5 mm molybdenum faceplate showed the greatest achievable heat flux prior to failure. In all cases, the stresses were proportional to the heat flux.

Near the outside corners of the heating element, expansion of the heated region led to stress concentrations in the unheated corner of the faceplate. A third zone of high stress occurred along the extreme edges of the faceplate. Here, stresses were up to 50 % greater than those on the interior but are believed to be an artifact of the numerical boundary condition.

Table 6 Stresses and temperatures as a function of heat flux. DS Copper (C15715), 2.5 mm thick faceplate FEM results. *Italicized stresses exceed the local yield stress.*

Heat Flux (MW/m ²)	Maximum Temperature (°C)	Center Stress (MPa)	Corner Stress (MPa)	Center Yield Stress (MPa)	Corner Yield Stress (MPa)
2.5	66.52	57.17	72.56	345.29	352.19
5.0	96.40	67.28	107.69	336.78	350.62
10.0	156.82	118.05	182.10	319.55	343.30
20.0	280.46	250.34	<i>342.37</i>	284.32	332.81
40.0	540.50	<i>527.08</i>	<i>685.14</i>	210.19	311.62

Table 7 Stresses and temperatures as a function of heat flux. DS Copper (C15715), 3.0 mm thick faceplate FEM results. *Italicized stresses exceed the local yield stress.*

Heat Flux (MW/m ²)	Maximum Temperature (°C)	Center Stress (MPa)	Corner Stress (MPa)	Center Yield Stress (MPa)	Corner Yield Stress (MPa)
2.5	69.70	42.32	63.03	344.39	351.84
5.0	102.82	64.92	101.23	334.95	349.94
10.0	169.90	132.26	182.42	315.83	341.81
20.0	307.68	<i>284.11</i>	<i>355.28</i>	276.56	329.80
40.0	600.07	<i>588.95</i>	<i>724.10</i>	193.23	305.46

Table 8 Stresses and temperatures as a function of heat flux. DS Copper (C15715), 4.0 mm thick faceplate FEM results. *Italicized stresses exceed the local yield stress.*

Heat Flux (MW/m ²)	Maximum Temperature (°C)	Center Stress (MPa)	Corner Stress (MPa)	Center Yield Stress (MPa)	Corner Yield Stress (MPa)
2.5	75.72	36.60	55.74	342.67	351.12
5.0	114.98	75.85	99.53	331.48	348.50
10.0	194.76	161.64	191.81	308.74	338.77
20.0	359.77	<i>342.78</i>	<i>387.75</i>	261.72	323.62
40.0	715.99	<i>692.47</i>	<i>802.79</i>	160.19	292.76

Table 9 Stresses and temperatures as a function of heat flux. TZM, 2.5 mm thick faceplate FEM results. *Italicized stresses exceed the local yield stress.*

Heat Flux (MW/m ²)	Maximum Temperature (°C)	Center Stress (MPa)	Corner Stress (MPa)	Center Yield Stress (MPa)	Corner Yield Stress (MPa)
2.5	99.54	61.84	99.51	756.35	800.13
5.0	163.10	97.26	162.14	713.78	793.45
10.0	292.98	200.93	295.92	649.63	752.76
20.0	565.07	440.76	587.93	578.86	707.91
40.0	1168.42	865.86	<i>1172.42</i>	356.11	642.02

Table 10 Stresses and temperatures as a function of heat flux. TZM, 3.0 mm thick faceplate FEM results. *Italicized stresses exceed the local yield stress.*

Heat Flux (MW/m ²)	Maximum Temperature (°C)	Center Stress (MPa)	Corner Stress (MPa)	Center Yield Stress (MPa)	Corner Yield Stress (MPa)
2.5	109.31	57.20	94.79	749.26	798.03
5.0	182.95	111.95	165.35	702.12	773.94
10.0	334.01	240.58	316.48	634.59	744.25
20.0	653.17	522.50	646.63	563.48	694.18
40.0	1377.77	995.28	<i>1290.53</i>	127.97	625.04

Table 11 Stresses and temperatures as a function of heat flux. TZM, 4.0 mm thick faceplate FEM results. *Italicized stresses exceed the local yield stress.*

Heat Flux (MW/m ²)	Maximum Temperature (°C)	Center Stress (MPa)	Corner Stress (MPa)	Center Yield Stress (MPa)	Corner Yield Stress (MPa)
2.5	128.08	68.92	95.79	736.21	793.41
5.0	221.21	146.68	180.74	681.61	764.35
10.0	413.71	314.14	361.69	610.82	727.40
20.0	827.33	<i>652.62</i>	<i>752.00</i>	526.76	668.60
40.0	1814.49	<i>1179.73</i>	<i>1532.32</i>	-	648.75

5. Transient and Steady State Thermal Models

5.1 Faceplate Transient Thermal Analysis

At the center of the plate, heat conduction is mainly one dimensional. The following one dimensional transient solution is valid at the center of the plate where the temperature gradient through the thickness is much larger than gradients along the plate. The plate is modeled as a horizontally infinite slab of thickness a . the transient temperature solution is given by

$$T(x,t) = \frac{2 \sum_{n=1}^{\infty} \left\{ \frac{q}{k} [\cos(\alpha_n a) + (\alpha_n a) \sin(\alpha_n a) - 1] - q \left(\frac{a}{k} + \frac{1}{h} \right) [\alpha_n \sin(\alpha_n a)] \right\}}{\alpha_n [(\alpha_n a) + \sin(\alpha_n a) \cos(\alpha_n a)]} e^{-\alpha_n^2 a^2 t} \cos(\alpha_n x) \quad (5.1)$$

$$-\frac{q}{k} x + q \left(\frac{a}{k} + \frac{1}{h} \right) + T_{\infty}$$

for $0 < x < a$ where $\tan(\alpha_n a) = \text{Bi}/\alpha_n a$ and $\text{Bi} = h a / k$.

The heat flux q is suddenly imposed at the surface $x = 0$. Results were developed for a 2 mm thick C15715 faceplate, using average material properties, with an imposed heat flux of 20 MW/m², a heat transfer coefficient, h , taken to be 200,000 W/m²·K and T_{∞} as 310 K. The time it takes to reach steady state is approximately 0.27 seconds. Although the temperature transients die out quickly, they may induce large thermal stresses. Even a free beam exhibits thermal stress due to nonlinear transient temperature profiles. However, transient stresses are smaller than steady state stresses for fixed beams with a constant flux boundary condition.⁵ During experimentation, the power level was increased gradually to avoid significant transient effects.

5.2 Analytical Heater Design

5.2.1 Pyrolytic Graphite Heaters

In designing the heating element, the use of a pyrolytic graphite heating element was considered. Typically, pyrolytic graphite is an attractive option for applications requiring joule heating. It is a highly anisotropic material with a high thermal conductivity parallel to its material planes.

However, its thermal conductivity perpendicular to its planes is quite poor. In order to utilize the available power supply, a heater on the order of several millimeters thick would be required. The problems we encountered with this design are as follow. It was not possible to manufacture 10.3 cm² sheet of pyrolytic graphite having the high thermal conductivity through its thin dimension. Resistance heaters combining pyrolytic graphite with pyrolytic boron nitride coatings (used for electrical isolation and oxidation prevention) showed unfeasibly high electrical resistance. At high heat fluxes, the thermal contact resistance at the heater/faceplate boundary could potentially be minimized by applying a sufficiently large contact pressure and/or introducing an appropriate interstitial material to improve the thermal contact. However, contact pressures introduce additional unwanted faceplate stresses, and a sufficiently effective interstitial material could not be specified with confidence.

5.2.2 Thin Metal Film Heaters

This section provides a theoretical procedure to design a metallic thin-film heating element. The heater consists of an Al₂O₃ insulator film located between the faceplate and a molybdenum heater film. Molybdenum's high electrical resistivity (relative to other pure metals) and high melting temperature makes it an ideal material for thin-film designs. The heater is designed to provide a maximum heat flux of 30 MW/m² over a 10.3 cm² area. The power source rating is 3000 A at 24 VDC.

The heating element was designed to meet several heat transfer and fluid mechanics constraints important to the design of the nozzle plate while maximizing the heat flux and its corresponding area. The design is based on bulk material properties, which can vary significantly from thin film material properties, as our experience has dictated.

All heat is assumed to flow across the heater thickness direction and any losses to the environment are considered to be negligible. The total power generated in the heating element may then be expressed as the product of the heat flux, q , and the heater area, A_h . That is,

$$P = qA_h \quad (5.2)$$

Utilizing a total power supply of 72 kW DC, the heater can be theoretically expected to generate a maximum heat flux of 70 MW/m^2 for a heater area of 2.03 by 5.08 cm (10.3 cm^2). The design being considered herein is based on a maximum heat flux of 30 MW/m^2 . Higher fluxes require thinner heaters which approach the limits of plasma spraying. In addition, variations in thickness across the film surface have a greater impact on thinner films.

The thickness of the heater may be determined from limitations imposed by the candidate materials, the available power supply configuration and thin film technology. The performance of the heating element throughout its operating range will depend strongly upon the electrical resistivity and thermal conductivity of the chosen material. As heater temperatures will vary greatly, the temperature dependence of these material properties must be accounted for in a thermoelectric model.

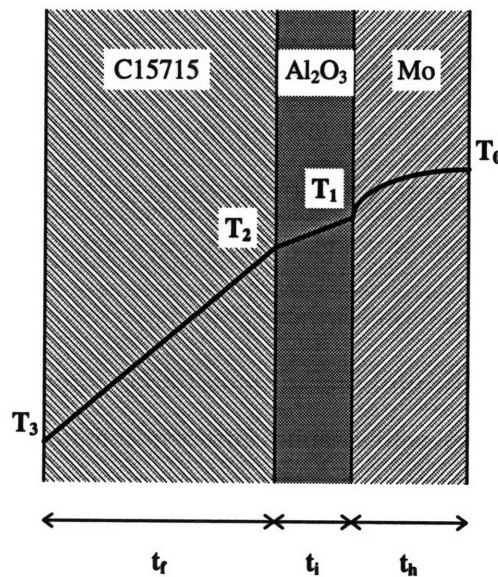


Figure 31 Composite series wall.

At a point sufficiently far from the heater boundary, the heat flow through the thickness of the faceplate, Al_2O_3 layer and the heater may be modeled by one dimensional, steady state heat transfer for a series composite wall as shown in Figure 31. The thermal contact resistance at each wall interface is assumed to be negligible. A temperature gradient across the composite wall is established as a result of joule heating in the heater, due to the electric current flow, and

convection heat transfer at the faceplate/liquid boundary. Utilizing the heat flux as a design input parameter, the temperature T_3 may be determined from Newton's law of cooling,

$$q = h(T_3 - T_\infty) \quad (5.3)$$

where h is the convection coefficient for an impinging liquid jet of temperature T_∞ .

At a heat flux of 30 MW/m^2 , the temperature across the faceplate varies significantly. The degree to which it varies depends strongly upon the thermal conductivity and its temperature dependency. To accurately determine the temperature T_2 at the faceplate/ Al_2O_3 boundary, we must account for the thermal conductivity's temperature dependence. In its most general form, the heat diffusion equation may be written as

$$\rho c_p \frac{\partial T}{\partial t} = \frac{\partial}{\partial x} \left(k \frac{\partial T}{\partial x} \right) + \frac{\partial}{\partial y} \left(k \frac{\partial T}{\partial y} \right) + \frac{\partial}{\partial z} \left(k \frac{\partial T}{\partial z} \right) + \dot{q} \quad (5.4)$$

For one-dimensional, steady-state heat transfer with no energy generation, Equation (5.4) may be written as

$$\frac{d}{dx} \left(k_f \frac{dT}{dx} \right) = 0 \quad (5.5)$$

The first constant of integration of Equation (5.5) is identically Fourier's law,

$$-k_f \frac{dT}{dx} = q \quad (5.6)$$

while the second constant may be evaluated using the following boundary condition,

$$T(x_2) = T_2$$

When the thermal conductivity k_f for the faceplate can be linearly correlated by a function of the form

$$k_f = k_1 T + k_2 \quad (5.7)$$

Utilizing Equations (5.5), (5.6) and (5.7) and integrating across the faceplate thickness t_f , the temperature T_2 may be obtained from the following equation

$$T_2 = \frac{-k_2 + \left(k_2^2 + k_1^2 T_3^2 + 2k_1 k_2 T_3 + 2k_1 q t_f\right)^{1/2}}{k_1} \quad (5.8)$$

The temperature T_1 at the Al_2O_3 /heater boundary may be closely estimated by assuming a constant thermal conductivity, k_i .

Ceramics such as Al_2O_3 are extremely poor thermal conductors but are excellent electrical insulators. The purpose of the Al_2O_3 is to electrically isolate the faceplate from the heater. Hence the required thickness depends upon its dielectric strength E_{\max} , and the applied voltage V_{\max} . From the definition of a material's dielectric strength, the Al_2O_3 thickness t_i , may be determined from,

$$t_i = \frac{V_{\max}}{E_{\max}} \quad (5.9)$$

The maximum voltage drop, V_{\max} , between the heater and the faceplate is 24 VDC. The dielectric strength, E_{\max} , of Al_2O_3 is 1×10^7 V/m. Using Equation (5.9), the thickness of Al_2O_3 required to electrically insulate the heater from the faceplate is 2.4 μm . However, due to limitations in the plasma spray technology, an Al_2O_3 thickness of 203 μm was used. Coats thinner than 203 μm did not provide adequate electrical insulation. The insulator thermal conductivity, k_i , at the temperature T_2 was utilized. The temperature T_1 may then be determined from Equation (5.6) as follows,

$$T_1 = T_2 + \frac{q t_i}{k_i} \quad (5.10)$$

Similarly, the heater is sufficiently thin that the temperature rise across its thickness t_h is small. Estimates show the temperature rise across the heater to be less than 5 K at 30 MW/m^2 . Hence, variations in the thermal conductivity k_h , and electrical resistivity ρ_e , may be neglected and these properties need only be evaluated at T_1 . For one-dimensional, steady-state heat transfer with heat generation and temperature independent properties, Equation (5.4) may be written as

$$\frac{d^2 T}{dx^2} + \frac{\dot{q}}{k_h} = 0 \quad (5.11)$$

and solved subject to the following boundary conditions,

$$\left. \frac{dT}{dx} \right|_{x=x_0} = 0 \text{ and } T(x_0) = T_0$$

First, in order to evaluate the heat generation quantity in Equation (5.11), we must determined the effects of voltage, current, electrical resistance and geometry upon the heater design. The DC generators are capable of producing either 12 VDC at 6000 A or 24 VDC at 3000 A. The heater resistance may be expressed by the following equation

$$R = \frac{\rho_e l}{wt_h} \quad (5.12)$$

where l is the heater length and its direction is parallel to the current flow, and w is the width of the heater. Alternately, the resistance R may be expressed using Ohm's law as follows,

$$R = \frac{V}{I} \quad (5.13)$$

From the perspective of thin-film technology, it is advantageous to minimize the thickness of the heater in order to minimize the stresses inherent in material deposition techniques such as plasma spraying. From a thermal and mechanical standpoint, thinner films mean lower temperatures and a decreased risk of high temperature thermal stress failure at a bimaterial interface. Therefore, from Equation (5.12), in order to minimize the heater thickness we must minimize l/w , maximize R and choose a material with a low electrical resistivity and sufficiently high melting temperature. These constraints are achieved by operating the generators at 24 VDC and 3000 A while requiring current to flow across the 2.03 cm distance. Combining Equations (5.12) and (5.13), the heater thickness may be expressed as

$$t_h = \left(\frac{\rho_h l}{w} \right) \left(\frac{i}{V} \right) \quad (5.14)$$

The internal heat generation may now be expressed as a function of the heat flux from the following equation

$$\dot{q} = \frac{q}{t_h} \quad (5.15)$$

Substituting Equation (5.15) into Equation (5.11), we may determine the heater surface temperature T_0 from the following equation

$$T_0 = T_1 + \frac{qt_h}{2k_h} \quad (5.16)$$

During operation, it will be necessary to determine the DC power supply voltage required to generate a particular heat flux. The total energy generated in the heating element is entirely due to electrical resistance and is described by the following equation,

$$P = i^2 R \quad (5.17)$$

Combining Equation (5.2) and (5.17), the current flow in the heating element may be expressed as

$$i = \left(\frac{qA_h}{R} \right)^{1/2} \quad (5.18)$$

while the voltage required to generate a particular heat flux may be expressed by Equation (5.13).

All temperatures in the faceplate assembly, the heater's thickness, current and voltage have been determined for the design flux. These parameters may be further evaluated at lower fluxes utilizing the same procedure, with the exception that the heater thickness remains constant at all lower fluxes. Results for a 3.0 mm C15715 faceplate, Al_2O_3 insulator and molybdenum heater are presented. The design yielded a 30.5 μm (1.2 mil) heater thickness. The Figure 32 illustrates the temperature as a function of the heat flux at various points throughout the faceplate, electrical insulator and heater. Note, as a result of thin film technology, the largest temperature rise should theoretically occur across the faceplate. In addition, Figure 33 is included to illustrate the voltage required to generate a particular heat flux.

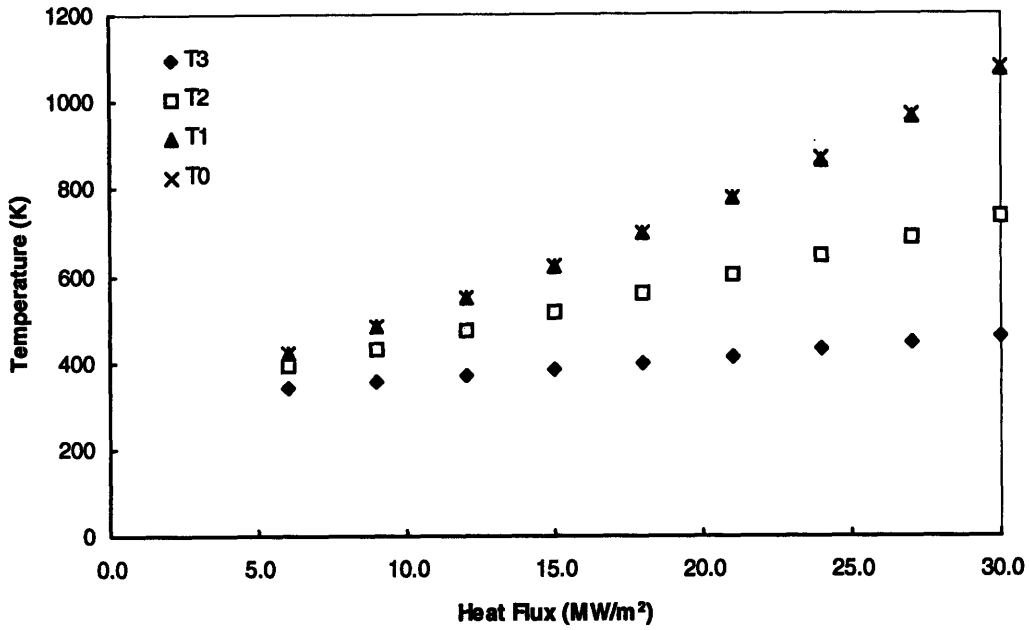


Figure 32 Temperature distribution throughout the faceplate assembly for a 3 mm C15715 faceplate, an 8 mil Al₂O₃ insulator, and a 1.2 mil molybdenum heater.

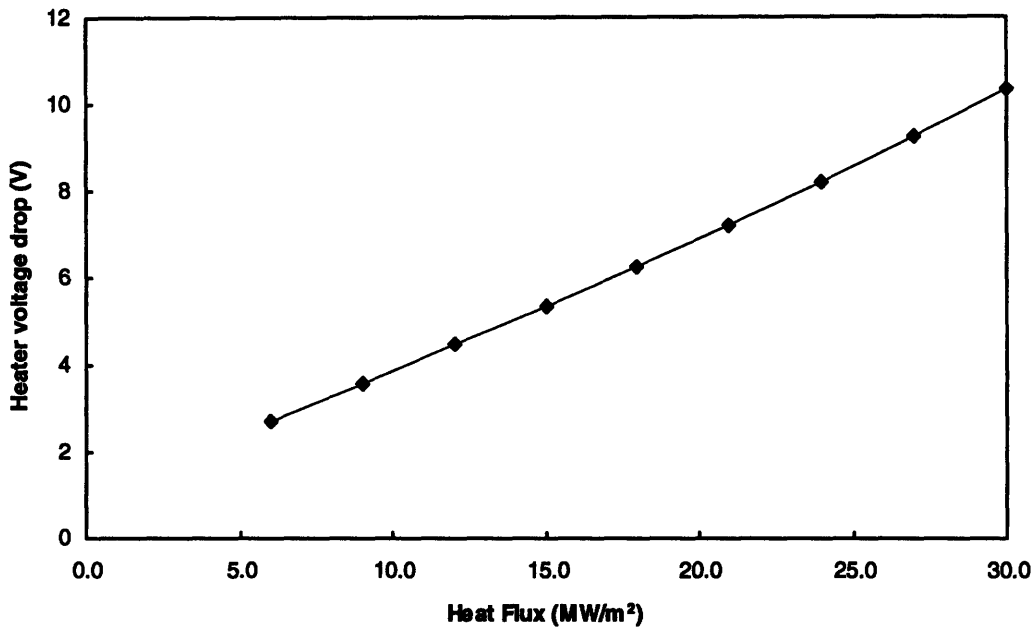


Figure 33 The required heater voltage as a function of the desired heat flux for a 3 mm C15715 faceplate, an 8 mil Al₂O₃ insulator, and a 1.2 mil molybdenum heater.

6. Experimental Development of Thin Film Heaters

We are aware of only one previous attempt to use thin-film resistance heaters to generate heat fluxes above 10 MW/m^2 over areas of several square centimeters.⁴⁰ This section describes the various designs attempted, the electrical resistances obtained, and the thermal resistances obtained. It is now possible to prescribe design characteristics for these heaters. Failure consistently occurs when the surface temperature exceeds $600 \text{ }^\circ\text{C}$.

6.1 Heater Development

Several heater prototypes have been developed, revealing numerous electrical design problems. The first few heaters consisted of a nickel film of $50 \text{ }\mu\text{m}$ (2 mils) thickness deposited atop a magnesium oxide film of $25 - 50 \text{ }\mu\text{m}$ (1 - 2 mils) thickness. This combination failed to provide electrical insulation between the nickel film and the faceplate. It was determined that designs based on known material properties were inadequate. Application of the films via plasma spraying alters their material properties, introducing substantial voids throughout. In addition, if the films are excessively thin the process tends to introduce a degree of unevenness on the order of several microns. In order to provide adequate electrical insulation between the plate and the heater film, a thicker layer of magnesium oxide was required.

The next few heaters were manufactured with thicker layers of magnesium oxide $200 - 250 \text{ }\mu\text{m}$ (8 - 10 mils) thick. These thicknesses provided adequate electrical isolation, but only allowed the films to conduct a maximum of 250 amps before they fractured and an electric arc occurred. It was observed that the electrical resistance measured across the electrodes was 2 orders of magnitude higher than the resistance calculated using tabulated bulk material properties. The high resistance was initially attributed to electrical contact resistance between the heater and the electrodes. This perception was strengthened by the fact that the heater surfaces were rough and probably provided poor contact with the electrodes.

⁴⁰ A.E. Hechanova, 1995, "Thermal Hydraulics of High Heat Flux Components," Ph.D. Thesis, Department of Nuclear Engineering, Massachusetts Institute of Technology, Cambridge, MA.

In an attempt to alleviate this problem, the copper bus bars were plated with silver and a 250 μm (10 mil) nickel film was deposited at the edges of the heater to provide a contact zone for the bus bars (Data Set A). This step showed no significant improvement. In several other runs, the heaters were sanded, aluminum foil was used at the contacts and the electrodes polished to an accuracy of 50 μm (1 mil) in an attempt to improve the contact. Thicker films of nickel between 175 and 300 μm (7 and 12 mils) were also sprayed in the hope that film resistance would be reduced. Data Set B corresponds to a 250 μm (10 mil) thick nickel heater that was sanded down to 150 μm (6 mils) and the electrodes polished. This step resulted in minor improvements. Film resistance was cut by half and currents in the film reached 460 amps at the highest heat flux of 3.5 MW/m^2 . (We ran a similar setup earlier, but with aluminum foil used at the electrodes, which yielded film currents of 415 amps and a maximum heat flux of 5 MW/m^2 . The temperature data was lost due to burning of the Kapton tape, resulting in a loss of contact between the thermocouples and the heater surface. High temperature thermocouple cement was used in all later runs).

In addition to these problems, the temperature distributions on the surface of these heaters varied widely, in some cases over 200 $^{\circ}\text{C}$ along the heater surface. This was also initially attributed to the non-uniform contact between the electrodes and heater causing a high electrical contact resistance. The effect of a high electrical contact resistance is to localize the flow of current into the film causing hot spots, which is consistent with what we observed. Table 13 summarizes the temperature scatter data for the various heater configurations run to date.

As the heater design evolved, the ceramic layer was changed to aluminum oxide because of its better adhesion characteristics in plasma spraying and in one attempt, the heater material was changed to molybdenum (Data Set C) in an effort to bring the heater resistance down by exploiting molybdenum's lower electrical resistivity. In addition, silver paint was used at the contacts to fill in any grooves resulting from film roughness.

These changes gave no improvement whatsoever. This was very surprising since the electrode imprints on the heater showed a uniform distribution of the highly conductive silver paint used. If the problem was indeed contact resistance, the silver paint should have entirely resolved it seeing how capillary action would fill in any grooves. Measured film resistances were still 2

orders of magnitude higher than calculated, currents through the film did not exceed the previous figure of 460 amps and film temperatures were still uneven, ranging from 401 to 598 °C along the molybdenum heater at the highest heat flux of 7 MW/m². This indicated that the primary source of the problem is with the film design rather than with the contact. Table 12 summarizes these problems for the first few heaters supplied by Vendor 1.

Table 12 Early problems encountered with thin film heaters. All heaters listed were supplied by Vendor 1.

Heater No.	Heater Film	Insulating Film	Comments
1	Ni, 2 mils	MgO, 1 mil	Inadequate electrical isolation between MgO and faceplate.
2	Ni, 2 mils	MgO, 2 mils	Inadequate electrical isolation between Ni and faceplate.
3	Ni, 2 mils	MgO, 8-10 mils	Electrical isolation achieved. Electrical resistance was too high. The heater failed at 250 amps. The high electrical resistance was initially attributed to contact resistance at the electrodes.
4	Ni, 2 mils	MgO, 10 mils	Copper bus bars were plated with silver. Thickened strips of Ni were deposited at the edges of the heater. No improvement was observed. See Data Set A.
5	Ni, 7-12 mils	Al ₂ O ₃ , 10 mils	Heaters were sanded and aluminum foil was used. No observable improvement for Data Set B. The heater was sanded and the electrodes polished. A slight improvement was observed. The film electrical resistance was reduced by 50% and the maximum current reached 460 amps.
6	Mo, 10 mils	Al ₂ O ₃ , 8 mils	The heater material was changed to molybdenum. Silver paint was used at the electrodes. See Data Set C. No improvement was observed. The maximum current remained at 460 amps.

In a final attempt to resolve these problems, it was decided to try a different vendor to plasma spray our heaters. The first heater supplied by Vendor 2 (Data Set D) consisted of 250 μm (10 mils) of molybdenum sprayed atop of 200 μm (8 mils) aluminum oxide atop a 3.2 mm TZM

plate (all the previous heaters supplied by Vendor 1 utilized dispersion strengthened copper plates). Identical test conditions were maintained. Silver paint was also used at the electrodes. These changes resulted in tremendous improvements. The film resistance dropped greatly, the highest current through the heater reached a maximum of 2347 amps at 7.3 kW before it failed; temperatures at the surface of the heater were much more uniform than previously recorded. The temperature scatter at the surface of the molybdenum at the highest heat flux of 7.1 MW/m^2 was only $70 \text{ }^\circ\text{C}$.

It was thus concluded that the technique of particular plasma spray vendors has an enormous effect on the quality of the films. In plasma spraying, high velocity particles impinge on the surface of the substance and form splats. Several factors govern the size and spreading of splats, which in turn affect the deposit microstructure and material properties. Velocity, particle size and temperature of particles strongly affect flattening and cooling of these splats.⁴¹ Differences in these parameters between the two vendors appear in the form of the film quality. Experimentation continued with heaters supplied by Vendor 2. Thinner heaters were subsequently tested in an attempt to reduce the heater's contribution to the total thermal resistance.

6.2 Surface Temperature Scatter

Vendor 1 consistently produced films with poor electrical characteristics which led to very large temperature variations over the surface of a given film, irrespective of film thickness. Vendor 2 produced films having a much finer grain structure and consequently much more uniform temperatures. Vendor 2's films performed very uniformly for thick films (Figure 34, Data Set D), but large scale surface temperature variations were also observed when thinner films were tested. This is especially clear when comparing the temperature scatter of a $75 \text{ }\mu\text{m}$ (3 mil) thick molybdenum film to that of a $250 \text{ }\mu\text{m}$ (10 mil) thick molybdenum film (Data Sets D and E, respectively).

⁴¹ S. Sampath and H. Herman, "Rapid Solidification and Microstructure Development During Plasma Spray Deposition," *Journal of Thermal Spray Technology*. Vol. 5. December 1996, pp. 445-456.

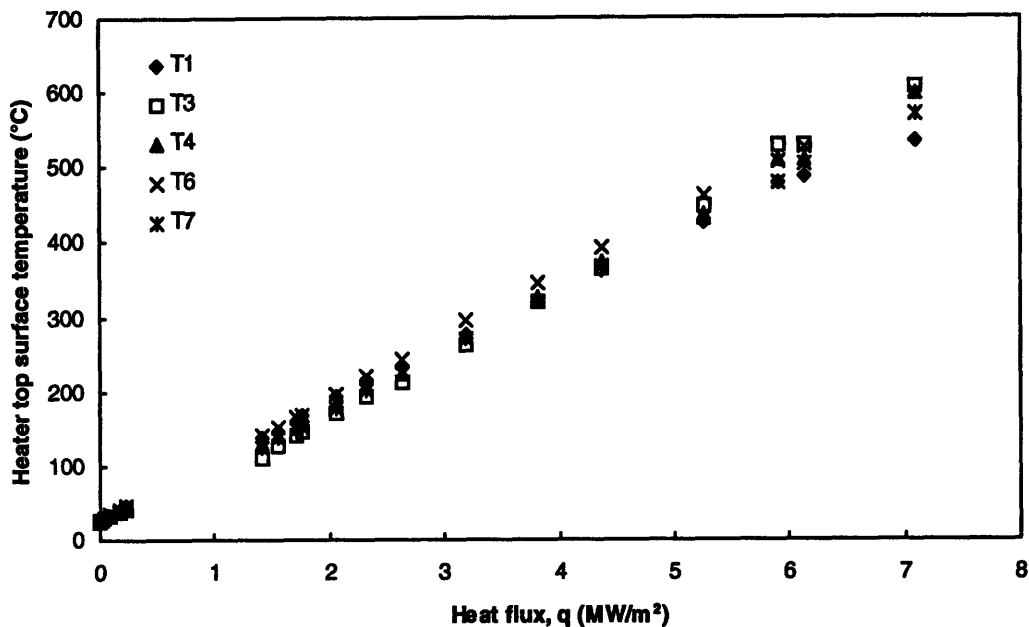


Figure 34 Heater top surface temperatures for various thermocouples as a function of the heat flux for Data Set D.

The plasma spraying process produces non-uniform films whose thickness can vary by as much as 50 μm (2 mils). Vendor 2 provided films with superior uniformity; the thickness varied by approximately 25 μm (1 mils). This variation results from micrometer scale variations inherent to the plasma spraying process. When molten droplets tens of micrometers in diameter strike the surface, splats form; a collection of which constitutes the deposit. The typical thickness of a plasma spray splat varies from 1 to 10 μm .⁴² Consequently, film non-uniformities that focus the resistive heating into thicker portions of the film are emphasized for thinner films. Table 13 below summarizes this data for various runs. (This spatial scatter is also represented by the vertical error bars in Figure 37 through Figure 43.) This conclusion does not apparently hold when comparing Data Sets F and G with the thicker film exhibiting a greater or equal scatter, but it may be a consequence of the 25 - 50 μm (1 - 2 mils) uncertainty introduced.

Table 13 Surface temperature scatter (evaluated at $q \approx 3 \text{ MW/m}^2$) and electrical resistance data for various heater configurations. Measured R tabulated for $T_{s,av} \approx 300 \text{ }^\circ\text{C}$ along with its experimental uncertainty. Calculated R estimated at $300 \text{ }^\circ\text{C}$ using bulk material properties. The calculated resistance carries an uncertainty owing to a 1 - 2 mils thickness variation from the plasma spraying. Underlined data sets provided by Vendor 1, others provided by Vendor 2.

Data Set	Date	Heater Film	T_s , scatter ($^\circ\text{C}$)	R , measured ($\text{m}\Omega$)	R , calculated ($\text{m}\Omega$)
<u>A</u>	12/18/96	Ni, 2 mils	198.10	34.07 ± 0.88	1.70
<u>B</u>	2/5/97	Ni, 10 mils*	143.76	17.65 ± 0.25	0.62
<u>C</u>	3/4/97	Mo, 10 mils	114.20	34.25 ± 0.53	0.20
D	3/1/97	Mo, 10 mils	32.00	1.29 ± 0.03	0.19
E	3/19/97	Mo, 3 mils	137.76	5.28 ± 0.07	0.68
F	3/24/97	Mo, 5 mils	76.41	2.94 ± 0.05	0.41
G	4/2/97	Mo, 7 mils	79.44	1.98 ± 0.04	0.29

*Sanded down to 6 mils.

6.3 Electrical Resistance

Even though Vendor 2 produced a better quality film with a lower electrical resistance, measured resistance values were still around 5 to 7 times higher than those calculated using bulk properties ($R = \rho_e l / wt$). Film deposition processes generally introduce mechanical defects, voids and chemical impurities into the thin film. Thin film deposition processes also result in poor contact at the microscopic point of view.⁴³ Such non-uniformities alter the film's properties from bulk material values. The measured electrical resistance is compared to the theoretical values in Table 13, and plotted as a function of the surface average film temperature in Figure 35 for Data Set D. The measured resistance increases with temperature, which is consistent with the temperature dependence of molybdenum's resistivity. Furthermore, given the scatter of the resistance data, the rate of change of resistance with temperature is close to the slope based on the theoretical values.

⁴² S. Sampath and H. Herman, "Rapid Solidification and Microstructure Development During Plasma Spray Deposition," *Journal of Thermal Spray Technology*. Vol. 5. December 1996, pp. 445-456.

⁴³ T.Q. Qiu, Personal Communication, Cambridge, MA, March 3, 1997.

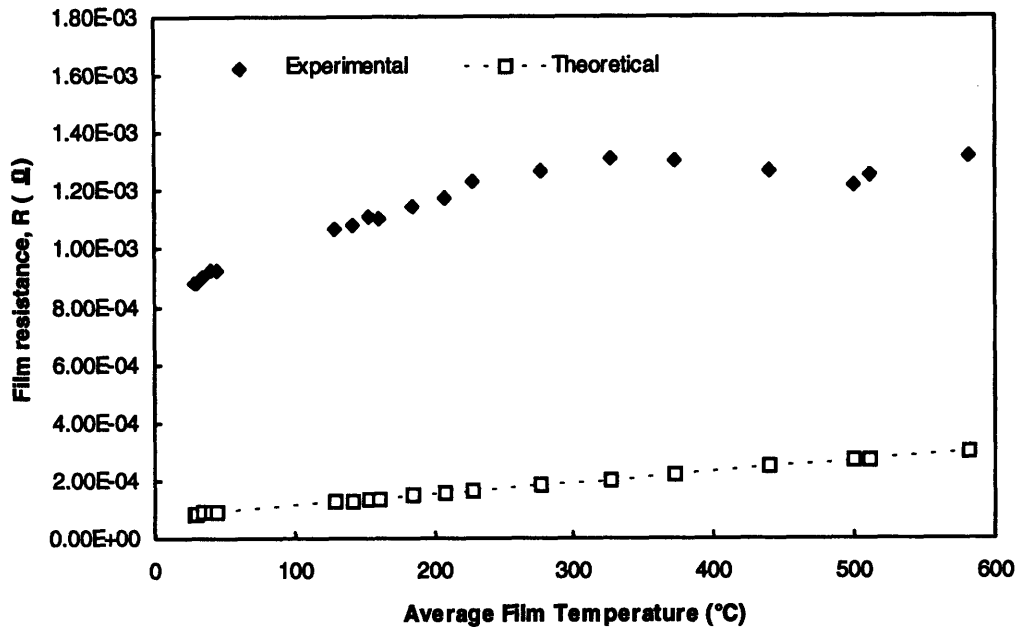


Figure 35 Experimental and theoretical heater film resistance as a function of the surface average film temperature for Data Set D.

6.4 Thermal Resistance

The plasma spraying process produces large variations in the material properties of films, owing to voids and impurities introduced during the process. This leads to a much higher electrical resistivity than that for the bulk material and a much lower thermal conductivity. The reduced thermal conductivity greatly increases the thermal resistance of the plasma sprayed layers. A thick film can put most of the thermal resistance and temperature rise into the thin films rather than the faceplate and boundary layer.

Film thermal resistances are quantified in Table 14. The total thermal resistance was determined from $R_{th,total} = \Delta T/q$. The average total temperature difference between the bulk liquid and the heater film's upper surface, ΔT , was divided by the surface averaged heat flux, q . The faceplate thermal resistance was determined from $R_{th,plate} = t_p/k_f$ where k_f is taken to be 350 W/m·K for C15715 and 115 W/m·K for molybdenum TZM. The boundary layer thermal resistance is

determined from $R_{th,bl} = 1/h$. The thermal resistance across the films, $R_{th,films}$, is determined by subtracting $R_{th,plate}$ and $R_{th,bl}$ from $R_{th,total}$.

Table 14 Thermal resistance values for various heater/plate configurations. All thermal resistance values calculated at $\Delta T \approx 300$ °C. Film thermal resistance values have been estimated using $h = 200,000$ W/m²·K. Underlined data sets provided by Vendor 1, others provided by Vendor 2.

Data Set	Heater Film	Insulating Film	Plate	$R_{th,total}$ (m ² ·K/MW)	$R_{th,plate}$ (m ² ·K/MW)	$R_{th,films}$ (m ² ·K/MW)
<u>A</u>	Ni, 2 mils	MgO, 10 mils	C15715, 3 mm	146.81 ± 23.52	8.57	133.24 ± 23.52
<u>B</u>	Ni, 10 mils*	Al ₂ O ₃ , 10 mils	C15715, 3 mm	76.01 ± 20.51	8.57	62.44 ± 20.51
<u>C</u>	Mo, 10 mils	Al ₂ O ₃ , 8 mils	C15715, 3 mm	58.90 ± 14.74	8.57	45.33 ± 14.74
D	Mo, 10 mils	Al ₂ O ₃ , 8 mils	TZM, 3.2 mm	76.53 ± 2.98	27.61	43.92 ± 2.98
E	Mo, 3 mils	Al ₂ O ₃ , 8 mils	TZM, 2.3 mm	77.54 ± 21.24	20.00	52.54 ± 21.24
F	Mo, 5 mils	Al ₂ O ₃ , 8 mils	TZM, 2.3 mm	79.90 ± 12.19	20.00	54.90 ± 12.19
G	Mo, 7 mils	Al ₂ O ₃ , 8 mils	TZM, 2.3 mm	78.00 ± 10.96	20.00	53.00 ± 10.96

*Sanded down to 6 mils.

Data Sets E through G present three experiments in which the only parameter varied was the thickness of the metallic heater layer, keeping the insulating film at a constant thickness of 200 μm (8 mils). The data shows the film thermal resistance to be insensitive to this change. This suggests that the resistance comes mainly from the insulating ceramic layer. Consequently, the effect of cutting the Al₂O₃ thickness by 2 mils from Data Sets B to C clearly shows a corresponding 27 % drop in film thermal resistance. An Al₂O₃ thickness of 200 μm (8 mils) was the thinnest layer of ceramic required to provide adequate electrical insulation from the faceplate.

Comparison of Data Sets A and B illustrates the effect of changing the insulating material from MgO to Al₂O₃. Although the bulk thermal conductivities of the two ceramics are very similar ($k_{Al_2O_3} = 39$ W/m·K, whereas $k_{MgO} = 46$ W/m·K at 20 °C), the film thermal resistance halved after switching to Al₂O₃. Vendor 1 consistently had problems with adhesion of MgO layers; Al₂O₃ was utilized in all subsequent runs.

Due to the calculation method, the estimated value of h does not affect $R_{th,total}$. However, h has a minor impact on the value of $R_{th,films}$. For example, changing h from 200,000 W/m²·K to 300,000 W/m²·K, lowers the boundary layer thermal resistance from 5 m²·K/MW to 3.33 m²·K/MW; this increases $R_{th,films}$ by only 1.67 m²·K/MW. Alternatively, if a value of 100,000 W/m²·K were used for h , the value of $R_{th,films}$ would drop by 5 m²·K/MW. This is at most an 11% change in the calculated value of $R_{th,films}$ shown in Table 14. The computed values of $R_{th,films}$ are fairly insensitive to the value of h used in the calculation. This is due to the fact that the thermal resistance across the films is much larger than that contributed by the boundary layer.

6.5 Heater Failure

All thin film heaters failed at heater surface temperatures of approximately 600 °C. Data Sets A - B utilized nickel heaters and failed at 3.5 and 4.4 kW, respectively. Data Sets C - G utilized molybdenum heaters and failed at approximately 7 kW. In either case, the failure was not attributed to a particular vendor. The point at which the heater failed was marked by the occurrence of an electric arc, fracture and localized melting of the heater film. The nickel films failed at low current and high voltage while the molybdenum films failed at high current and low voltage. All heaters failed at approximately 600 °C. Table 15 summarizes peak surface temperature and heat flux data at failure for the various heater configurations.

Film failure may be attributed to the thermal expansion effects of the faceplate/heater composite. Thin films such as the heater and the ceramic insulator are inherently fragile. Differences between the thermal expansion coefficients of the faceplate, ceramic insulator, and heater, coupled with a temperature rise from 30 °C to 600 °C, may result in large heater surface stresses leading to failure. In addition, film stresses owed to large temperature gradients present across the film surface may contribute to its failure. Any of these phenomena could initiate a crack.

Table 15 Heat flux and peak surface temperature at failure for various heater/faceplate configurations. Power was slightly increased beyond recorded values prior to heater failure. Italicized values are extrapolated. Underlined data sets provided by Vendor 1, others provided by Vendor 2.

Data Set	Heater Film	Insulating Film	Plate	Heat Flux at Failure (MW/m²)	Peak Temperature at Failure (°C)
<u>A</u>	Ni, 2 mils	MgO, 10 mils	C15715, 3 mm	3.5	676
<u>B</u>	Ni, 10 mils*	Al ₂ O ₃ , 10 mils	C15715, 3 mm	4.1	579
<u>C</u>	Mo, 10 mils	Al ₂ O ₃ , 8 mils	C15715, 3 mm	7.0	598
D	Mo, 10 mils	Al ₂ O ₃ , 8 mils	TZM, 3.2 mm	7.1	605
E	Mo, 3 mils	Al ₂ O ₃ , 8 mils	TZM, 2.3 mm	6.7	725
F	Mo, 5 mils	Al ₂ O ₃ , 8 mils	TZM, 2.3 mm	7.2	640
G	Mo, 7 mils	Al ₂ O ₃ , 8 mils	TZM, 2.3 mm	6.6	630

* Sanded down to 6 mils.

Once a crack has formed an unstable situation occurs. As the crack propagates, the current densities increase as current flow is restricted into an increasingly smaller area. Further heating in the vicinity of the crack increases the magnitude of thermal stress locally and eventually the crack propagates across the entire heater.

As the heater surface temperatures increase beyond 600 °C, the air filled region directly above the heater fills with electrons; thermoionic electron emission from conductor surfaces is a possible mechanism of electron emission and is typical at such temperatures.⁴⁴ Once the crack propagates across the entire heater surface, the resistance of the heater increases substantially and current flows preferentially through the electron rich region above the heater, forming an arc between the electrodes.⁴⁵

Such reasoning suggests it is unlikely that arcing destroyed the films, rather the film fracture led to arcing. Upon observation of several crack patterns, it is apparent that the direction of crack propagation is horizontal, whereas the electric field gradient is in the vertical direction between the electrodes. An arc always propagates in the direction of an electric field gradient.

⁴⁴ D.G. Fink and H.W. Beaty, *Standard Handbook for Electrical Engineers*, 13th Edition. New York, NY: McGraw-Hill, p. 4-133.

⁴⁵ G.L. Wilson, Personal Communication, Cambridge, MA, April 23, 1997.

Several important design rules may be applied to extend the operating range of thin film heaters. When using a ceramic insulator, ubiquitous materials such Al_2O_3 are advantageous as their plasma spray characteristics are well understood and the process well controlled. Metals exhibiting high melting temperatures and a high electrical resistivity (relative to other pure metals) are advantageous.

For instance, films based on copper must be substantially thinner (potentially below the limits of plasma spraying) than those based on molybdenum, as copper is a much better electrical conductor. From experimental conclusions and insight provided by Vendor 1, films between 5 and 12 mils are optimal. Below 5 mils, surface coverage and heat generation may not be sufficiently uniform. Above 12 mils, residual stresses inherent in film deposition processes lead to poor adhesion. This was evident in several plates where the plasma sprayed Ni layer was peeling at the edges.

6.6 Future Recommendations

The heaters have all been plasma sprayed using air plasma spraying (APS) technology. Many of the drawbacks of APS can be overcome by switching to vacuum plasma spraying (VPS). High porosity, unmelted particles and oxide inclusions are typical in APS. These inclusions significantly raise the thermal resistance of the deposit. In addition, because the substrates are convectively cooled, residual stresses arise when the molten droplets solidify on the cool substrate.⁴⁶ Vendor 2 claims that the substrate temperature does not exceed 150 °C.

It has been shown that VPS sprayed deposits approach densities very near to theoretical values. Because of the vacuum environment, the problems related to oxide inclusions and trapped air are no longer present. The VPS deposit is also maintained at much higher temperatures than APS deposit. The absence of convective cooling and a longer plasma flame in VPS maintain the substrate at temperatures between 800 °C and 1000 °C. This self-anneals the deposited material,

⁴⁶ S. Sampath and H. Herman, "Rapid Solidification and Microstructure Development During Plasma Spray Deposition," *Journal of Thermal Spray Technology*. Vol. 5. December 1996, pp. 445-456.

providing for significant stress relief and recrystallization and results in enhanced interparticle bonding.⁴⁷

Classical laminate theory may shed some insight into the cause of failure of the heaters. The theory provides stress results of multiple layers of materials bonded to one another. The laminate is assumed to consist of perfectly bonded, infinitesimally thin layers which are non-shear-deformable. The displacements are continuous across the layers such that there is no interfacial slip. A failure criterion unique to laminated composites must be used. Two failure criteria are applicable for such composites. They include the Tsai-Hill and Tsai-Wu failure criteria. The Tsai-Hill criteria is applied to materials of equal strength in compression and tension while the Tsai-Wu criteria is applied to materials of unequal tensile and compressive strengths.⁴⁸

Preliminary studies detailing the causes of the heater failure were conducted. As a first estimate, the faceplate, insulator, heater assembly may be treated as a laminated composite. Finite element analysis based on classical laminate theory (CLT) may be used to determine the stress distribution in a laminate composed of several materials of varying thickness and strength. The faceplate assembly may be modeled subject to simply supported boundary conditions and a linear temperature profile through the thickness.

CLT is better applied to VPS sprayed deposits, where the material properties approach theoretical values. However, in APS sprayed materials, the material properties vary considerably and depend on the manufacturing technique, temperatures and splat velocities. In addition, plasma sprayed molybdenum is brittle.

A problem encountered with using the CLT method is that it does not account for residual stresses. Residual stresses can only be calculated using CLT if each layer is at the same temperature during the spraying process, i.e. there is one temperature at which all the layers are stress free. In APS, the substrate is convectively cooled which keeps at a lower temperature than the sprayed deposits.

⁴⁷ S. Sampath and H. Herman, "Rapid Solidification and Microstructure Development During Plasma Spray Deposition," *Journal of Thermal Spray Technology*. Vol. 5. December 1996, pp. 445-456.

⁴⁸ R.M. Jones, "Mechanics of Composite Materials," McGraw-Hill, New York, NY, 1975. pp. 147-238.

In VPS, the plasma sprayed layers as well as the substrate are all maintained at a high temperature; this allows the simulation of residual stresses using CLT for VPS sprayed composites.

Neutron diffraction has been used in the past to quantify residual stresses in plasma sprayed ceramic coatings. A study showed that residual stresses arising from the inhomogeneous shrinkage of the composites does not significantly determine the stress state. Microcrack formation in the ceramics keeps the stress levels low.⁴⁹ The feasibility of conducting neutron diffraction tests to our faceplate composites should be investigated.

The final step to be taken to characterize heater failure is metallography. The faceplate composite should be cut at various cross-sections and failure sites observed under a microscope. An approximate microcrack size in the molybdenum layer can later be used in crack stress analysis, since it is believed that the molybdenum heater layer fails by crack propagation rather than yielding.

⁴⁹ M.T. Hutchings and A.D. Krawitz, "Measurement of Residual and Applied Stress Using Neutron Diffraction," Kluwer Academic Publishers, Boston, MA, 1992. pp. 451-459.

7. Heating Data

7.1 Power Generation and Absorption

The heating apparatus reached a power level of 7.3 kW at 2347 amps and 3.1 VDC for Data Set D (see Table 14). The power generated was determined by measuring the current through and voltage drop across the thin-film molybdenum heater. This represents the total electrical power dissipated in the film and must be distinguished from the total power absorbed by the impinging liquid jets. An energy balance on the cooling water gives

$$Q_{absorbed} = \rho \dot{Q} c_p \Delta T_{bulk} - \Delta P \dot{Q} \quad (7.1)$$

The heat absorbed is simply the difference between the total energy rise and the energy rise generated by viscous forces. Figure 36 compares the total power dissipated and the total heat absorbed as a function of the system current. Uncertainties due to limitations in the accuracy of temperature rise, pressure, and flow rate measurements have been included for the power absorption curve. The total temperature rise through the module is small at these fluxes, so that viscous heating cannot be ignored and the resolution of temperature is the dominant uncertainty. Uncertainty in the electrical power is small.

Estimates of heat losses by radiation from the heater and conduction into the bus bars must also be considered. As an upper bound, if the heated surface is assumed to behave as a black body, less than 1 % of the total power generated is lost to the surrounding environment by radiation. Conduction losses through the copper bus bar contacts have been estimated to be less than 2 % of the total power. At the maximum power of 7,953 W (Data Set F), conduction losses have been measured to be approximately 95 W. The effects of losses to the environment are demonstrated in Figure 36 for Data Set D, where for a given current, the electrical power dissipated is generally greater than the heat absorbed by the liquid; however, losses are within the uncertainty of the absorbed power.

The heat flux, q , at the faceplate's upper surface was calculated by dividing the electrical power dissipated by the active area of the heater film (2.03 cm by 5.08 cm or 10.3 cm²).

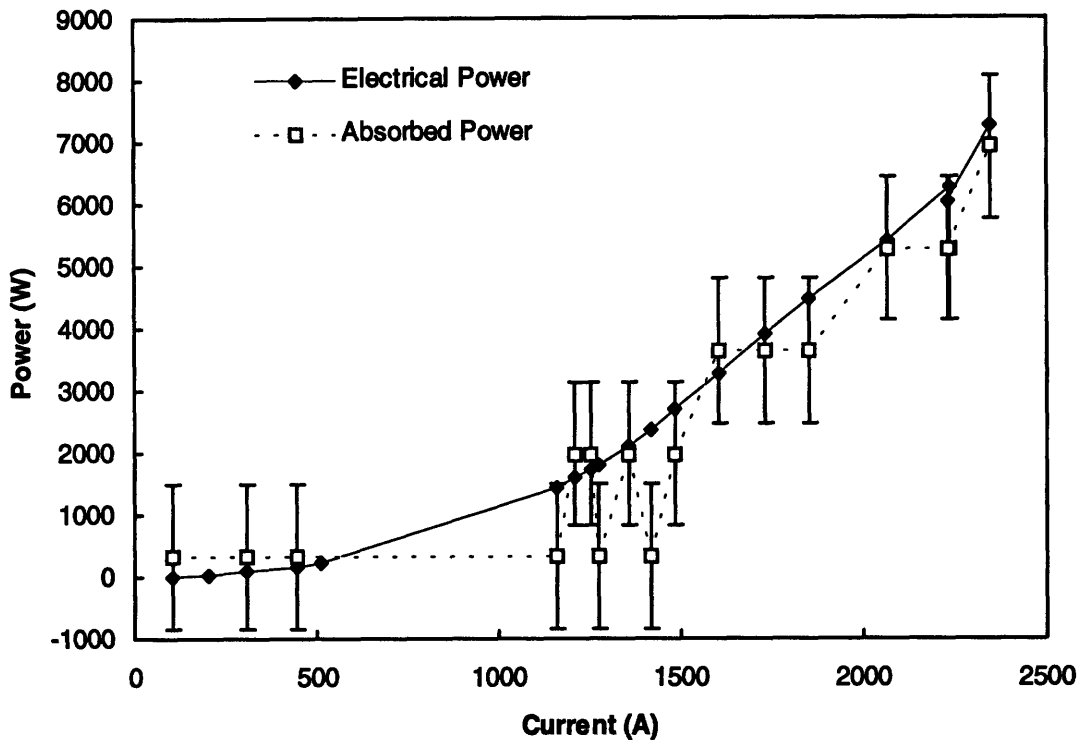


Figure 36 Electrical power dissipated and heat absorbed as a function of the electric current for Data Set D (see Table 14).

7.2 Module Cooling Performance

Test data was acquired for heating powers up to 7.8 kW; this corresponds to a maximum surface averaged flux of 7.2 MW/m² (Data Set F). Temperature measurements were made over the heater film using 4 to 6 type K thermocouples cemented on its forward surface. These thermocouples are separated from each other by 0.5 - 1.0 in. (see Table 1); the cooling water average bulk temperature ranged from 24 to 37 °C as power was increased. The heater surface temperature measurements were averaged and used to compute the average total temperature difference, ΔT , between the heater surface and the average bulk temperature of the water.

Figure 37 through Figure 43 show the heat flux as a function of the average temperature difference between the liquid and heater surface for Data Sets A through G while Figure 44

shows these results on a single chart. The slope quantifies the total thermal resistance, from the heater surface to the flowing liquid and is approximately constant within the scatter of the data. Uncertainties in our measurements of heat flux were calculated and are represented by horizontal error bars. This uncertainty takes into account the error in the area of the heater and errors from our measurements of current through and voltage across the heater film. The vertical error bars represent the spatial temperature scatter at the surface of the heater film.

The graphs clearly illustrate that the heat flux was linearly dependent upon the temperature difference. This behavior is consistent with purely convective heat removal from the faceplate. However, because most of the thermal resistance in the system results from the heater and insulator film, these graphs would not be expected to reveal nonlinearity in the $q-\Delta T$ curve such as might accompany the onset of boiling.

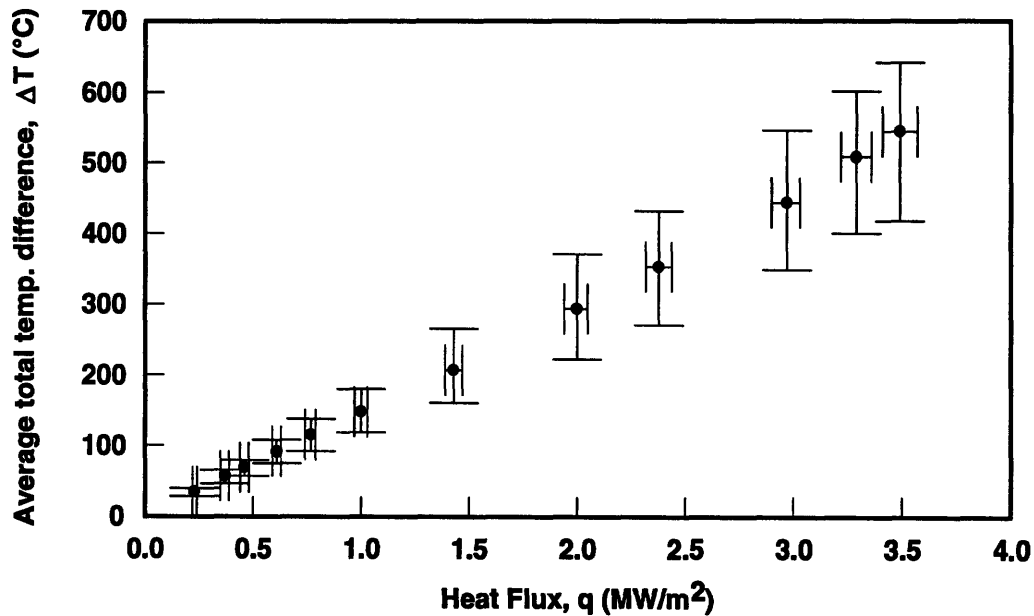


Figure 37 Average temperature difference between the bulk liquid and the heater film's upper surface for Data Set A (see Table 14).

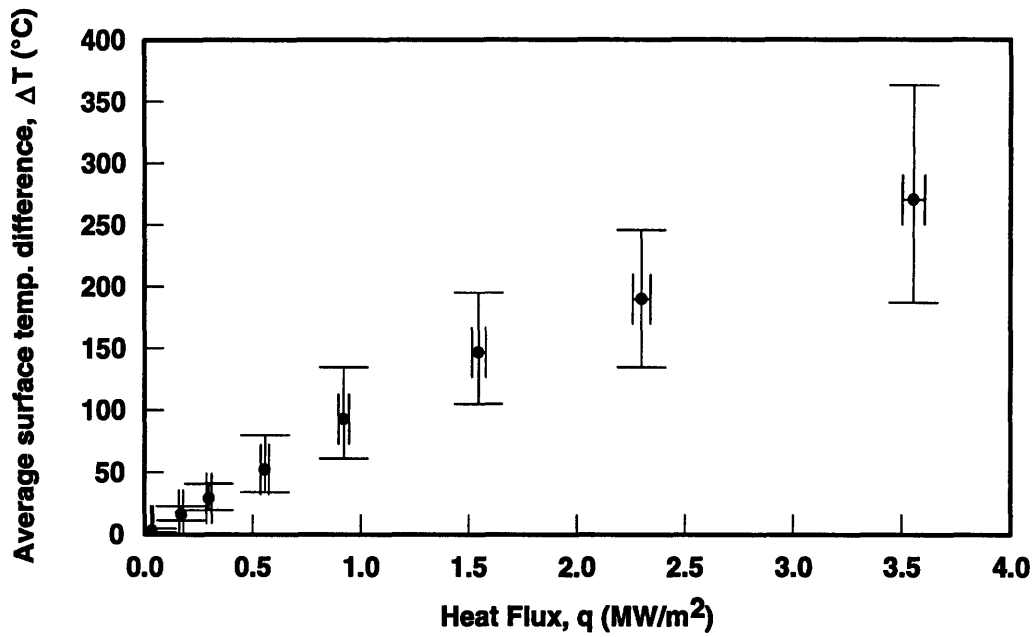


Figure 38 Average temperature difference between the bulk liquid and the heater film's upper surface for Data Set B (see Table 14).

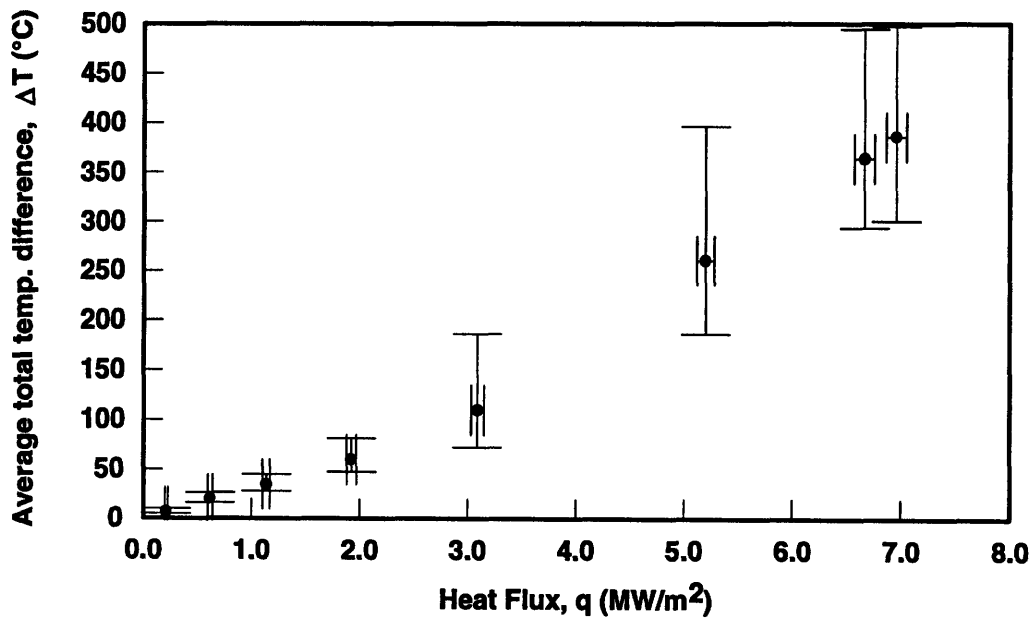


Figure 39 Average temperature difference between the bulk liquid and the heater film's upper surface for Data Set C (see Table 14).

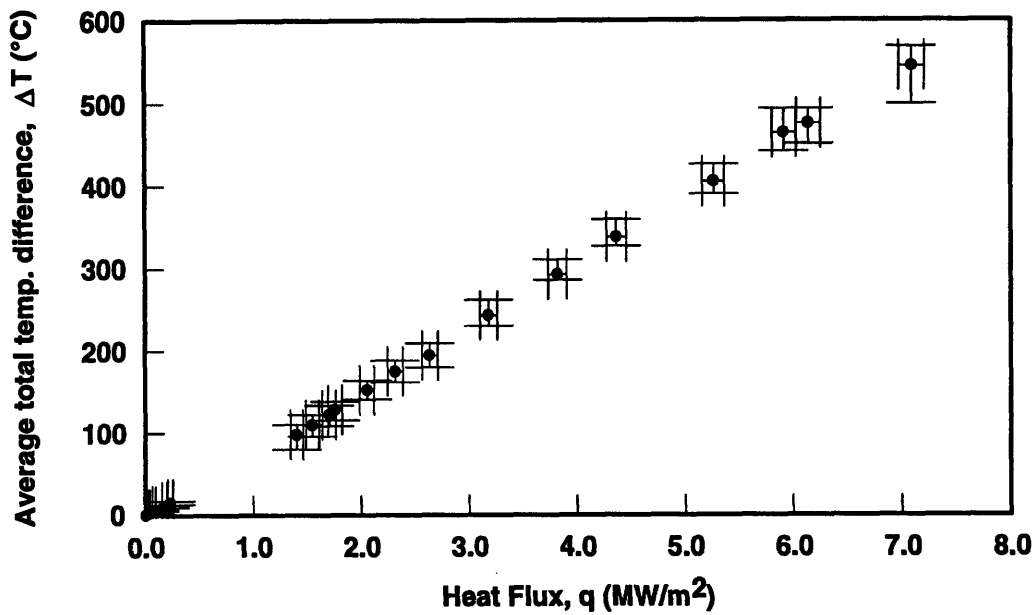


Figure 40 Average temperature difference between the bulk liquid and the heater film's upper surface for Data Set D (see Table 14).

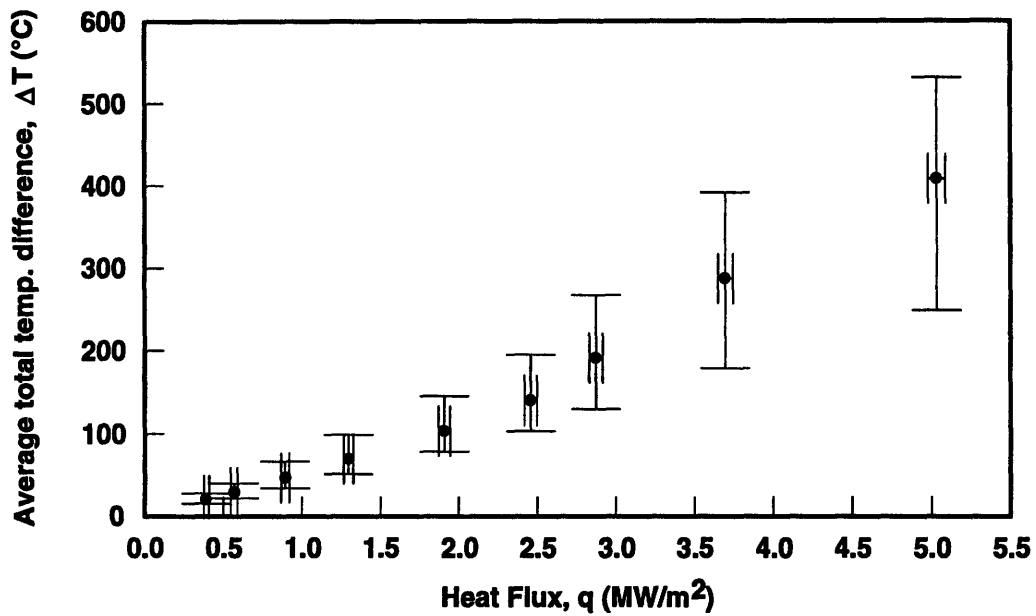


Figure 41 Average temperature difference between the bulk liquid and the heater film's upper surface for Data Set E (see Table 14).

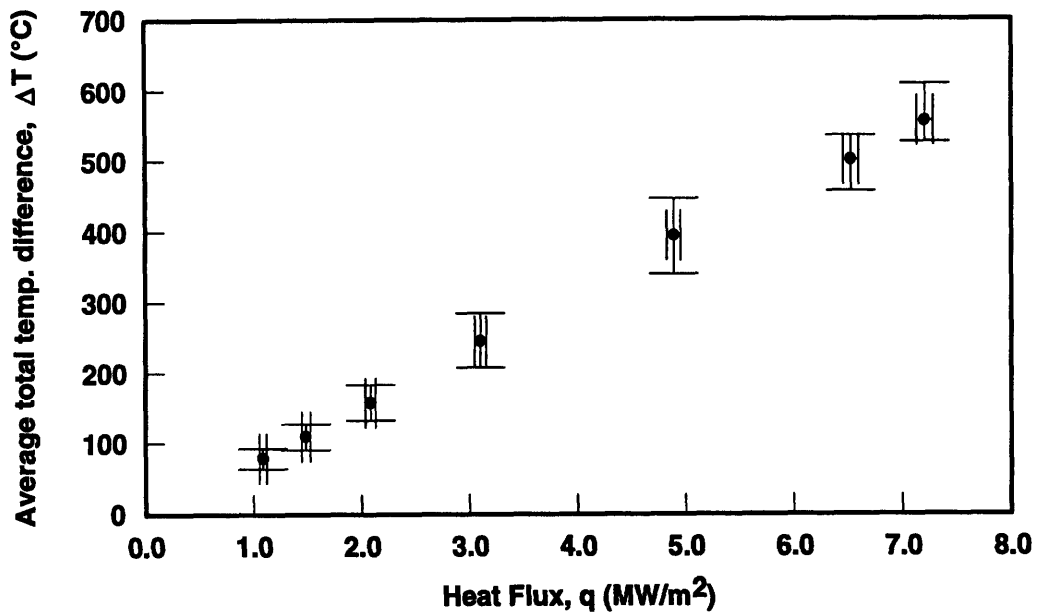


Figure 42 Average temperature difference between the bulk liquid and the heater film's upper surface for Data Set F (see Table 14).

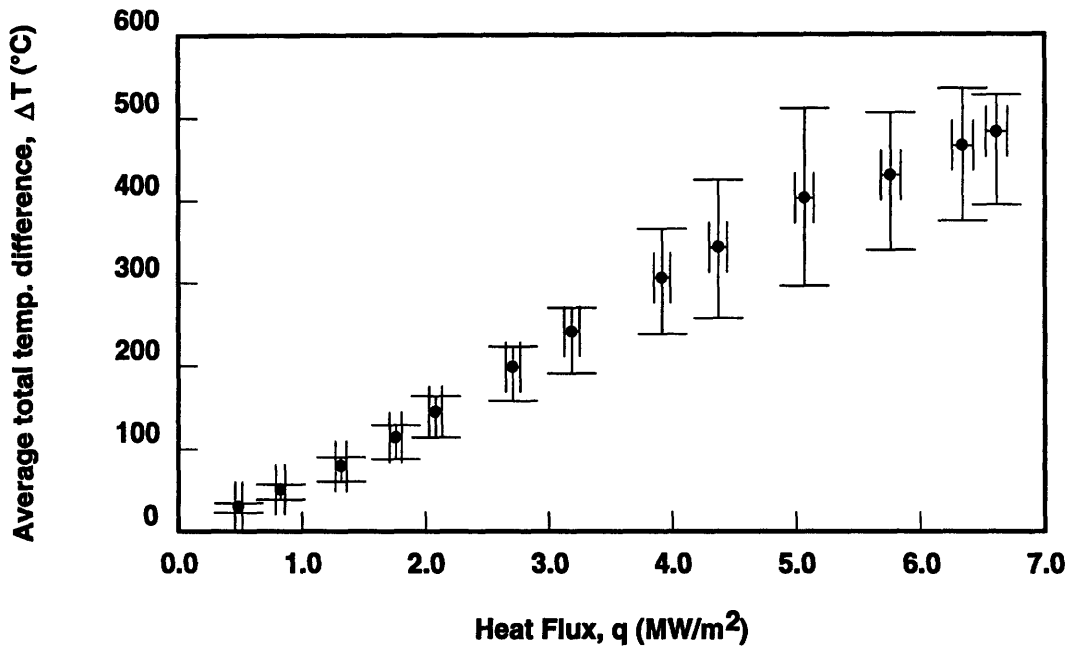


Figure 43 Average temperature difference between the bulk liquid and the heater film's upper surface for Data Set G (see Table 14).

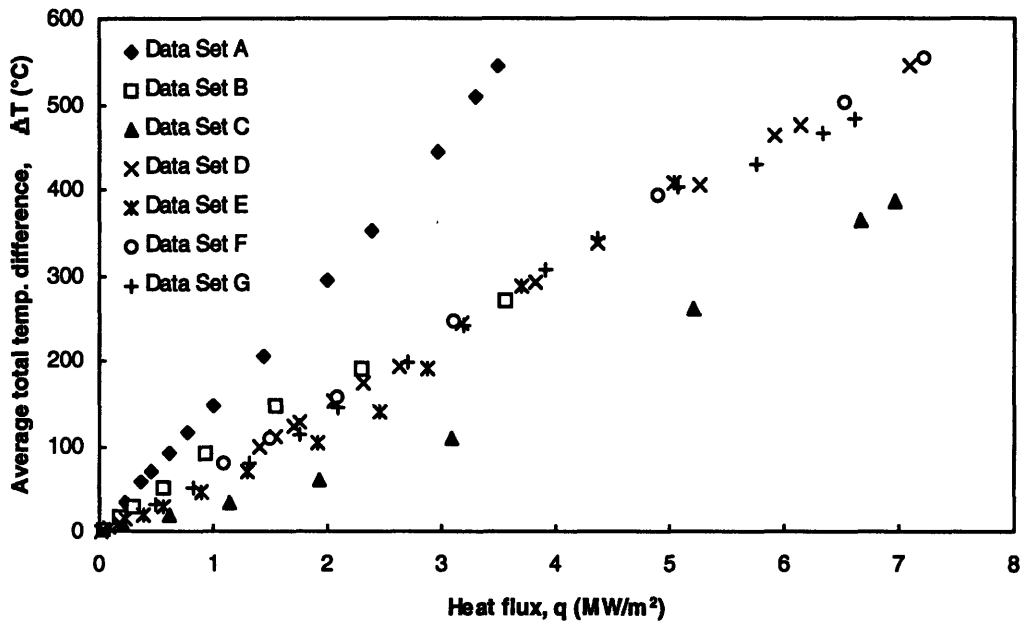


Figure 44 Average temperature difference between the bulk liquid and the heater film's upper surface for Data Sets A-G (see Table 14). Data Set A utilized a 10 mil MgO insulating film and a 3 mm C15715 faceplate. Data Set C utilized an 8 mil Al₂O₃ insulating film and a 3 mm C15715 faceplate.

The temperature distribution across the faceplate assembly for Data Sets D - G is illustrated in Figure 45 through Figure 48. T_0 is the surface averaged temperature across the forward heater surface and T_{bulk} is the average measured water bulk temperature. From these measured temperatures and measured heat fluxes, the remaining temperatures across the faceplate assembly may be computed using the thermal resistance values (see Section 6.4). T_1 is the temperature at the heater/ceramic insulator interface and is equal to T_0 since the heater film's thermal resistance has been taken to be negligible. T_2 is the temperature at the ceramic/faceplate interface and T_3 is the temperature at the back surface of the faceplate directly in contact with the water jets. The heat transfer coefficient, h , was taken to be 200,000 W/m²·K for these calculations. When referring to these graphs, it should be noted that the temperature values carry considerable error due to the scatter in the data. For Data Sets D-G, Figure 40 through Figure 43 illustrate the scatter for T_0 .

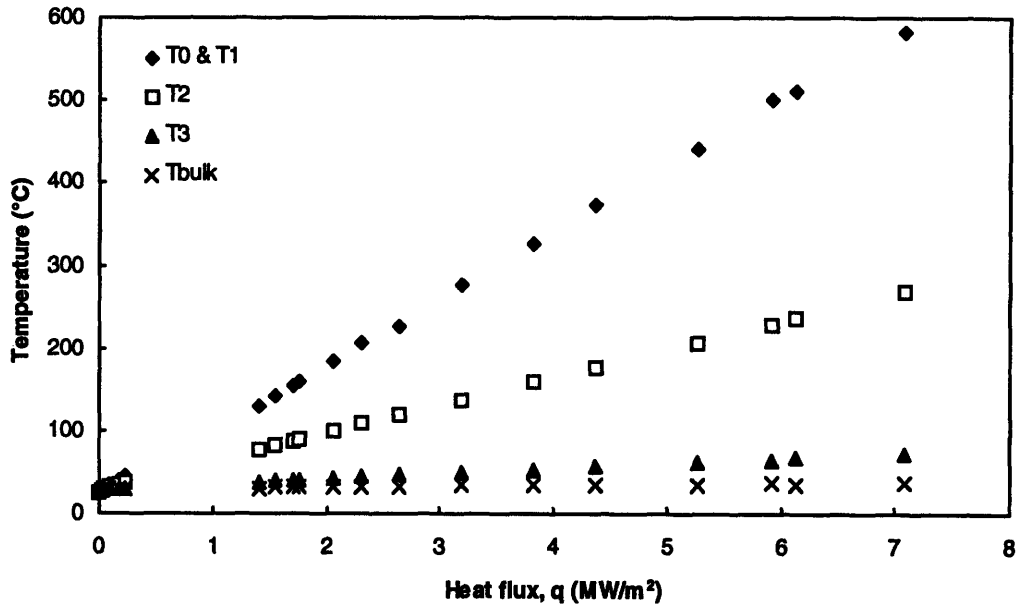


Figure 45 Temperature distribution throughout the faceplate assembly and the bulk liquid for Data Set D.

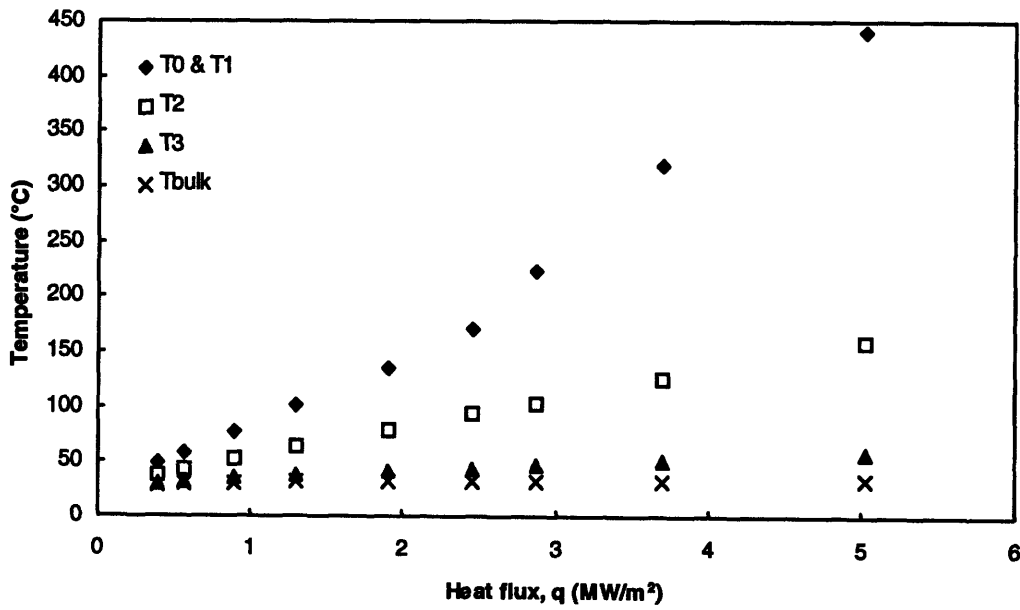


Figure 46 Temperature distribution throughout the faceplate assembly and the bulk liquid for Data Set E.

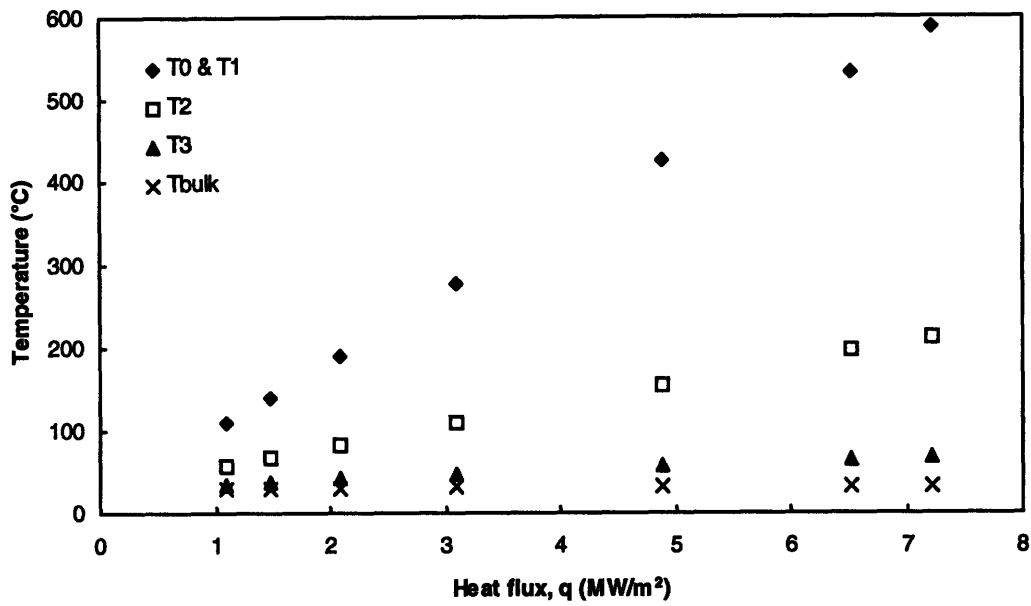


Figure 47 Temperature distribution throughout the faceplate assembly and the bulk liquid for Data Set F.

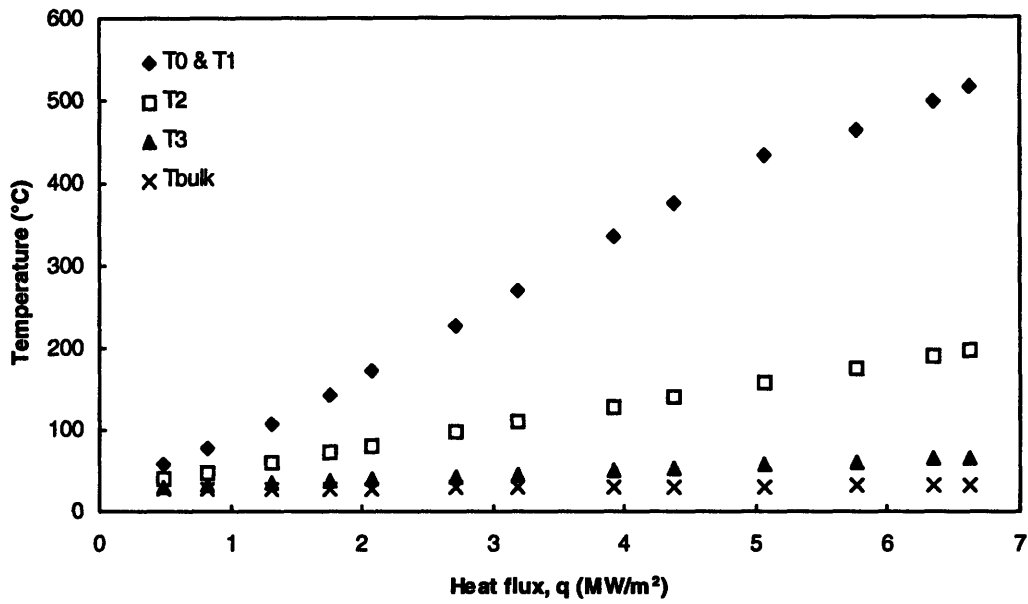


Figure 48 Temperature distribution throughout the faceplate assembly and the bulk liquid for Data Set G.

7.3 Discussion

Several conclusions may be drawn from the observed heat flux data. Most generally, thin film heaters may be effectively used to generate large heat fluxes over large surface areas. Secondly, arrays of impinging liquid jets may be used to convectively cool heated extended areas with heat fluxes of up to 7 MW/m^2 without the onset of boiling and the immediate danger of boiling burnout. Based on finite element simulations, it is important to note that the central jets in the array are removing essentially the full imposed heat flux, while the outermost jets experience a flux that is approximately 50 % lower (see Section 4.2).

The thermal resistance values in the system have been quantified in a one dimensional model, separating the contributions of the films, faceplate and boundary layer as shown in Table 14. The thermal resistance of the films is the major component of the overall thermal resistance; it is between 84 - 94 % of the total thermal resistance for plates supplied by Vendor 1 and no higher than 75 % for Vendor 2. Consequently, most of the temperature drop occurs across the thin films. The thermal resistance of the boundary layer was $5.0 \text{ m}^2 \cdot \text{K/MW}$, based on an estimated heat transfer coefficient of $200,000 \text{ W/m}^2 \cdot \text{K}$.

The effect of changing the faceplate material on the overall thermal resistance can also be seen in the data, as shown in Figure 44. The slope of each data set curve represents the thermal resistance between the heater surface and the cooling water. Data Set A exhibited the largest thermal resistance and was unique in that it utilized a MgO insulating film. The quality of the plasma sprayed MgO was clearly poor. Vendor 1 consistently cited problems with adhesion of MgO onto the faceplate, raising the possibility for a large interfacial thermal contact resistance. The quality of the film was also highly granular and rough, contributing to raise the thermal resistance of the configuration. All future designs utilized Al_2O_3 ceramic insulators.

A reduction in thermal resistance resulted from the use of an Al_2O_3 insulator as shown by Data Sets B-G. Data Set B utilized a 10 mil Al_2O_3 insulator and a dispersion strengthened copper C15715 faceplate. Data Sets D-G utilized an 8 mil Al_2O_3 insulator and molybdenum TZM faceplates. The reduction of Al_2O_3 from Data Set B to Data Sets D-G (which would decrease the thermal resistance) was counterbalanced by switching from the C15715 faceplate of Data Set B to the TZM faceplates of Data Sets D-G (which would increase the thermal resistance). These

differences explain why the thermal resistance values of Data Set B and Data Sets D-G were comparable. Data Set C exhibited the least thermal resistance as it combined the benefits of an 8 mil (as opposed to a 10 mil) Al_2O_3 insulator with the high thermal conductivity C15715 alloy (as opposed to TZM). Furthermore, for all data sets, the temperature difference and the heat flux exhibited a linear relationship. This is characteristic of a convection driven cooling process, as opposed to boiling.

The data shows that the thin-film/faceplate composite can be expected to survive temperature increases of up to 500 °C without film failure due to thermal expansion. The heated faceplate was successfully designed to withstand the imposed thermal stresses, liquid jet pressure loads, and the mechanical boundary loads at the faceplate edges.

Appendix A – Flow Loop Components

Table 16 Parts listing.

Part No.	Qty.	Description
1	1	Gould vert. 8 stage pump, 2 ½" Class 250 flanged suction and discharge.
2	1	Baldor electric motor, 30 HP.
3	1	High density or cross linked polyethylene tank, 500 gallon.
PVC		
4	1	2 ½" Schedule 80 PVC bushing.
5	1	2 ½" Schedule 80 PVC ball valve, union ends.
6	1	1 ¼" Schedule 80 PVC ball valve, threaded ends.
7	1	2" x 239" pipe, Schedule 40, PVC.
8	1	2 ½" x 12" pipe, Schedule 40, PVC.
9	7	2" threaded male adapter, Schedule 40, PVC.
10	1	2 ½" threaded male adapter, Schedule 40, PVC.
11	3	2" standard 90° elbow, Schedule 40, PVC.
12	2	2" threaded male union ends, Schedule 80, PVC.
13	1	2" female adapter, Schedule 40, PVC.
14	1	2" to 2 ½" bushing, Schedule 40, PVC.
15	1	2 ½" coupler, Schedule 40, PVC.
16	1	2" coupler, Schedule 40, PVC.
Steel		
17	2	2 ½" flange, male threaded, raised face, Class 300, 304 S.S.
18	6	2" flange, male threaded, raised face, Class 300, 304 S.S.
19	1	2" x 112" pipe, Schedule 40, 304 S.S.
20	1	2 ½" x 12" pipe, Schedule 40, 304 S.S.
21	1	2 ½" - 2" concentric reducer, Schedule 40, 304 S.S.
22	3	2" long radius elbows, butt weld, Schedule 40, 304 S.S.
23	1	2" Globe Valve, flanged, Class 300, 316 S.S.
24	2	1 ½" Globe valve, flanged, Class 300, 316 S.S.
25	1	3/8" to ¼" male reducing nipple, 316 S.S.
26	1	1 ½" - 1" concentric reducer, Schedule 40, 304 S.S.
27	1	2" - 1 ½" concentric reducer, Schedule 40, 304 S.S.

Support

28	3	2" Nu-Rail Tee.
29	3	2" Nu-Rail flange, rectangular base.
30	3	2" x 34 5/8" pipe, standard black, plain ends.
31	12	3/8" drop in anchors.
32	12	3/8" x 1" bolts.

Instruments

33	1	Omega FTB-109 2" Turbine Meter.
34	1	Omega FLSC-18B Signal Conditioner.
35	1	Omega DPF-64 Rate Meter.
36	2	Omega PX945-500GI Pressure Transducer, 0-500 PSIG.
37	2	Omega DP24-E Process Meter.
38	1	Hoffman CHQR instrument housing box.

Appendix B – Pressure Drop Calculation Across the Nozzles

The pressure drop across the nozzle can be quantified by the following equation,

$$\Delta P_{nozzles} = (k_1 + k_2 + k_3) \frac{1}{2} \rho u_j^2 \quad (\text{B.1})$$

where k_1 , k_2 , and k_3 are pressure loss coefficients. The pressure losses are due to a sharp edge nozzle entrance⁵⁰ (k_1), viscous friction loss across the nozzle length (k_2), and a discharge loss from the nozzle into the upper manifold (k_3). The values for these coefficients are,

$$k_1 = 0.5$$

$$k_2 = f \cdot \frac{L}{D} = 0.017 \cdot \frac{5.08 \text{ cm}}{0.2778 \text{ cm}} = 0.31$$

$$k_3 = 1.0$$

where the friction factor, f , at $\text{Re}_D = 1.5 \times 10^5$ is obtained from a Moody Chart for a smooth pipe.⁵⁰ Hence, the pressure loss may be determined as follows,

$$\begin{aligned} \Delta P_{nozzles} &= (0.5 + 0.31 + 1.0) \frac{1}{2} \rho u_j^2 \\ &= 1.8 \left(\frac{1}{2} \rho u_j^2 \right) \end{aligned}$$

⁵⁰ R.L. Daugherty, J.B. Franzini and E.J. Finnemore, *Fluid Mechanics with Engineering Applications*, McGraw-Hill, Inc., Singapore, 1989.

Appendix C – Temperature Dependent Material Properties

Finite element simulations utilized temperature dependent properties for dispersion strengthened copper (C15715) and molybdenum (TZM). They have been listed in the following tables.

Table 17 Temperature dependent material properties for dispersion strengthened copper (C15715).

Temperature (°C)	Thermal Conductivity (W/m·K)	Modulus of Elasticity (10^{10} N/m ²)	Coefficient of Thermal Expansion (10^{-6} K ⁻¹)
0	360	-	-
20	-	13.00	14.99
100	-	12.52	16.40
200	-	11.80	17.41
300	-	11.07	18.18
400	320	10.35	18.90
500	-	9.632	19.44
600	-	8.908	19.98
700	-	8.184	20.34
800	280	-	20.70
900	-	-	21.06
1000	-	6.012	21.24

Table 18 Temperature dependent material properties for molybdenum (TZM).

Temperature (°C)	Thermal Conductivity (W/m·K)	Modulus of Elasticity (10^{10} N/m ²)	Coefficient of Thermal Expansion (10^{-6} K ⁻¹)
0	126	29.60	-
100	-	-	5.20
500	112	26.16	5.70
1000	99	21.54	5.75
1500	86	13.85	6.51
2000	76	3.080	-

Appendix D – COSMOS/M Finite Element Algorithm

The following algorithm initializes all pertinent parameters, inputs the necessary material properties, constructs the appropriate geometry and applies the desired boundary conditions necessary to analyze a one quarter plate model of the faceplate. The features include parameter declarations for easy modification of the geometry and boundary condition values, temperature dependent material properties, thermal analysis, and linear elastic stress analysis.

C* Establish the proper planar definition and view angle.

```
PLANE,Z,0,1,  
VIEW,1,1,1,0,
```

C* Define necessary parameters for the geometry and boundary conditions.

```
PARASSIGN,PSTAG,REAL,180.0,           Stagnation pressure  
PARASSIGN,HSTAG,REAL,0.1189081,      Stagnation heat transfer coefficient  
PARASSIGN,HMAX,REAL,0.06794753,      Maximum heat transfer coefficient  
PARASSIGN,HEATFLUX,REAL,24.467593,   Heat flux due to heating  
PARASSIGN,AMBTEMP,REAL,98.33,        Water temperature  
PARASSIGN,THICKNESS,REAL,0.157480,   Faceplate thickness  
PARASSIGN,XP,REAL,2.0,               Faceplate width  
PARASSIGN,YP,REAL,2.6,               Faceplate length  
PARASSIGN,XH,REAL,0.8,               Heater width  
PARASSIGN,YH,REAL,2.0,               Heater length  
PARASSIGN,XP2,REAL,XP/2,  
PARASSIGN,YP2,REAL,YP/2,  
PARASSIGN,XH2,REAL,XH/2,  
PARASSIGN,YH2,REAL,YH/2,  
PARASSIGN,XHO,REAL,XP2-XH2,  
PARASSIGN,YHO,REAL,YP2-YH2,
```

C* Establish the faceplate geometry.

```
PT,1,0,0,0,  
PT,2,XP2,0,0,  
PT,3,XP2,YP2,0,  
PT,4,0,YP2,0,  
SCALE,0,  
SF4PT,1,1,2,3,4,0,  
VLEXTR,1,1,1,Z,THICKNESS,  
EGROUP,1,SOLID,0,1,0,0,0,0,0,0,
```

C* Define the necessary material properties.

USER_MAT,1,COPPER_C15715,FPS,
CURDEF,TEMP,1,0,CTE_AL15.DAT,
ACTSET,TP,1,
MPROP,1,ALPX,1,
ACTSET,TP,0,
CURDEF,TEMP,2,0,E_AL15.DAT,
ACTSET,TP,2,
MPROP,1,EX,1,
ACTSET,TP,0,
CURDEF,TEMP,3,0,TC_AL15.DAT,
ACTSET,TP,3,
MPROP,1,KX,1,
ACTSET,TP,0,

C* Mesh the three dimensional model.

M_VL,1,1,1,8,20,25,2,1,1,1,
NMERGE,1,NDMAX,1,0.0001,0,0,0,
NCOMPRESS,1,NDMAX,

C* Apply displacement boundary conditions.

DSF,3,UZ,0,4,1,,
DSF,6,SX,0,6,1,,
DSF,5,SY,0,5,1,,

C* Define the necessary parameters to apply pressure and heat transfer boundary conditions.

PARASSIGN,I,INT,0,
PARASSIGN,PSIG,REAL,0.10,
PARASSIGN,HSIG,REAL,0.16,
PARASSIGN,TOL,REAL,1.0E-005,
PARASSIGN,XC1,REAL,XP2,
PARASSIGN,YC1,REAL,YP2+13/64,
PARASSIGN,XC2,REAL,XP2-11/32,
PARASSIGN,YC2,REAL,YP2,
PARASSIGN,XC3,REAL,XP2+11/32,
PARASSIGN,YC3,REAL,YP2,
PARASSIGN,XC4,REAL,XP2,
PARASSIGN,YC4,REAL,YP2-13/64,
PARASSIGN,XC5,REAL,XP2-11/32,
PARASSIGN,YC5,REAL,YP2-13/32,
PARASSIGN,XC6,REAL,XP2+11/32,
PARASSIGN,YC6,REAL,YP2-13/32,
PARASSIGN,XC7,REAL,XP2,
PARASSIGN,YC7,REAL,YP2-39/64,
PARASSIGN,XC8,REAL,XP2-11/32,
PARASSIGN,YC8,REAL,YP2-26/32,
PARASSIGN,XC9,REAL,XP2+11/32,

Counting index
Pressure Gaussian width
Heat transfer coefficient Gaussian width
Define a zero
Define the jet centers

PARASSIGN,YC9,REAL,YP2-26/32,
PARASSIGN,X,REAL,XELF(11610),
PARASSIGN,Y,REAL,YELF(11610),

Assign element face coordinates

C* Define the Gaussian surface functions for the pressure for each jet.
FUNCDEF,PJET1(PSTAGIPSIGIXC1IYC1IXIY),REAL,PSTAG*EXP(-((X-
XC1)^2)/(2*PSIG^2))*EXP(-((Y-YC1)^2)/(2*PSIG^2)),
FUNCDEF,PJET2(PSTAGIPSIGIXC2IYC2IXIY),REAL,PSTAG*EXP(-((X-
XC2)^2)/(2*PSIG^2))*EXP(-((Y-YC2)^2)/(2*PSIG^2)),
FUNCDEF,PJET3(PSTAGIPSIGIXC3IYC3IXIY),REAL,PSTAG*EXP(-((X-
XC3)^2)/(2*PSIG^2))*EXP(-((Y-YC3)^2)/(2*PSIG^2)),
FUNCDEF,PJET4(PSTAGIPSIGIXC4IYC4IXIY),REAL,PSTAG*EXP(-((X-
XC4)^2)/(2*PSIG^2))*EXP(-((Y-YC4)^2)/(2*PSIG^2)),
FUNCDEF,PJET5(PSTAGIPSIGIXC5IYC5IXIY),REAL,PSTAG*EXP(-((X-
XC5)^2)/(2*PSIG^2))*EXP(-((Y-YC5)^2)/(2*PSIG^2)),
FUNCDEF,PJET6(PSTAGIPSIGIXC6IYC6IXIY),REAL,PSTAG*EXP(-((X-
XC6)^2)/(2*PSIG^2))*EXP(-((Y-YC6)^2)/(2*PSIG^2)),
FUNCDEF,PJET7(PSTAGIPSIGIXC7IYC7IXIY),REAL,PSTAG*EXP(-((X-
XC7)^2)/(2*PSIG^2))*EXP(-((Y-YC7)^2)/(2*PSIG^2)),
FUNCDEF,PJET8(PSTAGIPSIGIXC8IYC8IXIY),REAL,PSTAG*EXP(-((X-
XC8)^2)/(2*PSIG^2))*EXP(-((Y-YC8)^2)/(2*PSIG^2)),
FUNCDEF,PJET9(PSTAGIPSIGIXC9IYC9IXIY),REAL,PSTAG*EXP(-((X-
XC9)^2)/(2*PSIG^2))*EXP(-((Y-YC9)^2)/(2*PSIG^2)),

C* Define the Gaussian surface functions for the heat transfer coefficient for each jet.
FUNCDEF,HJET1(HSTAGIHSIGIXC1IYC1IXIY),REAL,HSTAG*EXP(-((X-
XC1)^2)/(2*HSIG^2))*EXP(-((Y-YC1)^2)/(2*HSIG^2)),
FUNCDEF,HJET2(HSTAGIHSIGIXC2IYC2IXIY),REAL,HSTAG*EXP(-((X-
XC2)^2)/(2*HSIG^2))*EXP(-((Y-YC2)^2)/(2*HSIG^2)),
FUNCDEF,HJET3(HSTAGIHSIGIXC3IYC3IXIY),REAL,HSTAG*EXP(-((X-
XC3)^2)/(2*HSIG^2))*EXP(-((Y-YC3)^2)/(2*HSIG^2)),
FUNCDEF,HJET4(HSTAGIHSIGIXC4IYC4IXIY),REAL,HSTAG*EXP(-((X-
XC4)^2)/(2*HSIG^2))*EXP(-((Y-YC4)^2)/(2*HSIG^2)),
FUNCDEF,HJET5(HSTAGIHSIGIXC5IYC5IXIY),REAL,HSTAG*EXP(-((X-
XC5)^2)/(2*HSIG^2))*EXP(-((Y-YC5)^2)/(2*HSIG^2)),
FUNCDEF,HJET6(HSTAGIHSIGIXC6IYC6IXIY),REAL,HSTAG*EXP(-((X-
XC6)^2)/(2*HSIG^2))*EXP(-((Y-YC6)^2)/(2*HSIG^2)),
FUNCDEF,HJET7(HSTAGIHSIGIXC7IYC7IXIY),REAL,HSTAG*EXP(-((X-
XC7)^2)/(2*HSIG^2))*EXP(-((Y-YC7)^2)/(2*HSIG^2)),
FUNCDEF,HJET8(HSTAGIHSIGIXC8IYC8IXIY),REAL,HSTAG*EXP(-((X-
XC8)^2)/(2*HSIG^2))*EXP(-((Y-YC8)^2)/(2*HSIG^2)),
FUNCDEF,HJET9(HSTAGIHSIGIXC9IYC9IXIY),REAL,HSTAG*EXP(-((X-
XC9)^2)/(2*HSIG^2))*EXP(-((Y-YC9)^2)/(2*HSIG^2)),

C* Begin loop to search for liquid surface and heater surface element coordinates.
#LOOP PRESSLOOP ELMAX
PARASSIGN,I,INT,I+1,
#IF (EXIST(ELI) && LISTSEL(ELI))


```
PARASSIGN,X,REAL,XELF(II6I0),
PARASSIGN,Y,REAL,YELF(II6I0),
PARASSIGN,Z5,REAL,ZELF(II5I0),
PARASSIGN,Z6,REAL,ZELF(II6I0),
#IF (Z6 >= 0.14)
```

C* Define pressure boundary condition value.

```
PARASSIGN,PXY1,REAL,PJET1(PSTAGIPSIGIXC1IYC1IXIY),
PARASSIGN,PXY2,REAL,PJET2(PSTAGIPSIGIXC2IYC2IXIY),
PARASSIGN,PXY3,REAL,PJET3(PSTAGIPSIGIXC3IYC3IXIY),
PARASSIGN,PXY4,REAL,PJET4(PSTAGIPSIGIXC4IYC4IXIY),
PARASSIGN,PXY5,REAL,PJET5(PSTAGIPSIGIXC5IYC5IXIY),
PARASSIGN,PXY6,REAL,PJET6(PSTAGIPSIGIXC6IYC6IXIY),
PARASSIGN,PXY7,REAL,PJET7(PSTAGIPSIGIXC7IYC7IXIY),
PARASSIGN,PXY8,REAL,PJET8(PSTAGIPSIGIXC8IYC8IXIY),
PARASSIGN,PXY9,REAL,PJET9(PSTAGIPSIGIXC9IYC9IXIY),
PARASSIGN,PTOT,REAL,PXY1+PXY2+PXY3+PXY4+PXY5+PXY6+PXY7+PXY8+PXY9
```

C* Define heat transfer coefficient boundary condition value.

```
PARASSIGN,HXY1,REAL,HJET1(HSTAGIHSIGIXC1IYC1IXIY),
PARASSIGN,HXY2,REAL,HJET2(HSTAGIHSIGIXC2IYC2IXIY),
PARASSIGN,HXY3,REAL,HJET3(HSTAGIHSIGIXC3IYC3IXIY),
PARASSIGN,HXY4,REAL,HJET4(HSTAGIHSIGIXC4IYC4IXIY),
PARASSIGN,HXY5,REAL,HJET5(HSTAGIHSIGIXC5IYC5IXIY),
PARASSIGN,HXY6,REAL,HJET6(HSTAGIHSIGIXC6IYC6IXIY),
PARASSIGN,HXY7,REAL,HJET7(HSTAGIHSIGIXC7IYC7IXIY),
PARASSIGN,HXY8,REAL,HJET8(HSTAGIHSIGIXC8IYC8IXIY),
PARASSIGN,HXY9,REAL,HJET9(HSTAGIHSIGIXC9IYC9IXIY),
PARASSIGN,HTOT,REAL,HXY1+HXY2+HXY3+HXY4+HXY5+HXY6+HXY7+HXY8+HXY9
```

C* Apply pressure boundary condition.

```
#IF (PTOT > TOL)
  PEL,I,PTOT,6,I,1,4,
#ENDIF
```

C* Apply heat transfer coefficient and heat flux boundary condition.

```
#IF (HTOT > TOL)
  #IF (HTOT > HMAX)
    PARASSIGN,HTOT,REAL,HMAX
  #ENDIF
  CEL,I,HTOT,AMBTEMP,6,I,1,4,
#ENDIF
#ENDIF
#IF (Z5 <= 0.01)
  #IF ((X >= XHO) && (Y >= YHO))
    HXEL,I,HEATFLUX,5,I,1,
  #ENDIF
```

```
#ENDIF
#ENDIF
#LABEL PRESSLOOP
CLS;
```

```
C* Execute thermal and stress analysis modules.
TREF,70.0,
HT_OUTPUT,1,1,1,
A_THERMAL,S,0.001,1,1,20,0,1,1e+008,0,
R_THERMAL
TEMPREAD,1,1,
A_STATIC,T,
R_STATIC
```

Appendix E – Temperature Data

Measured Quantities

	Thermocouple Measurements on Top of Heater														
	T _{w,in} (°C)	T _{w,out} (°C)	T _{w,av} (°C)	T ₂ (°C)	T ₁ (°C)	T ₃ (°C)	T ₄ (°C)	T ₅ (°C)	T _{Ni,av} (°C)	V _{shunt} (mV)	I (A)	V _{film} (V)	R _{film} (Ω)	Power (W)	q" (MW/m ²)
1	26.8	27.2	27	48.9	51.6				50.25	1.73	104.09	0.99	0.009511	103.05	0.10
2	27.1	27.5	27.3	58.6	61.7				60.15	1.98	119.14	1.16	0.009737	138.20	0.13
3	27.6	28	27.8	85.4	90.1				87.75	2.57	154.64	1.67	0.010799	258.24	0.25
4	27.8	28.2	28	112.4	120.2				116.3	3.02	181.71	2.17	0.011942	394.32	0.38
5	28.2	28.7	28.45	142	152.7				147.35	3.38	203.37	2.71	0.013325	551.15	0.53
6	28.8	29.2	29	165	177.8				171.4	3.63	218.42	3.21	0.014697	701.12	0.68
7	29.1	29.5	29.3	189.9	207.8				198.85	3.82	229.85	3.65	0.015880	838.95	0.81
8	29.4	29.8	29.6	212.8	232.2				222.5	3.99	240.08	4.17	0.017369	1001.13	0.96
9	29.8	30.3	30.05	227.2	246.6				236.9	4.08	245.49	4.48	0.018249	1099.81	1.06
10	30.1	30.6	30.35	248.7	271.2				259.95	4.2	252.71	4.95	0.019587	1250.93	1.21
11	30.5	30.9	30.7	272.4	295.8				284.1	4.33	260.54	5.45	0.020918	1419.92	1.37
12	30.9	31.4	31.15	349.4	388.8				369.1	4.72	284.00	6.7	0.023591	1902.82	1.83

Date	Heater Generation	Heater Material	Heater Thickness (mils)	Heater Thickness (m)	Plate Material	Plate Thickness (m)	Ceramic Material	Ceramic Thickness (mils)	Ceramic Thickness (m)	Theoretical R _{Ni} @ 200°C (Ω)
11-Dec-96	Fourth	Ni	2	0.0000508	C15715	0.004	MgO	10	0.000254	0.001243

Heater Length (dir. of I) (m)	Heater Width (m)	Heater Area (m ²)	Flow Rate (GPM)	Number of nozzles	Nozzle I.D. (m)	Jet Velocity (m/s)	P _{in} (psi)	P _{out} (psi)	Estimated h (W/m ² K)
0.02037	0.05095	0.001038	62.5	14	0.002778	46.47	315.7	84	200000

Calculated Quantities

	$T_{w,av}$	$T_{Ni,av}$	ΔT_{av}	q''	$T_{Water-Cu}$	$T_{Cu-MgOxide}$	Effective $R_{thermal}$ (Ni/MgOxide)	$R_{thermal}$ (total)	P_{Ni} (calculated using R_{film})
	(°C)	(°C)	(°C)	(MW/m ²)	(°C)	(°C)	(m ² ·K/MW)	(m ² ·K/MW)	(Ωm)
1	27	51.60	24.60	0.10	27.50	28.63	217.74	247.77	1.208E-06
2	27.3	61.70	34.40	0.13	27.97	29.49	230.29	258.36	1.237E-06
3	27.8	90.10	62.30	0.25	29.04	31.89	224.52	250.40	1.372E-06
4	28	120.20	92.20	0.38	29.90	34.24	216.00	242.69	1.517E-06
5	28.45	152.70	124.25	0.53	31.10	37.17	207.49	233.99	1.693E-06
6	29	177.80	148.80	0.68	32.38	40.10	194.38	220.28	1.867E-06
7	29.3	207.80	178.50	0.81	33.34	42.58	193.34	220.84	2.018E-06
8	29.6	232.20	202.60	0.96	34.42	45.45	183.56	210.05	2.207E-06
9	30.05	246.60	216.55	1.06	35.35	47.46	178.79	204.37	2.319E-06
10	30.35	271.20	240.85	1.21	36.38	50.15	174.08	199.84	2.489E-06
11	30.7	295.80	265.10	1.37	37.54	53.17	168.80	193.78	2.658E-06
12	31.15	388.80	357.65	1.83	40.32	61.27	167.92	195.09	2.998E-06

Date	k C15715 @ 100 °C	Average $R_{thermal}$	1/h	Tabulated P_{Ni} @ 200°C
	(W/mK)	(m ² ·K/MW)	(m ² ·K/MW)	(Ωm)
11-Dec-96	350	196.41	5.00	1.58E-07

Notes / Misc. Features:

Plate only slightly bowed.
MgO insulator being used. Thickened pads of Ni used (10-15 mils) thick.
Did not fail, saved for two more runs.
Only 2 thermocouples used.
Vendor 1.

Measured Quantities

	Thermocouple Measurements on Top of Heater										V_{shunt} (mV)	I (A)	V_{film} (V)	R_{film} (Ω)	Power (W)	q'' (MW/m ²)
	$T_{w,in}$ (°C)	$T_{w,out}$ (°C)	$T_{w,av}$ (°C)	T_2 (°C)	T_1 (°C)	T_3 (°C)	T_4 (°C)	T_5 (°C)	$T_{Ni,av}$ (°C)							
0	28.9	29.4	29.15		28.5	28.8			28.65							
1	29.8	30.2	30		43.5	44			43.75	1.8	108.31	1.05	0.00969	113.72	0.11	
2	30.3	30.7	30.5		58	57.3			57.65	2.36	142.00	1.48	0.01042	210.16	0.20	
3	30.8	31.1	30.95		66.6	66			66.3	2.63	158.25	1.74	0.01100	275.35	0.27	
4	31.1	31.4	31.25		85.8	86.5			86.15	3.06	184.12	2.26	0.01227	416.11	0.40	
5	31.3	31.7	31.5		117.7	119.8			118.75	3.55	213.60	3.11	0.01456	664.31	0.64	
6	31.8	32.2	32		144.7	148.9			146.8	3.82	229.85	3.85	0.01675	884.92	0.85	
7	32.1	32.6	32.35		174.5	174.4			174.45	4.05	243.69	4.71	0.01933	1147.77	1.11	
8	33.9	34.4	34.15		218.6	213.5			216.05	4.28	257.53	5.86	0.02275	1509.11	1.45	

Date	Heater Generation	Heater Material	Heater Thickness (mils)	Heater Thickness (m)	Plate Material	Plate Thickness (m)	Ceramic Material	Ceramic Thickness (mils)	Ceramic Thickness (m)	Theoretical R_{Ni} @ 200°C (Ω)
11-Dec-96	Fourth	Ni	2	0.0000508	C15715	0.004	MgO	10	0.000254	0.001243

Heater Length (dir. of I) (m)	Heater Width (m)	Heater Area (m ²)	Flow Rate (GPM)	Number of nozzles	Nozzle I.D. (m)	Jet Velocity (m/s)	P_{in} (psi)	P_{out} (psi)	Estimated h (W/m ² K)
0.02037	0.05095	0.001038	62.5	14	0.002778	46.47	315	84	200000

Calculated Quantities

	$T_{w,av}$	$T_{Ni,av}$	ΔT_{av}	q''	$T_{Water-Cu}$	$T_{Cu-MgOxide}$	Effective $R_{thermal}$ (Ni/MgOxide)	$R_{thermal}$ (total)	P_{Ni} (calculated using R_{film})
	(°C)	(°C)	(°C)	(MW/m ²)	(°C)	(°C)	(m ² ·K/MW)	(m ² ·K/MW)	(Ωm)
0	29.15	28.65	-0.50	0.00	29.15	29.15			
1	30	43.75	13.75	0.11	30.55	31.80	109.07	125.50	1.232E-06
2	30.5	57.65	27.15	0.20	31.51	33.83	117.66	134.09	1.324E-06
3	30.95	66.30	35.35	0.27	32.28	35.31	116.82	133.25	1.397E-06
4	31.25	86.15	54.90	0.40	33.25	37.84	120.51	136.94	1.560E-06
5	31.5	118.75	87.25	0.64	34.70	42.01	119.89	136.32	1.850E-06
6	32	146.80	114.80	0.85	36.26	46.01	118.22	134.65	2.128E-06
7	32.35	174.45	142.10	1.11	37.88	50.52	112.07	128.50	2.456E-06
8	34.15	216.05	181.90	1.45	41.42	58.04	108.68	125.11	2.891E-06

Date	k C15715 @ 100 °C	Average $R_{thermal}$	1/h	Tabulated P_{Ni} @ 200°C
	(W/mK)	(m ² ·K/W)	(m ² ·K/MW)	(Ωm)
11-Dec-96	350	115.37	5.00	1.58E-07

Notes / Misc. Features:

T_2 got disconnected and data did have to get discarded.
 Plate only slightly bowed.
 MgO insulator being used. Thickened pads of Ni used (10-15 mils) thick.
 Did not fail, saved for one more run.
 Vendor 1.

Measured Quantities

	Thermocouple Measurements on Top of Heater										$T_{Ni,av}$ (°C)	V_{shunt} (mV)	I (A)	V_{film} (V)	R_{film} (Ω)	Power (W)	q'' (MW/m ²)
	$T_{w,in}$ (°C)	$T_{w,out}$ (°C)	$T_{w,av}$ (°C)	T_2 (°C)	T_1 (°C)	T_3 (°C)	T_4 (°C)	T_5 (°C)	T_6 (°C)								
0	35	35.4	35.2	34.5	32.7	34.1					33.77	0.00	0.00	0.00		0.00	0.00
1	35.4	35.8	35.6	64.2	48.3	52.1					54.87	1.96	117.93	1.26	0.01068	148.60	0.14
2	35.9	36.2	36.05	81.2	57.8	62.9					67.30	2.37	142.60	1.63	0.01143	232.44	0.22
3	36	36.4	36.2	102.5	71.2	77.2					83.63	2.79	167.87	2.08	0.01239	349.18	0.34
4	36.4	36.7	36.55	122.6	82.3	91.4					98.77	3.09	185.93	2.50	0.01345	464.81	0.45
5	36.6	36.9	36.75	162.2	108.4	122.2					130.93	3.54	213.00	3.37	0.01582	717.82	0.69
6	36.8	37.2	37	216.4	149.7	168.9					178.33	3.92	235.87	4.70	0.01993	1108.57	1.07
7	37.4	37.8	37.6	286.7	200.3	221.4					236.13	4.17	250.91	5.99	0.02387	1502.94	1.45
8	37.6	38.1	37.85	349.6	241.1	262.5					284.40	4.39	264.15	6.99	0.02646	1846.38	1.78
9	38.1	38.5	38.3	395.4	265.1	288.8					316.43	4.58	275.58	7.67	0.02783	2113.69	2.04

Date	Heater Generation	Heater Material	Heater Thickness (mils)	Heater Thickness (m)	Plate Material	Plate Thickness (m)	Ceramic Material	Ceramic Thickness (mils)	Ceramic Thickness (m)	Theoretical R_{Ni} @ 200°C (Ω)
11-Dec-96	Fourth	Ni	2	0.0000508	C15715	0.004	MgO	10	0.000254	0.001243

Heater Length (dir. of I) (m)	Heater Width (m)	Heater Area (m ²)	Flow Rate (GPM)	Number of nozzles	Nozzle I.D. (m)	Jet Velocity (m/s)	P_{in} (psi)	P_{out} (psi)	Estimated h (W/m ² K)
0.02037	0.05095	0.001038	62.4	14	0.002778	46.40	313.2	84	200000

Calculated Quantities

	$T_{w,av}$	$T_{Ni,av}$	ΔT_{av}	q''	$T_{Water-Cu}$	$T_{Cu-MgO\ oxide}$	Effective $R_{thermal}$ (Ni/MgO oxide)	$R_{thermal}$ (total)	ρ_{Ni} (calculated using R_{film})
	(°C)	(°C)	(°C)	(MW/m ²)	(°C)	(°C)	(m ² ·K/MW)	(m ² ·K/MW)	(Ωm)
0	35.2	33.77	-1.43	0.00	35.20	35.20			
1	35.6	54.87	19.27	0.14	36.32	37.95	118.15	134.58	1.358E-06
2	36.05	67.30	31.25	0.22	37.17	39.73	123.11	139.54	1.452E-06
3	36.2	83.63	47.43	0.34	37.88	41.73	124.57	141.00	1.574E-06
4	36.55	98.77	62.22	0.45	38.79	43.91	122.50	138.93	1.709E-06
5	36.75	130.93	94.18	0.69	40.21	48.11	119.76	136.19	2.010E-06
6	37	178.33	141.33	1.07	42.34	54.55	115.90	132.33	2.532E-06
7	37.6	236.13	198.53	1.45	44.84	61.39	120.68	137.11	3.033E-06
8	37.85	284.40	246.55	1.78	46.74	67.07	122.17	138.60	3.362E-06
9	38.3	316.43	278.13	2.04	48.48	71.76	120.15	136.58	3.536E-06

Date	k C15715 @ 100 °C	Average $R_{thermal}$	1/h	Tabulated ρ_{Ni} @ 200°C
	(W/mK)	(m ² ·K/MW)	(m ² ·K/MW)	(Ωm)
11-Dec-96	350	120.78	5.00	1.58E-07

Notes / Misc. Features:

Plate only slightly bowed.
MgO insulator being used. Thickened pads of Ni used (10-15 mils) thick.
Plate failed and arced.
Vendor 1.

Measured Quantities

	Thermocouple Measurements on Top of Heater										V_{shunt} (mV)	I (A)	V_{film} (V)	R_{film} (Ω)	Power (W)	q'' (MW/m ²)
	$T_{w,in}$ (°C)	$T_{w,out}$ (°C)	$T_{w,av}$ (°C)	T_2 (°C)	T_1 (°C)	T_3 (°C)	T_5 (°C)	T_7 (°C)	$T_{Ni,av}$ (°C)							
0	27.2	27.6	27.4		26.4		26.6	26.9	26.63	0	0			0	0	
1	28	28.4	28.2		56.2		56	46.7	52.97	1.93	116.13	1.6	0.01378	185.80	0.188	
2	28.4	28.7	28.55		85.1		89.2	69.6	81.30	2.52	151.63	2.36	0.01556	357.84	0.362	
3	29	29.4	29.2		99.1		104.9	82.5	95.50	2.76	166.07	2.78	0.01674	461.67	0.467	
4	29.4	29.8	29.6		121.8		128.1	100.1	116.67	3	180.51					
5	30.1	30.5	30.3		152.7		161	127.1	146.93	3.29	197.96	4.03	0.02036	797.78	0.807	
6	30.5	30.9	30.7		187.4		197.6	160.8	181.93	3.54	213.00	4.92	0.02310	1047.97	1.059	
7	31.1	31.5	31.3		217.8		230.5	196.1	214.80	3.84	231.05	6.08	0.02631	1404.80	1.420	
8	32.1	32.6	32.35		290.8		294.2	241.1	275.37	4.38	263.54	7.94	0.03013	2092.54	2.115	

Date	Heater Generation	Heater Material	Heater Thickness (mils)	Heater Thickness (m)	Plate Material	Plate Thickness (m)	Ceramic Material	Ceramic Thickness (mils)	Ceramic Thickness (m)	Theoretical R_{Ni} @ 200°C (Ω)
18-Dec-96	Fourth	Ni	2	0.0000508	C15715	0.002	MgO	10	0.000254	0.001193

Heater Length (dir. of I) (m)	Heater Width (m)	Heater Area (m ²)	Flow Rate (GPM)	Number of nozzles	Nozzle I.D. (m)	Jet Velocity (m/s)	P_{in} (psi)	P_{out} (psi)	Estimated h (W/m ² K)
0.01948	0.05077	0.000989	62.5	14	0.002778	46.47	315.8	83.9	200000

Calculated Quantities

	$T_{w,av}$	$T_{Ni,av}$	ΔT_{av}	q''	$T_{Water-Cu}$	$T_{Cu-MgOxide}$	Effective $R_{thermal}$ (Ni/MgOxide)	$R_{thermal}$ (total)	P_{Ni} (calculated using R_{film})
	(°C)	(°C)	(°C)	(MW/m ²)	(°C)	(°C)	(m ² ·K/MW)	(m ² ·K/MW)	(Ωm)
0	27.40	26.63	-0.77	0.00	27.40	27.40			
1	28.20	52.97	24.77	0.19	29.14	30.21	121.14	131.85	1.82E-06
2	28.55	81.30	52.75	0.36	30.36	32.43	135.10	145.82	2.06E-06
3	29.20	95.50	66.30	0.47	31.53	34.20	131.34	142.05	2.22E-06
4	29.60	116.67	87.07						
5	30.30	146.93	116.63	0.81	34.33	38.94	133.90	144.62	2.70E-06
6	30.70	181.93	151.23	1.06	36.00	42.05	132.04	142.75	3.06E-06
7	31.30	214.80	183.50	1.42	38.40	46.52	118.50	129.21	3.48E-06
8	32.35	275.37	243.02	2.12	42.93	55.02	104.16	114.88	3.99E-06

Date	k C15715 @ 100 °C	Average $R_{thermal}$	1/h	Tabulated P_{Ni} @ 200°C
	(W/mK)	(m ² ·K/MW)	(m ² ·K/MW)	(Ωm)
18-Dec-96	350	125.17	5.00	1.58E-07

Notes / Misc. Features:

Plate only slightly bowed.
MgO insulator being used. Thickened pads of Ni used (10-15 mils) thick.
More thermocouples were mounted, but peeled off. For this reason, cement was used in next run.
In next run, plate was inverted to see if we could track down source of hot spots.
Vendor 1.

Measured Quantities

	Thermocouple Measurements on Top of Heater										V_{shunt} (mV)	I (A)	V_{film} (V)	R_{film} (Ω)	Power (W)	q'' (MW/m ²)
	$T_{w,in}$ (°C)	$T_{w,out}$ (°C)	$T_{w,av}$ (°C)	T_1 (°C)	T_3 (°C)	T_4 (°C)	T_5 (°C)	T_6 (°C)	T_7 (°C)	$T_{Ni,av}$ (°C)						
0	29.2	29.7	29.45	29.9	29.9	30	30.1	30	30.1	30.00						
1	30.4	30.7	30.55	59.5	58.9	69.9	65.1	66.7	70.2	65.05	2.08	125.15	1.8	0.01438	225.28	0.23
2	30.7	31	30.85	78.2	77.2	95.8	88	90.6	96.2	87.67	2.54	152.83	2.4	0.01570	366.80	0.37
3	31	31.3	31.15	89.7	88	109.8	100.3	103.4	110.8	100.33	2.76	166.07	2.73	0.01644	453.37	0.46
4	31.2	31.6	31.4	107.4	106.2	135.7	122.1	127.8	139.8	123.17	3.03	182.32	3.3	0.01810	601.64	0.61
5	31.6	31.9	31.75	128.2	123.8	161.6	144.8	151.8	169.3	146.58	3.27	196.76	3.85	0.01957	757.51	0.77
6	31.8	32.2	32	157.4	150.8	196.6	175.2	183.3	211.1	179.07	3.50	210.60	4.7	0.02232	989.80	1.00
7	32.2	32.6	32.4	208.2	192.6	277.6	222.4	231.7	297.3	238.30	3.76	226.24	6.24	0.02758	1411.73	1.43
8	33	33.5	33.25	285.1	254.8	379.5	305.5	328.3	403.8	326.17	4.00	240.68	8.2	0.03407	1973.58	2.00
9	33.3	33.7	33.5	340.1	303.5	438	375.8	393.9	464.9	386.03	4.15	249.71	9.44	0.03780	2357.22	2.38
10	33.7	34.1	33.9	422.9	381.9	546.7	460.7	474	580	477.70	4.40	264.75	11.08	0.04185	2933.41	2.97
11	34	34.5	34.25	478.3	434.2	623.6	511.1	573	635.2	542.57	4.50	270.77	12.02	0.04439	3254.60	3.29
12	34.2	34.7	34.45	522	452	655	540	627	676	578.67	4.55	273.77	12.6	0.04602	3449.55	3.49

Date	Heater Generation	Heater Material	Heater Thickness (mils)	Heater Thickness (m)	Plate Material	Plate Thickness (m)	Ceramic Material	Ceramic Thickness (mils)	Ceramic Thickness (m)	Theoretical R_{Ni} @ 300°C (Ω)
18-Dec-96	Fourth	Ni	2	0.0000508	C15715	0.003	MgO	10	0.000254	0.001699

Heater Length (dir. of I) (m)	Heater Width (m)	Heater Area (m ²)	Flow Rate (GPM)	Number of nozzles	Nozzle I.D. (m)	Jet Velocity (m/s)	P_{in} (psi)	P_{out} (psi)	Estimated h (W/m ² K)
0.01948	0.05077	0.000989	62.6	14	0.002778	46.54	314.5	84	200000

Calculated Quantities

	$T_{w,av}$	$T_{Ni,av}$	ΔT_{av}	q''	$T_{Water-Cu}$	$T_{Cu-MgOxide}$	Effective $R_{thermal}$ (Ni/MgOxide)	$R_{thermal}$ (total)	P_{Ni} (calculated using R_{film})
	(°C)	(°C)	(°C)	(MW/m ²)	(°C)	(°C)	(m ² -K/MW)	(m ² -K/MW)	(Ωm)
0	29.45	30.00	0.55	0.00	29.45	29.45			
1	30.55	65.05	34.50	0.23	31.69	33.64	137.92	151.49	1.90E-06
2	30.85	87.67	56.82	0.37	32.70	35.88	139.65	153.22	2.08E-06
3	31.15	100.33	69.18	0.46	33.44	37.37	137.38	150.95	2.18E-06
4	31.40	123.17	91.77	0.61	34.44	39.65	137.31	150.88	2.40E-06
5	31.75	146.58	114.83	0.77	35.58	42.14	136.38	149.95	2.59E-06
6	32.00	179.07	147.07	1.00	37.00	45.58	133.40	146.98	2.95E-06
7	32.40	238.30	205.90	1.43	39.54	51.77	130.70	144.27	3.65E-06
8	33.25	326.17	292.92	2.00	43.23	60.33	133.24	146.81	4.51E-06
9	33.50	386.03	352.53	2.38	45.42	65.84	134.37	147.94	5.01E-06
10	33.90	477.70	443.80	2.97	48.73	74.15	136.08	149.65	5.54E-06
11	34.25	542.57	508.32	3.29	50.70	78.90	140.92	154.49	5.88E-06
12	34.45	578.67	544.22	3.49	51.89	81.78	142.49	156.06	6.09E-06

Date	k C15715 @ 100 °C	Average $R_{thermal}$	1/h	Tabulated P_{Ni} @ 300°C
	(W/mK)	(m ² -K/MW)	(m ² -K/MW)	(Ωm)
18-Dec-96	350	136.65	5.00	2.25E-07

Notes / Misc. Features:

Data set A, vendor 1.
 Plate only slightly bowed.
 MgO insulator being used. Thickened pads of Ni used (10-15 mils) thick.
 Cement used. Plate was inverted from previous run.
 Plate failed and arced.

Measured Quantities

	Thermocouple Measurements on Top of Heater (does not include T ₂)											I (A)	V _{film} (V)	R _{film} (Ω)	Power (W)	q" (MW/m ²)	
	T _{w,in} (°C)	T _{w,out} (°C)	T _{w,av} (°C)	T ₂ (°C)	T ₃ (°C)	T ₄ (°C)	T ₅ (°C)	T ₆ (°C)	T ₇ (°C)	T _{Ni,av} (°C)	V _{shunt} (mV)						
0	23.5	23.8	23.65	22.6	22.6	22.5	23.2	22.7	22.8	22.76							
1	24.6	25	24.8	24.5	30.1	40.5	41.6	29.4	29.5	34.22	2.16	129.97	1.870	0.01439	243.04	0.234	
2	24.9	25.3	25.1	24.9	33.8	50.4	52	33.3	33.3	40.56	2.63	158.25	2.510	0.01586	397.20	0.382	
3	25.3	25.6	25.45	25.5	39.8	68.9	71	40.6	40.2	52.10	3.05	183.52	3.260	0.01776	598.27	0.575	
4	25.6	26	25.8	25.9	44.7	83.9	87.3	46.2	45.5	61.52	3.24	194.95	3.740	0.01918	729.12	0.701	
5	25.9	26.3	26.1	26.4	50.2	102.8	111	54.6	54	74.52	3.47	208.79	4.510	0.02160	941.64	0.905	
6	26.2	26.6	26.4	27.1	61.8	136.9	150	68.7	68.5	97.18	3.77	226.84	5.350	0.02358	1213.60	1.167	
7	26.6	27	26.8	27.9	75.7	173	183	82.3	81.4	119.08	4.01	241.28	6.250	0.02590	1508.01	1.450	
8	27.4	27.9	27.65	29.9	114	207.3	216	103	98.7	147.80	4.30	258.73	7.140	0.02760	1847.34	1.776	

Date	Heater Generation	Heater Material	Heater Thickness (mils)	Heater Thickness (m)	Plate Material	Plate Thickness (m)	Ceramic Material	Ceramic Thickness (mils)	Ceramic Thickness (m)	Theoretical R _{Ni} @ 200°C (Ω)
14-Jan-97	Fifth	Ni	12	0.0003048	C15715	0.004	Al ₂ O ₃	10	0.000254	0.000206

Heater Length (dir. of I) (m)	Heater Width (m)	Heater Area (m ²)	Flow Rate (GPM)	Number of nozzles	Nozzle I.D. (m)	Jet Velocity (m/s)	P _{in} (psi)	P _{out} (psi)	Estimated h (W/m ² K)
0.02032	0.05118	0.00104	62.6	14	0.002778	46.54	316.5	84	200000

Calculated Quantities

	$T_{w,av}$	$T_{Ni,av}$	ΔT_{av}	q''	$T_{Water-Cu}$	$T_{Cu-AlOxide}$	Effective $R_{thermal}$ (Ni/AlOxide)	$R_{thermal}$ (total)	ρ_{Ni} (calculated using R_{film})
	(°C)	(°C)	(°C)	(MW/m ²)	(°C)	(°C)	(m ² ·K/MW)	(m ² ·K/MW)	(Ωm)
0	3.65	22.76	-0.89	0.00	23.65	23.65			
1	4.8	34.22	9.42	0.23	25.97	28.64	23.88	40.31	1.105E-05
2	5.1	40.56	15.46	0.38	27.01	31.37	24.05	40.48	1.218E-05
3	5.45	52.10	26.65	0.58	28.33	34.90	29.90	46.33	1.364E-05
4	5.8	61.52	35.72	0.70	29.31	37.32	34.52	50.95	1.473E-05
5	6.1	74.52	48.42	0.91	30.63	40.97	37.05	53.48	1.658E-05
6	6.4	97.18	70.78	1.17	32.23	45.57	44.23	60.66	1.811E-05
7	6.8	119.08	92.28	1.45	34.05	50.62	47.21	63.64	1.989E-05
8	7.65	147.80	120.15	1.78	36.53	56.83	51.21	67.64	2.119E-05

Plate	k C15715 @ 100 °C	Average $R_{thermal}$	$1/h$	Tabulated ρ_{Ni} @ 200°C
	(W/mK)	(m ² ·K/MW)	(m ² ·K/MW)	(Ωm)
1 an-97	350	36.51	5.00	1.58E-07

Notes / Misc. Features:

- P bowed in the middle. Pressure tape test applied. See tape set number 1. Poor contact on bottom electrode (electrode 2)
- T as observed not to be touching the plate after running the experiment. Hard to tell whether T_2 (italicized) was touching the ceramic
- si it was not taped down with kapton tape.
- V for 1.

Measured Quantities

	Thermocouple Measurements on Top of Heater (does not include T ₂)											I (A)	V _{film} (V)	R _{film} (Ω)	Power (W)	q" (MW/m ²)
	T _{w,in} (°C)	T _{w,out} (°C)	T _{w,av} (°C)	T ₂ (°C)	T ₁ (°C)	T ₃ (°C)	T ₄ (°C)	T ₅ (°C)	T ₆ (°C)	T _{Ni,av} (°C)	V _{shunt} (mV)					
0	26	26.4	26.2	24.3	24	24.8	24.6	24.1	23.5	24.20	0.00	0.00	0.000	0.00	0.000	
1	26.6	27	26.8	25.3	35	34.3	40.1	37.8	37.8	37.00	1.55	93.26	1.940	0.02080	180.93	0.174
2	26.9	27.2	27.05	25.9	43.7	41.7	51.7	48.2	52.4	47.54	2.03	122.15	2.670	0.02186	326.13	0.314
3	27.2	27.5	27.35	26.5	56.6	52.6	70.8	62.3	73	63.06	2.49	149.82	3.510	0.02343	525.88	0.506

Date	Heater Generation	Heater Material	Heater Thickness (mils)	Heater Thickness (m)	Plate Material	Plate Thickness (m)	Ceramic Material	Ceramic Thickness (mils)	Ceramic Thickness (m)	Theoretical R _{Ni} @ 200°C (Ω)
15-Jan-97	Fifth	Ni	12	0.0003048	C15715	0.004	Al ₂ O ₃	10	0.000254	0.000206

Heater Length (dir. of I) (m)	Heater Width (m)	Heater Area (m ²)	Flow Rate (GPM)	Number of nozzles	Nozzle I.D. (m)	Jet Velocity (m/s)	P _{in} (psi)	P _{out} (psi)	Estimated h (W/m ² K)
0.02032	0.05118	0.00104	62.5	14	0.002778	46.47	316.5	84.2	200000

Calculated Quantities

	$T_{w,av}$	$T_{Ni,av}$	ΔT_{av}	q''	$T_{Water-Cu}$	$T_{Cu-AlOxide}$	Effective $R_{thermal}$ (Ni/AlOxide)	$R_{thermal}$ (total)	P_{Ni} (calculated using R_{film})
	(°C)	(°C)	(°C)	(MW/m ²)	(°C)	(°C)	(m ² ·K/MW)	(m ² ·K/MW)	(Ωm)
0	26.2	24.20	-2.00	0.00	26.20	26.20			
1	26.8	37.00	10.20	0.17	27.67	29.66	42.20	58.63	1.597E-05
2	27.05	47.54	20.49	0.31	28.62	32.20	48.91	65.34	1.678E-05
3	27.35	63.06	35.71	0.51	29.88	35.66	54.19	70.62	1.799E-05

Date	k C15715 @ 100 °C	Average $R_{thermal}$	1/h	Tabulated P_{Ni} @ 200°C
	(W/mK)	(m ² ·K/MW)	(m ² ·K/MW)	(Ωm)
15-Jan-97	350	48.44	5.00	1.58E-07

Notes / Misc. Features:

Plate bowed in the middle.

Plate inverted from Jan 14. Sanded too. Different thermocouple locations since Jan 14. No aluminum foil used.

Only three readings taken since film resistance didn't seem to drop from Jan 14 readings.

Stopped and aluminum foil used (see next run - Jan 15, with Aluminum)

Hard to tell whether T_2 (italicized) was touching the ceramic. T_7 was not touching the heater.

Vendor 1.

Measured Quantities

	Thermocouple Measurements on Top of Heater (does not include T ₂)														
	T _{w,in} (°C)	T _{w,out} (°C)	T _{w,av} (°C)	T ₂ (°C)	T ₁ (°C)	T ₃ (°C)	T ₆ (°C)	T ₇ (°C)	T _{Ni,av} (°C)	V _{shunt} (mV)	I (A)	V _{film} (V)	R _{film} (Ω)	Power (W)	q" (MW/m ²)
0	27.6	28	27.8	25.2			25.4		25.4						
1	27.9	28.2	28.05	26.4			62.8		62.8	2.05	123.35	2.630	0.02132	324.41	0.312
2	28.2	28.6	28.4	27.3			92.6		92.6	2.63	158.25	3.600	0.02275	569.69	0.548
3	28.5	28.8	28.65	28.2			126.2		126.2	3.04	182.92	4.260	0.02329	779.23	0.749
4	28.7	29.1	28.9	29.3			170.4		170.4	3.53	212.40	5.560	0.02618	1180.94	1.136
5	29.2	29.6	29.4	31.5			201		201	3.98	239.48	6.920	0.02890	1657.18	1.593
6	29.5	29.9	29.7	33.9			299		299	4.82	290.02	9.380	0.03234	2720.38	2.616
7	29.8	30.3	30.05	35.8			372		372	5.16	310.48	10.410	0.03353	3232.07	3.108
8	30.1	30.7	30.4	38.1			520		520	6.02	362.22	11.660	0.03219	4223.52	4.061
9	30.7	31.2	30.95	41.5			573		573	6.16	370.65	12.420	0.03351	4603.44	4.426
10	31.2	31.7	31.45				790		790	6.90	415.17	13.420	0.03232	5571.62	5.357

Date	Heater Generation	Heater Material	Heater Thickness (mils)	Heater Thickness (m)	Plate Material	Plate Thickness (m)	Ceramic Material	Ceramic Thickness (mils)	Ceramic Thickness (m)	Theoretical R _{Ni} @ 200°C (Ω)
15-Jan-97	Fifth	Ni	12	0.0003048	C15715	0.004	Al ₂ O ₃	10	0.000254	0.000206

Heater Length (dir. of I) (m)	Heater Width (m)	Heater Area (m ²)	Flow Rate (GPM)	Number of nozzles	Nozzle I.D. (m)	Jet Velocity (m/s)	P _{in} (psi)	P _{out} (psi)	Estimated h (W/m ² K)
0.02032	0.05118	0.00104	62.3	14	0.002778	46.32	315.7	84.2	200000

Calculated Quantities

	$T_{w,av}$	$T_{Ni,av}$	ΔT_{av}	q''	$T_{Water-Cu}$	$T_{Cu-AlOxide}$	Effective $R_{thermal}$ (Ni/AlOxide)	$R_{thermal}$ (total)	P_{Ni} (calculated using R_{film})
	(°C)	(°C)	(°C)	(MW/m ²)	(°C)	(°C)	(m ² ·K/MW)	(m ² ·K/MW)	(Ωm)
0	27.8	25.40	-2.40	0.00	27.80	27.80			
1	28.05	62.80	34.75	0.31	29.61	33.17	94.97	111.40	1.637E-05
2	28.4	92.60	64.20	0.55	31.14	37.40	100.77	117.20	1.746E-05
3	28.65	126.20	97.55	0.75	32.40	40.96	113.77	130.20	1.788E-05
4	28.9	170.40	141.50	1.14	34.58	47.56	108.18	124.61	2.010E-05
5	29.4	201.00	171.60	1.59	37.37	55.58	91.26	107.69	2.218E-05
6	29.7	299.00	269.30	2.62	42.78	72.67	86.52	102.95	2.483E-05
7	30.05	372.00	341.95	3.11	45.59	81.11	93.60	110.03	2.574E-05
8	30.4	520.00	489.60	4.06	50.71	97.12	104.13	120.56	2.471E-05
9	30.95	573.00	542.05	4.43	53.08	103.67	106.03	122.46	2.573E-05
10	31.45	790.00	758.55	5.36	58.24	119.46	125.16	141.59	2.482E-05

Date	k C15715 @ 100 °C	Average $R_{thermal}$	1/h	Tabulated P_{Ni} @ 200°C
	(W/mK)	(m ² ·K/MW)	(m ² ·K/MW)	(Ωm)
15-Jan-97	350	102.44	5.00	1.58E-07

Notes / Misc. Features:

Plate bowed in the middle.

Plate inverted from Jan 14. Sanded too. Exactly the same thermocouple locations as Jan 15, no aluminum.

Different thermocouple locations since Jan 14. Ran with Aluminum foil at the electrodes.

Hard to tell whether T_2 (italicized) was touching the ceramic.

Heater failed after this run. Long, straight fracture just above bottom electrode.

At the end of the run, after observing the thermocouples, the kapton tape was burnt and it was obvious that none of the thermocouples were touching the Ni surface except for one, T_6 . Therefore, all other data was discarded and T_{avNi} is based only on T_6 .

Vendor 1.

Measured Quantities

	Thermocouple Measurements on Top of Heater (does not include T ₂)																
	T _{w,in} (°C)	T _{w,out} (°C)	T _{w,av} (°C)	T ₂ (°C)	T ₁ (°C)	T ₃ (°C)	T ₄ (°C)	T ₆ (°C)	T ₇ (°C)	T _{Ni,av} (°C)	V _{shunt} (mV)	I (A)	V _{film} (V)	R _{film} (Ω)	Power (W)	q" (MW/m ²)	
0	24.4	24.7	24.55	24.3	24	24.4	24.4	24.4	24.3	24.30							
1	24.6	25.1	24.85	24.9	26.6	29.6	27.5	28.7	27	27.88	1.08	64.98	0.597	0.00919	38.80	0.036	
2	24.9	25.3	25.1	25.7	39.3	47.6	38.6	42.7	36.1	40.86	2.24	134.78	1.360	0.01009	183.30	0.170	
3	25.5	25.9	25.7	26.4	51.8	66.4	51.7	55.7	45.2	54.16	2.87	172.69	1.870	0.01083	322.93	0.299	
4	26.2	26.6	26.4	27.4	75.1	106	76.8	72.4	60.4	78.14	3.66	220.22	2.730	0.01240	601.21	0.557	
5	26.5	26.9	26.7	28.6	115	161	119	113	87.2	119.04	4.38	263.54	3.780	0.01434	996.20	0.923	
6	27.2	27.6	27.4	30.8	150	222	182	181.9	132	173.58	5.25	315.89	5.290	0.01675	1671.07	1.548	
7	27.6	28.1	27.85	33.1		273.4	223.8	210	162.1	217.33	6.25	376.06	6.610	0.01758	2485.77	2.302	
8	28.1	28.6	28.35	36.3		391.2	282	306	215	298.55	7.75	466.32	8.230	0.01765	3837.79	3.555	

Date	Heater Generation	Heater Material	Heater Thickness (mils)	Heater Thickness (m)	Plate Material	Plate Thickness (m)	Ceramic Material	Ceramic Thickness (mils)	Ceramic Thickness (m)	Theoretical R _{th} @ 300°C (Ω)
5-Feb-97	Fifth	Ni	10	0.000254	C15715	0.003	Al ₂ O ₃	10	0.000254	0.000372

Heater Length (dir. of I) (m)	Heater Width (m)	Heater Area (m ²)	Flow Rate (GPM)	Number of nozzles	Nozzle I.D. (m)	Jet Velocity (m/s)	P _{in} (psi)	P _{out} (psi)	Estimated h (W/m ² K)
0.02129	0.05072	0.00108	62.5	14	0.002778	46.47	316	84	200000

Calculated Quantities

	$T_{w,av}$	$T_{Ni,av}$	ΔT_{av}	q''	$T_{Water-Cu}$	$T_{Cu-AlOxide}$	Effective $R_{thermal}$ (Ni/AlOxide)	$R_{thermal}$ (total)	ρ_{Ni} (calculated using $R_{Ni,m}$)
	(°C)	(°C)	(°C)	(MW/m ²)	(°C)	(°C)	(m ² -K/MW)	(m ² -K/MW)	(Ωm)
0	24.55	24.30	-0.25	0.00	24.55	24.55			
1	24.85	27.88	3.03	0.04	25.03	25.34	70.75	84.32	5.561E-06
2	25.1	40.86	15.76	0.17	25.95	27.40	79.26	92.83	6.108E-06
3	25.7	54.16	28.46	0.30	27.20	29.76	81.58	95.15	6.555E-06
4	26.4	78.14	51.74	0.56	29.18	33.96	79.34	92.92	7.504E-06
5	26.7	119.04	92.34	0.92	31.31	39.22	86.51	100.08	8.682E-06
6	27.4	173.58	146.18	1.55	35.14	48.41	80.87	94.45	1.014E-05
7	27.85	217.33	189.48	2.30	39.36	59.10	68.72	82.30	1.064E-05
8	28.35	298.55	270.20	3.55	46.12	76.59	62.44	76.01	1.068E-05

Date	k C15715 @ 100 °C	Average $R_{thermal}$	1/h	Tabulated ρ_{Ni} @ 300°C
	(W/mK)	(m ² -K/MW)	(m ² -K/MW)	(Ωm)
5-Feb-97	350	76.19	5.00	2.25E-07

Notes / Misc. Features:

Data set B, vendor 1.

Highest Current pumped through heater to date. This is believed to be due to the fact that we polished down the electrodes down to accuracy of 1 mil (they were off by 6-7 mils) and also sanded down the plate. The plate, however, was bowed in the middle and this resulted in a non-uniform thickness of Ni on the upper surface (more material on the sides than in the middle), but the surface was smooth.

The result was that the pressure tape imprints were excellent. See sets 2 and 3 of pressure tape.

The aluminum rod (which was also observed as bent) was replaced by a much stiffer steel rod.

Electrodes swapped for the first time. Electrode 1 is now on the bottom, electrode 2 on the top. This configuration maintained from now on.

Measured Quantities

	Thermocouple Measurements on Top of Heater (does not include T ₂)											I (A)	V _{film} (V)	R _{film} (Ω)	Power (W)	q" (MW/m ²)	
	T _{w,in} (°C)	T _{w,out} (°C)	T _{w,av} (°C)	T ₂ (°C)	T ₁ (°C)	T ₃ (°C)	T ₄ (°C)	T ₆ (°C)	T ₇ (°C)	T _{Ni,av} (°C)	V _{shunt} (mV)						
0	27.3	27.7	27.5	26.2	27	27.8	27.6	27.7	27.7	27.56							
1	28.1	28.5	28.3	27.9		42.2	37.5	41	38.9	39.90	2.06	123.95	1.16	0.00936	143.78	0.133	
2	28.5	28.8	28.65	28.7		62.7	51.3	57.7	54.9	56.65	3.05	183.52	1.88	0.01024	345.01	0.320	
3	28.7	29.1	28.9	29.6	92.3	93.4	74.6	82.6	79.1	84.40	4.06	244.29	2.87	0.01175	701.11	0.649	
4	29	29.4	29.2	31.2	153.2	158.8	109.4	136.1	127.1	136.92	5.05	303.86	4.45	0.01464	1352.17	1.252	
5	29.4	29.9	29.65	35.3	335.7	323	213.3	284.9	255	282.38	5.97	359.21	8.35	0.02325	2999.44	2.778	
6	29.8	30.4	30.1	40.5	578	579	447	449	458	502.20	6.30	379.07	11.64	0.03071	4412.39	4.087	

Date	Heater Generation	Heater Material	Heater Thickness (mils)	Heater Thickness (m)	Plate Material	Plate Thickness (m)	Ceramic Material	Ceramic Thickness (mils)	Ceramic Thickness (m)	Theoretical R _{Ni} @ 200°C (Ω)
6-Feb-97	Fifth	Ni	10	0.000254	C15715	0.003	Al ₂ O ₃	10	0.000254	0.000261

Heater Length (dir. of I) (m)	Heater Width (m)	Heater Area (m ²)	Flow Rate (GPM)	Number of nozzles	Nozzle I.D. (m)	Jet Velocity (m/s)	P _{in} (psi)	P _{out} (psi)	Estimated h (W/m ² K)
0.02129	0.05072	0.00108	62.5	14	0.002778	46.47	316.4	84	200000

Calculated Quantities

	$T_{w,av}$	$T_{Ni,av}$	ΔT_{av}	q''	$T_{Water-Cu}$	$T_{Cu-AlOxide}$	Effective $R_{thermal}$ (Ni/AlOxide)	$R_{thermal}$ (total)	P_{Ni} (calculated using R_{film})
	(°C)	(°C)	(°C)	(MW/m ²)	(°C)	(°C)	(m ² -K/MW)	(m ² -K/MW)	(Ωm)
0	27.5	27.56	0.06	0.00	27.50	27.50			
1	28.3	39.90	11.60	0.13	28.97	30.11	73.53	87.10	5.665E-06
2	28.65	56.65	28.00	0.32	30.25	32.99	74.05	87.62	6.201E-06
3	28.9	84.40	55.50	0.65	32.15	37.71	71.89	85.47	7.111E-06
4	29.2	136.92	107.72	1.25	35.46	46.20	72.44	86.01	8.865E-06
5	29.65	282.38	252.73	2.78	43.54	67.35	77.40	90.97	1.407E-05
6	30.1	502.20	472.10	4.09	50.53	85.56	101.95	115.52	1.859E-05

Date	k C15715 @ 100 °C	Average $R_{thermal}$	1/h	Tabulated P_{Ni} @ 200°C
	(W/mK)	(m ² -K/MW)	(m ² -K/MW)	(Ωm)
6-Feb-97	350	78.54	5.00	1.58E-07

Notes / Misc. Features:

Exactly the same setup as 5 Feb 97 run, but with cement. T_y may have moved a little since previous run. During the last measurement, the measured shunt voltage was unstable and the temperature was fluctuating too rapidly to get an accurate reading (measurement italicized). Couldn't get as much current through as 5 Feb run, suggests that these thin film heaters are not repeatable. Failed after this run. Arc was observed. Disgards theory that cemented areas prevent arcing as was thought previously. Vendor 1.

Measured Quantities

	Thermocouple Measurements on Top of Heater (does not include T ₂)											I (A)	V _{film} (V)	R _{film} (Ω)	Power (W)	q" (MW/m ²)	
	T _{w,in} (°C)	T _{w,out} (°C)	T _{w,av} (°C)	T ₂ (°C)	T ₁ (°C)	T ₃ (°C)	T ₄ (°C)	T ₅ (°C)	T ₇ (°C)	T _{Ni,av} (°C)	V _{shunt} (mV)						
0	24.6	24.9	24.75	24.3	24.4	24.3	24.5	24.2	24.2	24.32							
1	25.1	25.4	25.25	25	26.2	26.8	25.7	28.4	27.7	26.96	0.55	32.97	0.515	0.01562	16.98	0.016	
2	25.4	25.8	25.6	25.4	32.1	33.4	28	41	38.6	34.62	1.08	65.22	1.070	0.01640	69.79	0.066	
3	25.7	26	25.85	25.7	42.4	45.4	32	65.1	58.3	48.64	1.61	96.87	1.730	0.01786	167.59	0.158	
4	26	26.4	26.2	26.3	60.2	62.9	38.1	98	83.7	68.58	2.00	120.34	2.350	0.01953	282.80	0.266	
5	26.3	26.6	26.45	27.1	92.7	96.4	49.4	152.6	132.4	104.70	2.54	152.83	3.330	0.02179	508.93	0.479	
6	26.7	27	26.85	28.3	139.6	143	67	212.3	186.7	149.72	3.03	182.32	4.440	0.02435	809.48	0.761	

Date	Heater Generation	Heater Material	Heater Thickness (mils)	Heater Thickness (m)	Plate Material	Plate Thickness (m)	Ceramic Material	Ceramic Thickness (mils)	Ceramic Thickness (m)	Theoretical R _{Ni} @ 200°C (Ω)
11-Feb-97	Fifth	Ni	7	0.0001778	C15715	0.003	Al ₂ O ₃	10	0.000254	0.000358

Heater Length (dir. of I) (m)	Heater Width (m)	Heater Area (m ²)	Flow Rate (GPM)	Number of nozzles	Nozzle I.D. (m)	Jet Velocity (m/s)	P _{in} (psi)	P _{out} (psi)	Estimated h (W/m ² K)
0.02070	0.05136	0.001063	62.3	14	0.002778	46.32	316.2	83.9	200000

Calculated Quantities

	$T_{w,av}$	$T_{Ni,av}$	ΔT_{av}	q''	$T_{Water-Cu}$	$T_{Cu-AlOxide}$	Effective $R_{thermal}$ (Ni/AlOxide)	$R_{thermal}$ (total)	P_{Ni} (calculated using R_{film})
	(°C)	(°C)	(°C)	(MW/m ²)	(°C)	(°C)	(m ² ·K/MW)	(m ² ·K/MW)	(Ωm)
0	24.75	24.32	-0.43	0.00	24.75	24.75			
1	25.25	26.96	1.71	0.02	25.33	25.47	93.49	107.06	6.890E-06
2	25.6	34.62	9.02	0.07	25.93	26.49	123.84	137.41	7.237E-06
3	25.85	48.64	22.79	0.16	26.64	27.99	131.01	144.58	7.878E-06
4	26.2	68.58	42.38	0.27	27.53	29.81	145.76	159.33	8.614E-06
5	26.45	104.70	78.25	0.48	28.84	32.95	149.90	163.47	9.611E-06
6	26.85	149.72	122.87	0.76	30.66	37.18	147.81	161.38	1.074E-05

Date	k C15715 @ 100 °C	Average $R_{thermal}$	1/h	Tabulated P_{Ni} @ 200°C
	(W/mK)	(m ² ·K/MW)	(m ² ·K/MW)	(Ωm)
11-Feb-97	350	131.97	5.00	1.58E-07

Notes / Misc. Features:

Plate also bowed in the middle. Sanded down too much.

$R_{thermal}$ is higher here than Feb 5 and 6 data, since the Ni layer is thinner to the extent that Al Oxide shows in the middle which makes the heater area smaller than the nominal value. This implies that the heat flux is higher than that calculated and this increases the thermal resistance when taken into account.

Thus, heat flux data and any resulting calculations not accurate here.

When decreasing the heater area by 20%, this brings back the thermal resistance back into the expected range.

Stopped before failure so that another run is possible (see Feb 17 data).

Vendor 1.

Measured Quantities

	Thermocouple Measurements on Top of Heater (does not include T ₂)													
	T _{w,in} (°C)	T _{w,out} (°C)	T _{w,av} (°C)	T ₂ (°C)	T ₁ (°C)	T ₄ (°C)	T ₆ (°C)	T _{Ni,av} (°C)	V _{shunt} (mV)	I (A)	V _{film} (V)	R _{film} (Ω)	Power (W)	q" (MW/m ²)
0	24.2	24.5	24.35	23.9	24.2	24.5	24.1	24.27						
1	24.6	25	24.8	24.5	31.2	27.3	36.9	31.80	1.02	61.07	1.020	0.01670	62.29	0.059
2	24.9	25.2	25.05	25	44.7	32.6	60.5	45.93	1.60	96.27	1.770	0.01839	170.40	0.160
3	25.3	25.6	25.45	25.7	69.1	41.3	98.7	69.70	2.08	125.15	2.660	0.02125	332.91	0.313
4	25.6	26	25.8	26.5	109.4	56.2	158.3	107.97	2.54	152.83	3.760	0.02460	574.65	0.540
5	25.9	26.4	26.15	27.6	170.4	81.4	222	157.93	3.06	184.12	5.140	0.02792	946.38	0.890
6	26.2	26.6	26.4	28.5	200.5	97.7	249.2	182.47	3.53	212.40	5.910	0.02782	1255.28	1.181
7	26.6	27	26.8	29.9	249	129.7	357	245.23	4.14	249.10	7.550	0.03031	1880.73	1.769
8	27.1	27.6	27.35		277.5	149.2	520.6	315.77	4.87	293.03	8.560	0.02921	2508.32	2.359

Date	Heater Generation	Heater Material	Heater Thickness (mils)	Heater Thickness (m)	Plate Material	Plate Thickness (m)	Ceramic Material	Ceramic Thickness (mils)	Ceramic Thickness (m)	Theoretical R _{Ni} @ 200°C (Ω)
17-Feb-97	Fifth	Ni	7	0.0001778	C15715	0.003	Al ₂ O ₃	10	0.000254	0.000358

Heater Length (dir. of I) (m)	Heater Width (m)	Heater Area (m ²)	Flow Rate (GPM)	Number of nozzles	Nozzle I.D. (m)	Jet Velocity (m/s)	P _{in} (psi)	P _{out} (psi)	Estimated h (W/m ² K)
0.02070	0.05136	0.001063	80.6	38	0.002159	36.55	299.5	84	200000

Calculated Quantities

	$T_{w,av}$	$T_{Ni,av}$	ΔT_{av}	q''	$T_{Water-Cu}$	$T_{Cu-AlOxide}$	Effective $R_{thermal}$ (Ni/AlOxide) ($m^2 \cdot K/MW$)	$R_{thermal}$ (total) ($m^2 \cdot K/MW$)	P_{Ni} (calculated using R_{film}) (Ωm)
	(°C)	(°C)	(°C)	(MW/m^2)	(°C)	(°C)			
0	24.35	24.27	-0.08	0.00	24.35	24.35			
1	24.8	31.80	7.00	0.06	25.09	25.60	105.90	119.47	7.367E-06
2	25.05	45.93	20.88	0.16	25.85	27.23	116.73	130.30	8.110E-06
3	25.45	69.70	44.25	0.31	27.02	29.70	127.75	141.32	9.375E-06
4	25.8	107.97	82.17	0.54	28.50	33.14	138.45	152.02	1.085E-05
5	26.15	157.93	131.78	0.89	30.60	38.23	134.48	148.05	1.231E-05
6	26.4	182.47	156.07	1.18	32.30	42.42	118.61	132.18	1.227E-05
7	26.8	245.23	218.43	1.77	35.64	50.81	109.91	123.48	1.337E-05
8	27.35	315.77	288.42	2.36	39.15	59.37	108.68	122.25	1.289E-05

Date	k C15715 @ 100 °C (W/mK)	Average $R_{thermal}$ ($m^2 \cdot K/MW$)	1/h ($m^2 \cdot K/MW$)	Tabulated P_{Ni} @ 200°C (Ωm)
17-Feb-97	350	120.06	5.00	1.58E-07

Notes / Misc. Features:

Plate bowed in the middle. Exactly the same configuration as Feb 11, except with the 2.159 mm I.D. 38 nozzles. Exactly the same thermocouple locations. The plate failed after this run and, unfortunately, as a result of the kapton tape burning, thermocouples T_7 and T_3 came loose and their data was discarded.

$R_{thermal}$ is higher here than Feb 5 and 6 data, since the Ni layer is thinner to the extent that Al Oxide shows in the middle which makes the heater area smaller than the nominal value. This implies that the heat flux is higher than that calculated and this increases the thermal resistance when taken into account.

Thus, heat flux data and any resulting calculations not accurate here.

When decreasing the heater area by 20%, this brings back the thermal resistance back into the expected range.

Realised the seriousness of bowing problem. Extra care taken from here on to alert manufacturers. Goal is to keep any bowing limited to 2 mills or less on any one side.

Vendor 1.

Measured Quantities

	Thermocouple Measurements on Top of Heater (does not include T ₂)																
	T _{w,in} (°C)	T _{w,out} (°C)	T _{w,av} (°C)	T ₂ (°C)	T ₁ (°C)	T ₃ (°C)	T ₄ (°C)	T ₆ (°C)	T ₇ (°C)	T _{Mo,av} (°C)	V _{shunt} (mV)	I (A)	V _{film} (V)	R _{film} (Ω)	Power (W)	q" (MW/m ²)	
0	25.6	25.9	25.75	25.7	26	26.1	26.1	26.3	26.3	26.16							
1	27.5	27.9	27.7	27.1	28.2	28.3	28.3	28.4	28.2	28.28	1.7	102.29	0.09	0.000880	9.21	0.01	
2	28	28.3	28.15	27.5	30.5	30.3	30.3	30.9	30.3	30.46	3.4	204.58	0.181	0.000885	37.03	0.04	
3	28.6	29	28.8	28.2	34.5	33.8	34.4	35.5	34.3	34.5	5.1	306.87	0.278	0.000906	85.31	0.08	
4	29.1	29.5	29.3	28.9	40.4	38.6	39.8	41.6	39.5	39.98	7.4	445.26	0.411	0.000923	183.00	0.18	
5	29.6	29.9	29.75	29.3	45.8	42.8	44.4	46.6	43.6	44.64	8.45	508.44	0.472	0.000928	239.98	0.23	
6	30.7	31.1	30.9	31.5	138.4	111	129.3	140.8	124.1	128.72	19.3	1161.28	1.238	0.001066	1437.67	1.41	
7	31.1	31.6	31.35	32	147.8	126.7	140.3	153.4	137.4	141.12	20.1	1209.42	1.31	0.001083	1584.34	1.55	
8	31.4	31.9	31.65	32.6	161.5	140	152.5	165	149.4	153.68	20.85	1254.54	1.39	0.001108	1743.82	1.71	
9	31.6	32	31.8	33	169.7	147	159	170	153.5	159.84	21.2	1275.60	1.41	0.001105	1798.60	1.76	
10	32.3	32.8	32.55	34.2	193.6	172.9	182.7	196.2	177.7	184.62	22.55	1356.83	1.55	0.001142	2103.09	2.06	
11	32.9	33.3	33.1	35.1	214.9	194.9	206.3	221.1	201.1	207.66	23.58	1418.81	1.67	0.001177	2369.41	2.32	
12	33.2	33.7	33.45	35.9	234.7	212.8	224	242.6	223	227.42	24.62	1481.39	1.82	0.001229	2696.12	2.64	
13	33.6	34.2	33.9	36.8	277.5	264	275	296	271	276.7	26.65	1603.53	2.03	0.001266	3255.17	3.18	
14	34.1	34.7	34.4	38.2	322.3	320.6	327	345	320	326.98	28.75	1729.89	2.26	0.001306	3909.55	3.82	
15	34.6	35.2	34.9	39.4	361.7	366	373	394	367	372.34	30.75	1850.23	2.415	0.001305	4468.30	4.37	
16	34.9	35.6	35.25	41	425	447	437	461	430.6	440.12	34.3	2063.83	2.61	0.001265	5386.60	5.27	
17	35.4	36.1	35.75	43.6	486	529	508	526	504	510.6	37.2	2238.32	2.805	0.001253	6278.50	6.14	
18	35.9	36.6	36.25	44.5	477.6	529	508	505	479	499.72	37.1	2232.31	2.71	0.001214	6049.55	5.92	
19	36.4	37.2	36.8	46.4	535	605	599	597	571	581.4	39	2346.63	3.09	0.001317	7251.09	7.09	

Date	Heater Generation	Heater Material	Heater Thickness (mils)	Heater Thickness (m)	Plate Material	Plate Thickness (m)	Ceramic Material	Ceramic Thickness (mils)	Ceramic Thickness (m)	Theoretical R _{Mo} @ 300°C (Ω)
1-Mar-97	One TZM	Mo	10	0.000254	TZM	0.003175	Al ₂ O ₃	8	0.0002032	0.000191

Heater Length (dir. of I) (m)	Heater Width (m)	Heater Area (m ²)	Flow Rate (GPM)	Number of nozzles	Nozzle I.D. (m)	Jet Velocity (m/s)	P _{in} (psi)	P _{out} (psi)	Estimated h (W/m ² K)
0.01986	0.05149	0.001023	62.5	14	0.002778	46.47	313.8	83.6	200000

Calculated Quantities

	$T_{w,av}$	$T_{Mo,av}$	ΔT_{av}	q''	$T_{Water-TZM}$	$T_{TZM-AlOxide}$	Effective $R_{thermal}$ (Mo/AlOxide)	$R_{thermal}$ (Total)	P_{Mo} (calculated using R_{film})
	(°C)	(°C)	(°C)	(MW/m ²)	(°C)	(°C)	(m ² ·K/MW)	(m ² ·K/MW)	(Ωm)
0	25.75	26.16	0.41	0.00	25.75	25.75			
1	27.70	28.28	0.58	0.01	27.75	27.99	31.82	64.43	5.793E-07
2	28.15	30.46	2.31	0.04	28.33	29.33	31.19	63.80	5.825E-07
3	28.80	34.50	5.70	0.08	29.22	31.52	35.72	68.33	5.965E-07
4	29.30	39.98	10.68	0.18	30.19	35.14	27.07	59.68	6.077E-07
5	29.75	44.64	14.89	0.23	30.92	37.40	30.84	63.45	6.112E-07
6	30.90	128.72	97.82	1.41	37.93	76.74	36.97	69.58	7.019E-07
7	31.35	141.12	109.77	1.55	39.10	81.87	38.25	70.85	7.131E-07
8	31.65	153.68	122.03	1.71	40.18	87.25	38.96	71.56	7.295E-07
9	31.80	159.84	128.04	1.76	40.59	89.15	40.19	72.80	7.278E-07
10	32.55	184.62	152.07	2.06	42.83	99.61	41.34	73.95	7.521E-07
11	33.10	207.66	174.56	2.32	44.68	108.65	42.73	75.34	7.749E-07
12	33.45	227.42	193.97	2.64	46.63	119.42	40.97	73.57	8.089E-07
13	33.90	276.70	242.80	3.18	49.82	137.70	43.67	76.28	8.335E-07
14	34.40	326.98	292.58	3.82	53.51	159.06	43.92	76.53	8.601E-07
15	34.90	372.34	337.44	4.37	56.75	177.38	44.62	77.23	8.594E-07
16	35.25	440.12	404.87	5.27	61.59	207.01	44.26	76.87	8.326E-07
17	35.75	510.60	474.85	6.14	66.45	235.95	44.74	77.34	8.251E-07
18	36.25	499.72	463.47	5.92	65.83	229.15	45.74	78.35	7.993E-07
19	36.80	581.40	544.60	7.09	72.25	268.01	44.20	76.81	8.670E-07

Date	k TZM @ 300 °C	Average $R_{thermal}$	1/h	Tabulated ρ_{Mo} @ 300°C
	(W/mK)	(m ² ·K/MW)	(m ² ·K/MW)	(Ωm)
1-Mar-97	115	37.88	5.00	1.26E-07

Notes / Misc. Features:

Vendor 2, Data set D. Plates very very slightly bowed. TZM bends less than our Cu plates. Cemented thermocouples. Plate not sanded. Silver paint used for the first time. Temperatures impressively uniform all along the Mo heater (max. variation 70 degrees). Severe glow showed in all areas that were not covered by cement at high temperatures. Some crystals were forming in these areas and they were also glowing. Seems possible that if entire plate was covered with cement this would not happen. Plate failed at the end of the run and green powder was observed everywhere. The current was increasing independently without any user input; for this reason, data points between 0.23 and 1.93 MW/m² were missed. T_2 was touching the edge of the plate rather than on top of Aluminum Oxide. This run provides evidence that vendor quality control was the problem. Calculated R_{film} is much closer to measured now. Some error in data gathering, since the currents kept going up and could barely keep up with the temperature measurements, especially towards the end, but in any case max error was no more than 10-15 degrees (out of 500 degrees). Plate sprayed by Hayden (vendor 2). First plate run from this vendor.

Measured Quantities

Thermocouple Measurements on Top of Heater (does not include T₂ and T₈)

	T _{w,in} (°C)	T _{w,out} (°C)	T _{w,av} (°C)	T ₂ (°C)	T ₁ (°C)	T ₃ (°C)	T ₄ (°C)	T ₆ (°C)	T ₇ (°C)	T ₈ (°C)	T _{Mo,av} (°C)	V _{shunt} (mV)	I (A)	V _{film} (V)	R _{film} (Ω)	Power (W)	q" (MW/m ²)
0	27.8	28.1	27.95	25.1	27.9	28.3	27.9	28.1	28.4	18.5	28.12						
1	28.5	28.8	28.65	27	37.4	36.9	41.3	38.4	36.6	20.1	38.12	1.6	96.27	2.3	0.023891	221.43	0.21
2	28.9	29.3	29.1	27.7	54.8	50.1	60.6	54.6	50.5	22.8	54.12	2.7	162.46	3.95	0.024314	641.71	0.62
3	29.3	29.7	29.5	28.6	73	64.7	81.6	72.2	65	25.9	71.3	3.6	216.61	5.45	0.025160	1180.54	1.14
4	29.7	30.1	29.9	29.5	100.7	90	122.2	101.2	88.9	31.1	100.6	4.5	270.77	7.38	0.027256	1998.25	1.92
5	30.1	30.6	30.35	30.6	139.2	130.5	235.8	167.6	121.6	41.6	158.94	5.5	330.94	9.7	0.029311	3210.07	3.09
6	30.6	31.3	30.95	32.7	274	312.7	473	364	263	59	337.34	6.6	397.12	13.6	0.034246	5400.86	5.20
7	30.8	31.6	31.2	34.3	477	392	591	451.5	390	67	460.3	7.375	443.75	15.6	0.035155	6922.56	6.67
8	31.8	32.6	32.2	34.6	540	401.6	598	453	441	71.9	486.72	7.65	460.30	15.7	0.034108	7226.72	6.96

Date	Heater Generation	Heater Material	Heater Thickness (mils)	Heater Thickness (m)	Plate Material	Plate Thickness (m)	Ceramic Material	Ceramic Thickness (mils)	Ceramic Thickness (m)	Theoretical R _{Mc} @ 300°C (Ω)
4-Mar-97	Six	Mo	10	0.000254	C15715	0.003	Al ₂ O ₃	8	0.0002032	0.000201

Heater Length (dir. of I) (m)	Heater Width (m)	Heater Area (m ²)	Flow Rate (GPM)	Number of nozzles	Nozzle I.D. (m)	Jet Velocity (m/s)	P _{in} (psi)	P _{out} (psi)	Estimated h (W/m ² K)
0.02051	0.05062	0.001038	62.5	14	0.002778	46.47	315.4	84	200000

Calculated Quantities

	$T_{w,av}$	$T_{Mo,av}$	ΔT_{av}	q''	$T_{Water-Cu}$	$T_{Cu-AlOxide}$	Effective $R_{thermal}$ (Mo/AlOxide)	$R_{thermal}$ (total)	P_{Mo} (calculated using R_{film})
	(°C)	(°C)	(°C)	(MW/m ²)	(°C)	(°C)	(m ² ·K/MW)	(m ² ·K/MW)	(Ωm)
0	27.95	28.12	0.17	0.00	27.95	27.95			
1	28.65	38.12	9.47	0.21	29.72	31.54	30.83	44.41	1.498E-05
2	29.10	54.12	25.02	0.62	32.19	37.49	26.91	40.48	1.524E-05
3	29.50	71.30	41.80	1.14	35.19	44.93	23.19	36.76	1.577E-05
4	29.90	100.60	70.70	1.92	39.52	56.02	23.16	36.74	1.709E-05
5	30.35	158.94	128.59	3.09	45.81	72.31	28.02	41.59	1.838E-05
6	30.95	337.34	306.39	5.20	56.96	101.54	45.33	58.90	2.147E-05
7	31.20	460.30	429.10	6.67	64.54	121.68	50.79	64.36	2.204E-05
8	32.20	486.72	454.52	6.96	67.00	126.66	51.73	65.30	2.138E-05

Date	k C15715 @ 100 °C	Average $R_{thermal}$	1/h	Tabulated P_{Mo} @ 300°C
	(W/mK)	(m ² ·K/MW)	(m ² ·K/MW)	(Ωm)
4-Mar-97	350	35.00	5.00	1.26E-07

Notes / Misc. Features:

Data set C, vendor 1.
 Plate bowed 5 mils only. Silver paint used. Cement applied everywhere even around electrodes to cover nearly entire plate.
 T_8 on electrode at the point were protruded part joins to rest of electrode.
 Seems like plate failed at the bottom electrode in the middle. Black spot there.
 Electrodes were sanded manually since previous run.

Measured Quantities

Thermocouple Measurements on Top of Heater (does not include T₂ and T₈)

	T _{w,in} (°C)	T _{w,out} (°C)	T _{w,av} (°C)	T ₂ (°C)	T ₁ (°C)	T ₃ (°C)	T ₆ (°C)	T ₇ (°C)	T ₈ (°C)	T _{Cu,av} (°C)	V _{shunt} (mV)	I (A)	V _{film} (V)	R _{film} (Ω)	Power (W)	q" (MW/m ²)
0	31.6	32	31.8	29.2	32	32.4	32.3	32.2	19.9	29.76						
1	32.6	32.9	32.75	30.9	32.9	33.6	33.3	33.3	19.4	30.5	3	180.51	0.0703	0.000389	12.69	0.01
2	32.9	33.2	33.05	31.4	33.9	34.8	34.4	34.4	19.7	31.44	5	300.85	0.115	0.000382	34.60	0.03
3	33.1	33.3	33.2	32	37.1	40.5	42	42.2	25	37.36	12	722.04	0.2825	0.000391	203.98	0.18
4	33.3	33.9	33.6	34	108	143	131	133	58	114.6	41.5	2497.06	1.125	0.000451	2809.19	2.51
5	33.5	34.1	33.8	35	190	265	244	175		218.5	50	3008.50	1.45	0.000482	4362.33	3.89
6	33.7	34.4	34.05	36	240	325	298	207		267.5	52.25	3143.88	1.55	0.000493	4873.02	4.35
7	33.9	34.6	34.25	38	280	380	350	245	129.6	276.92	53.7	3231.13	1.66	0.000514	5363.67	4.79
8	34	34.7	34.35	39.5	322	430	396	278	150	315.2	54.9	3303.33	1.7	0.000515	5615.67	5.01
9	34.4	35.1	34.75	41.5	347	420	388	283.4	162	320.08	54.2	3261.21	1.67	0.000512	5446.23	4.86
10	35.4	36.1	35.75	44.7	388	470	432	333	173.4	359.28	55.5	3339.44	1.8	0.000539	6010.98	5.37
11	35.9	36.6	36.25	46.4	413	501.5	456	360	188.2	383.74	56.45	3396.60	1.83	0.000539	6215.77	5.55
12	36.2	36.9	36.55	47.4	428	509	464	372	195.2	393.64	57.1	3435.71	1.86	0.000541	6390.42	5.70
13	36.6	37.3	36.95	48.5	449	532	485	394.4	203	412.68	58.25	3504.90	1.9	0.000542	6659.31	5.94
14	36.9	37.7	37.3	49.7	468.6	557.2	514	418	215.5	434.66	59.5	3580.12	1.96	0.000547	7017.03	6.26
15	37.5	38.2	37.85	50.4	485	586	531	432	219.9	450.78	60.5	3640.29	1.975	0.000543	7189.56	6.42

Date	Heater Generation	Heater Material	Heater Thickness (mils)	Heater Thickness (m)	Plate Material	Plate Thickness (m)	Ceramic Material	Ceramic Thickness (mils)	Ceramic Thickness (m)	Theoretical R _{Cu} @ 400°C (Ω)
5-Mar-97	Six	Cu	10	0.000254	C15715	0.004	Al ₂ O ₃	8	0.0002032	0.000069

Heater Length (dir. of I) (m)	Heater Width (m)	Heater Area (m ²)	Flow Rate (GPM)	Number of nozzles	Nozzle I.D. (m)	Jet Velocity (m/s)	P _{in} (psi)	P _{out} (psi)	Estimated h (W/m ² K)
0.02202	0.05088	0.00112	62.5	14	0.002778	46.47	315	83.9	200000

Calculated Quantities

	$T_{w,av}$	$T_{Cu,av}$	ΔT_{av}	q''	$T_{Water-C15715}$	$T_{C15715-AlOxide}$	Effective $R_{thermal}$ (Cu/AlOxide)	$R_{thermal}$ (total)	P_{Cu} (calculated using R_{lim})
	(°C)	(°C)	(°C)	(MW/m ²)	(°C)	(°C)	(m ² ·K/MW)	(m ² ·K/MW)	(Ωm)
0	31.80	29.76	-2.04	0.00	31.80	31.80			
1	32.75	30.50	-2.25	0.01	32.81	32.94			2.285E-07
2	33.05	31.44	-1.61	0.03	33.20	33.56			2.243E-07
3	33.20	37.36	4.16	0.18	34.11	36.19			2.296E-07
4	33.60	114.60	81.00	2.51	46.14	74.79	15.88	32.31	2.644E-07
5	33.80	218.50	184.70	3.89	53.27	97.77	31.01	47.44	2.828E-07
6	34.05	267.50	233.45	4.35	55.80	105.50	37.25	53.67	2.893E-07
7	34.25	276.92	242.67	4.79	58.19	112.90	34.26	50.69	3.015E-07
8	34.35	315.20	280.85	5.01	59.41	116.69	39.60	56.03	3.020E-07
9	34.75	320.08	285.33	4.86	59.06	114.61	42.27	58.70	3.005E-07
10	35.75	359.28	323.53	5.37	62.58	123.89	43.87	60.30	3.163E-07
11	36.25	383.74	347.49	5.55	63.99	127.39	46.21	62.63	3.162E-07
12	36.55	393.64	357.09	5.70	65.07	130.25	46.18	62.61	3.177E-07
13	36.95	412.68	375.73	5.94	66.67	134.60	46.79	63.21	3.181E-07
14	37.30	434.66	397.36	6.26	68.62	140.19	47.02	63.45	3.213E-07
15	37.85	450.78	412.93	6.42	69.94	143.27	47.92	64.35	3.184E-07

Date	k C15715 @ 100 °C	Average $R_{thermal}$	1/h	Tabulated P_{Cu} @ 400 °C
	(W/mK)	(m ² ·K/MW)	(m ² ·K/MW)	(Ωm)
5-Mar-97	350	39.85	5.00	4.0433E-08

Notes / Misc. Features:

Copper heater used in an attempt to reduce electrical resistance.
 T_g on electrode. Cement on most of the plate. Silver paint used. Least bowed plate ever supplied from vendor 1: claimed 2 mils bowing maximum.
 Hot spot on bottom right electrode. Fractured along lower electrode; seems like copper heater melted. Different process used for spraying this time; electric arc spraying. Temperatures highly non-uniform.
 This heater ran 210.6 A through it at 0.101 V (i.e. $R=0.00048$ Ohms) across the heater without silver paint. After using silver paint, it ran 183 A at 0.070 V ($R=0.00038$ Ohms); a slight improvement was observed using the silver paint.
 Comparing this to one of vendor 2's plates (Mo heater) of same heater thickness, Vendor 2's plate ran 210.6 A at 0.059 V ($R=0.00028$ Ohms) without even using silver paint. This is stronger evidence that vendor quality control has a significant effect on R.
 It is worth pointing out that vendor 1 produced a much rougher ceramic surface.
 Vendor 1.

Measured Quantities

Thermocouple Measurements on Top of Heater (does not include T₁)

	T _{w,in} (°C)	T _{w,out} (°C)	T _{w,av} (°C)	T ₁ (°C)	T ₂ (°C)	T ₃ (°C)	T ₄ (°C)	T ₅ (°C)	T ₆ (°C)	T _{M₀,av} (°C)	I (A)	V _f (V)	R _f (Ω)	Power (W)	q" (MW/m ²)
1	28.4	28.7	28.55	28.79	45.01	43.86	45.00	56.39	53.15	48.81	351.99	1.2	0.003409	422.39	0.39
2	29.4	29.8	29.6	30.32	53.81	51.29	52.40	69.75	66.37	58.76	418.18	1.465	0.003503	612.64	0.57
3	30.1	30.5	30.3	30.85	68.27	65.87	64.17	96.38	88.83	76.78	511.45	1.88	0.003676	961.52	0.89
4	30.9	31.3	31.1	31.80	86.74	82.50	83.31	129.50	119.34	100.34	601.10	2.32	0.003860	1394.55	1.30
5	31.3	31.8	31.55	33.01	112.49	110.11	109.84	176.50	162.70	134.33	700.98	2.925	0.004173	2050.37	1.91
6	31.4	31.9	31.65	33.61	137.48	134.58	136.81	221.44	226.06	171.27	770.18	3.43	0.004454	2641.70	2.46
7	31.6	32.2	31.9	34.45	160.99	182.51	188.15	282.62	298.76	222.38	808.68	3.82	0.004724	3089.18	2.87
8	32.3	32.8	32.55	36.21	210.43	261.88	312.98	388.21	423.29	319.20	867.65	4.58	0.005279	3973.84	3.70
9	32.7	33.5	33.1	38.11	281.40	368.24	447.77	546.04	564.61	440.62	962.12	5.625	0.005846	5411.92	5.03
10	32.9	33.7	33.3								1083.06	6.69	0.006177	7245.67	6.74

Date	Heater Generation	Heater Material	Heater Thickness (mils)	Heater Thickness (m)	Plate Material	Plate Thickness (m)	Ceramic Material	Ceramic Thickness (mils)	Ceramic Thickness (m)	Theoretical R _{M₀} @ 300°C (Ω)
19-Mar-97	Two TZM	Mo	3	0.0000762	TZM	0.0023	Al ₂ O ₃	8	0.0002032	0.000681

Heater Length (dir. of I) (m)	Heater Width (m)	Heater Area (m ²)	Flow Rate (GPM)	Number of nozzles	Nozzle I.D. (m)	Jet Velocity (m/s)	P _{in} (psi)	P _{out} (psi)	Estimated h (W/m ² K)
0.02104	0.05108	0.001075	62.3	14	0.002778	46.32	314.2	84	200000

Calculated Quantities

	$T_{w,av}$	$T_{Mo,av}$	ΔT_{av}	q''	$T_{Water-TZM}$	$T_{TZM-AlOxide}$	Effective $R_{thermal}$ (Mo/AlOxide)	$R_{thermal}$ (total)	ρ_{Mo} (calculated using R_{film})
	(°C)	(°C)	(°C)	(MW/m ²)	(°C)	(°C)	(m ² ·K/MW)	(m ² ·K/MW)	(Ωm)
1	28.55	48.81	20.26	0.39	30.51	38.37	26.56	51.56	6.306E-07
2	29.60	58.76	29.16	0.57	32.45	43.85	26.17	51.17	6.480E-07
3	30.30	76.78	46.48	0.89	34.77	52.66	26.96	51.96	6.799E-07
4	31.10	100.34	69.24	1.30	37.59	63.53	28.37	53.37	7.139E-07
5	31.55	134.33	102.78	1.91	41.09	79.24	28.88	53.88	7.718E-07
6	31.65	171.27	139.62	2.46	43.94	93.09	31.81	56.81	8.237E-07
7	31.90	222.38	190.48	2.87	46.27	103.75	41.28	66.28	8.737E-07
8	32.55	319.20	286.65	3.70	51.03	124.97	52.54	77.54	9.763E-07
9	33.10	440.62	407.52	5.03	58.27	158.97	55.94	80.94	1.081E-06
10	33.30			6.74					1.142E-06

Date	k TZM @ 300 °C (W/mK)	Average $R_{thermal}$ (m ² ·K/MW)	1/h (m ² ·K/MW)	Tabulated ρ_{Mo} @ 300°C (Ωm)
19-Mar-97	115	35.39	5.00	1.26E-07

Notes / Misc. Features:

Data Set E, vendor 2.

First time computer was used to gather data.

Sampling rate = 200 ms; cold junction temperature = 27.3 °C. Silver paint used (used previously and from now on).

T_7 and T_8 on electrode to measure loss by conduction. T_1 on ceramic layer. Computer used for the first time for data acquisition, didn't resolve T_7 and T_8 accurately to get heat loss by conduction estimate.

Temperatures non-uniform again. Left side hotter than right.

Measured Quantities

Thermocouple Measurements on Top of Heater

	$T_{w,in}$ (°C)	$T_{w,out}$ (°C)	$T_{w,av}$ (°C)	T_2 (°C)	T_4 (°C)	T_5 (°C)	T_6 (°C)	$T_{Mo,av}$ (°C)	I (A)	V_f (V)	R_f (Ω)	P_{net} (W)	q''_{net} (MW/m ²)
1	30.3	30.7	30.5	123.24	120.49	98.09	94.60	109.11	722.04	1.67	0.002313	1185.49	1.09
2	30.7	31.1	30.9	158.16	157.34	124.73	121.40	140.53	825.23	1.999	0.002422	1619.16	1.49
3	30.9	31.3	31.1	212.69	214.05	165.91	162.99	188.58	942.86	2.455	0.002604	2270.70	2.08
4	31.1	31.7	31.4	310.20	315.51	241.97	239.10	276.39	1082.46	3.18	0.002938	3381.26	3.10
5	31.5	32.1	31.8	468.07	478.17	385.82	370.69	425.76	1265.98	4.26	0.003365	5335.49	4.89
6	31.9	32.6	32.25	567.05	564.82	508.03	489.26	532.94	1436.86	4.99	0.003473	7115.74	6.53
7	31.8	32.6	32.2	640.00		563.28	557.64	587.43	1523.50	5.22	0.003426	7857.87	7.21

Date	Heater Generation	Heater Material	Heater Thickness (mils)	Heater Thickness (m)	Plate Material	Plate Thickness (m)	Ceramic Material	Ceramic Thickness (mils)	Ceramic Thickness (m)	Theoretical R_{Mo} @ 300°C (Ω)
24-Mar-97	Two TZM	Mo	5	0.000127	TZM	0.0023	Al ₂ O ₃	8	0.0002032	0.000413

Heater Length (dir. of I) (m)	Heater Width (m)	Heater Area (m ²)	Flow Rate (GPM)	Number of nozzles	Nozzle I.D. (m)	Jet Velocity (m/s)	P_{in} (psi)	P_{out} (psi)	Estimated h (W/m ² K)
0.02130	0.05118	0.00109	62.4	14	0.002778	46.40	315.6	84	200000

Calculated Quantities

	$T_{w,av}$	$T_{Mo,av}$	ΔT_{av}	q''_{net}	$T_{Water-TZM}$	$T_{TZM-AlOxide}$	Effective $R_{thermal}$ (Mo/AlOxide) ($m^2 \cdot K/MW$)	$R_{thermal}$ (total) ($m^2 \cdot K/MW$)	ρ_{Mo} (calculated using R_{film}) (Ωm)
	(°C)	(°C)	(°C)	(MW/m^2)	(°C)	(°C)			
1	30.50	109.11	78.61	1.09	35.94	57.69	47.28	72.28	7.059E-07
2	30.90	140.53	109.63	1.49	38.33	68.04	48.81	73.81	7.393E-07
3	31.10	188.58	157.48	2.08	41.52	83.18	50.60	75.60	7.947E-07
4	31.40	276.39	244.99	3.10	46.91	108.95	53.98	78.98	8.966E-07
5	31.80	425.76	393.96	4.89	56.27	154.17	55.49	80.49	1.027E-06
6	32.25	532.94	500.69	6.53	64.89	195.45	51.70	76.70	1.060E-06
7	32.20	587.43	555.23	7.21	68.24	212.42	52.02	77.02	1.046E-06

Date	k TZM @ 300 °C (W/mK)	Average $R_{thermal}$ ($m^2 \cdot K/MW$)	1/h ($m^2 \cdot K/MW$)	Tabulated ρ_{Mo} @ 300°C (Ωm)
24-Mar-97	115	51.41	5.00	1.26E-07

Notes / Misc. Features:

Data set F, vendor 2.

First calculation that takes into account heat loss due to conduction. Q_{loss} was only 95 W at the highest flux.

Sampling rate = 200 ms; cold junction temperature = 29 °C. T_3 came off at the beginning of the run and data was eliminated.

T_1 not used on side of plate. T_7 and T_8 taken manually. Generally, left side cooler than right side.

Measured Quantities

	Thermocouple Measurements on Top of Heater										I (A)	V _f (V)	R _f (Ω)	Power (W)	q" (MW/m ²)
	T _{w,in} (°C)	T _{w,out} (°C)	T _{w,av} (°C)	T ₂ (°C)	T ₃ (°C)	T ₄ (°C)	T ₅ (°C)	T ₆ (°C)	T _{Mo,av} (°C)						
1	27	27.4	27.2	57.87	57.57	49.90	61.45	60.13	57.43	634.79	0.87	0.001371	552.27	0.49	
2	27.6	28	27.8	79.63	78.67	66.71	85.04	82.18	78.64	806.28	1.16	0.001439	935.28	0.83	
3	27.9	28.4	28.15	109.85	108.32	89.02	118.26	112.80	107.44	980.77	1.52	0.001550	1490.77	1.32	
4	28.2	28.7	28.45	140.23	142.79	115.82	157.18	152.12	141.83	1101.11	1.81	0.001644	1993.01	1.76	
5	28.5	29	28.75	169.12	175.04	142.50	191.95	187.07	173.13	1173.32	2.01	0.001713	2358.36	2.08	
6	28.8	29.3	29.05	221.44	228.16	186.16	251.39	246.59	227.13	1290.65	2.38	0.001844	3071.74	2.71	
7	29.4	29.9	29.65	269.86	270.55	219.84	299.28	293.88	270.48	1362.85	2.65	0.001944	3611.55	3.19	
8	30.2	30.8	30.5	325.62	330.60	268.26	395.45	364.89	336.20	1483.19	2.995	0.002019	4442.16	3.92	
9	30.6	31.2	30.9	353.78	369.47	287.84	455.56	408.03	374.01	1558.40	3.18	0.002041	4955.72	4.37	
10	30.9	31.6	31.25	395.30	427.67	327.37	542.30	472.39	433.50	1672.73	3.435	0.002054	5745.81	5.07	
11	31.7	32.4	32.05	441.39	495.31	371.10		537.65	461.84	1775.02	3.68	0.002073	6532.06	5.76	
12	32.1	32.8	32.45	478.87	546.36	407.44		567.38	498.48	1862.26	3.86	0.002073	7188.33	6.34	
13	32.3	33	32.65	510.19	557.94	426.46		559.92	515.12	1883.32	3.98	0.002113	7495.62	6.61	

Date	Heater Generation	Heater Material	Heater Thickness (mils)	Heater Thickness (m)	Plate Material	Plate Thickness (m)	Ceramic Material	Ceramic Thickness (mils)	Ceramic Thickness (m)	Theoretical R _{Mo} @ 300°C (Ω)
2-Apr-97	Two TZM	Mo	7	0.0001778	TZM	0.0023	Al ₂ O ₃	8	0.0002032	0.000290

Heater Length (dir. of I) (m)	Heater Width (m)	Heater Area (m ²)	Flow Rate (GPM)	Number of nozzles	Nozzle I.D. (m)	Jet Velocity (m/s)	P _{in} (psi)	P _{out} (psi)	Estimated h (W/m ² K)
0.02153	0.05265	0.001133	62.5	14	0.002778	46.47	315.3	84	200000

Calculated Quantities

	$T_{w,av}$	$T_{Mo,av}$	ΔT_{av}	q''	$T_{Water-TZM}$	$T_{TZM-AlOxide}$	Effective $R_{thermal}$ (Mo/AlOxide)	$R_{thermal}$ (total)	ρ_{Mo} (calculated using R_{film})
	(°C)	(°C)	(°C)	(MW/m ²)	(°C)	(°C)	(m ² ·K/MW)	(m ² ·K/MW)	(Ωm)
1	27.20	57.43	30.23	0.49	29.64	39.38	37.04	62.04	5.960E-07
2	27.80	78.64	50.84	0.83	31.93	48.43	36.61	61.61	6.257E-07
3	28.15	107.44	79.29	1.32	34.73	61.03	35.29	60.29	6.740E-07
4	28.45	141.83	113.38	1.76	37.24	72.41	39.48	64.48	7.149E-07
5	28.75	173.13	144.38	2.08	39.15	80.77	44.39	69.39	7.450E-07
6	29.05	227.13	198.08	2.71	42.60	96.80	48.09	73.09	8.020E-07
7	29.65	270.48	240.83	3.19	45.58	109.31	50.58	75.58	8.456E-07
8	30.50	336.20	305.70	3.92	50.10	128.48	53.00	78.00	8.782E-07
9	30.90	374.01	343.11	4.37	52.76	140.21	53.47	78.47	8.874E-07
10	31.25	433.50	402.25	5.07	56.60	157.98	54.35	79.35	8.931E-07
11	32.05	461.84	429.79	5.76	60.86	176.12	49.58	74.58	9.016E-07
12	32.45	498.48	466.03	6.34	64.16	191.00	48.48	73.48	9.014E-07
13	32.65	515.12	482.47	6.61	65.72	197.98	47.96	72.96	9.191E-07

Date	k TZM @ 300 °C (W/mK)	Average $R_{thermal}$ (m ² ·K/MW)	1/h (m ² ·K/MW)	Tabulated ρ_{Mo} @ 300°C (Ωm)
2-Apr-97	115	46.03	5.00	1.26E-07

Notes / Misc. Features:

Data set G, vendor 2.

Heat loss due to conduction calculated for a few points, but removed due to inconsistencies in T_7 and T_8 readings. In any case, Q_{loss} by conduction did not exceed 170 W. After data point 10, T_5 gave negative readings and was discarded. T_1 was not used.

Let side was hotter than right side of the plate. Sampling rate = 200 ms.

This is the only time where temperature readings at failure were captured. Unfortunately the hottest temperature which should have been recorded by T_5 was lost. It should, however, be approximately 630 °C.